Galaxy Overdensities and Emission Line Galaxies in the Faint Infrared Grism Survey

by

John Pharo

A Dissertation Presented in Partial Fulfillment
of the Requirements for the Degree
Doctor of Philosophy

Approved July 2019 by the
Graduate Supervisory Committee:

Sangeeta Malhotra, Co-Chair
Patrick Young, Co-Chair
James Rhoads
Evan Scannapieco
Sanchayeeta Borthakur

ARIZONA STATE UNIVERSITY

August 2019

ABSTRACT

Learning how properties of galaxies such as star formation, galaxy interactions, chemical composition, and others evolve to produce the modern universe has long been a goal of extragalactic astronomy. In recent years, grism spectroscopy from the Hubble Space Telescope (HST) has provided a means to study these properties with spectroscopy while avoiding the limitations of ground-based observation. In this dissertation, I present several studies wherein I used HST G102 grism spectroscopy from the Faint Infrared Grism Survey (FIGS) to investigate these fundamental properties of galaxies and how they interact and evolve. In the first study, I combined the grism spectra with broadband photometry to produce a catalog of redshifts with improved accuracy, reducing the median redshift error from 3% to 2%. With this redshift catalog, I conducted a systematic search for galaxy overdensities in the FIGS fields, producing a list of 24 significant candidates. In the second study, I developed a method for identifying emission line galaxy (ELG) candidates from continuum-subtracted 1D spectra, and identified 71 ELGs in one FIGS field. In matching MUSE/VLT spectra, I measured the [OIII]λ4363 emission line for 14 FIGS ELGs, and used this to measure their T_e-based gas-phase metallicities. These ELGs show a low-metallicity offset on the Mass-Metallicity Relation, and I demonstrated that this offset can be explained by recent star formation. In the third study, I expanded the ELG search to all four FIGS fields, identifying 208 Hα, [OIII]$\lambda\lambda$4959,5007, and [OII]$\lambda\lambda$3727,3729 line emitters. I compiled a catalog of line fluxes, redshifts, and equivalent widths. I combined this catalog with the overdensity study to investigate a possible relationship between line luminosity, star formation, and an ELG's environment. In the fourth study, I usde 15 FIGS Hα emitters and 49 "green pea" line emitters to compare Hα and the far-UV continuum as tracers of star formation. I explored a correlation between the Hα-FUV ratio and the ratio of [OIII]$\lambda\lambda$4959,5007 to [OII]$\lambda\lambda$3727,3729 and its implications for star formation history.

DEDICATION

To my parents Mollie and Nancy and to my sister Jean, without whose many sacrifices and constant support I could not have done this.

ACKNOWLEDGMENTS

First, I would like to thank my advisers, Sangeeta Malhotra and James Rhoads, for their guidance and support during my PhD. I would also like to thank Evan Scannapieco, Patrick Young, and Sanchayeeta Borthakur for taking the time to be on my committee and offering me their advice and insights.

I want to thank the other members of the Malhotra-Rhoads research group, including Alicia Coughlin, Tianxing Jiang, Huan Yang, Vithal Tilvi, Bhavin Joshi, Mark Smith, Karen Olsen, Santosh Harish, Keunho Kim, Lucia Perez, Ali Ahmad Khostovan, and Isak Wold.

This work would not have been possible without the many efforts of the FIGS team, who proposed for and reduced the data that is the basis of all my work, and who offered me advice and suggestions that greatly improved that work.

I would like to thank NASA and the Goddard Space Flight Center for hosting me for the last few years of my PhD, and in particular Jane Rigby, Michael Florian, Amber Straughn, Travis Fischer, and H. D. Thorpe for helping to make Goddard an interesting place to work.

Thanks to Rebecca Dial, Rebecca Polley, Amanda Ramos, Juana Garcia, and all of the others who keep SESE running. Without their helpfulness, patience, and tolerance for a certain amount of bureaucratic ineptitude on my part, I'm not sure I'd ever have gotten anything done.

TABLE OF CONTENTS

CHAPTER Page

APPENDIX

LIST OF TABLES

LIST OF FIGURES

Figure Page

Chapter 1

INTRODUCTION

1.1 Galaxy Evolution in the $z < 2$ Universe

A major goal of extragalactic surveys has long been to probe the evolution of galaxies from deep in the epoch of reionization at $6 < z < 11$ to the local universe at $z = 0$. Galaxy evolution can be studied by learning how properties of galaxies such as star formation, galaxy interactions and environments, chemical composition, and others evolve over this history. Star formation activity in galaxies and merger interactions between galaxies are thought to have peaked at redshift $z \sim 2$ (e.g., Madau & Dickinson, 2014, and references therein), before declining towards $z = 0$. The nature of this decline and its relation to other galaxy characteristics is key to understanding the development of the modern universe.

Nebular emission lines are commonly used as measures of star formation (Kennicutt, 1998, and references therein) and as proxies for the heavy element composition of nebular gas, or gas-phase metallicity (Kobulnicky & Kewley, 2004; Izotov et al., 2006). Consequently, surveys targeting emission lines are frequently used to probe the evolution of these properties by measuring them at different redshifts and for galaxies with a range of stellar masses. At a given stellar mass, galaxies are usually found to have lower metallicity at $2 < z < 3$ than at $z = 0$ (Tremonti et al., 2004; Erb et al., 2006; Mannucci et al., 2010), and other studies have found little evolution from $z = 0.8$ to $z = 0$ (Zahid et al., 2011). Attempts have been made to develop an empirical Fundamental Metallicity Relation to relate metallicity, stellar mass, and star formation rate (SFR) in this period (Mannucci et al., 2009).

Attempts have also been made to search for a link between galaxy interactions and star

formation, with some studies suggesting that nebular emission and related star formation are triggered by interactions with companion galaxies (Kennicutt et al., 1987; Alonso et al., 2004). Alternatively, Scoville et al. (2013) studied ultraviolet-continuum-derived SFRs as a function of the density of galaxies (Σ) in redshift slices up to $z < 3$ in the COSMOS field, finding a flat SFR-Σ relationship for $0.8 < z < 2$. At lower redshift, they measure a flat relationship up to Σ of a few, after which the SFR declines with increasing density, with a stronger decline in lower redshift bins. It is possible that after the merger peak, higher-density environments may have already quenched star formation in local galaxies through strangulation or ram-pressure stripping (Muzzin et al., 2012, 2014), depleting their reserves of star-forming material and increasingly relegating star formation to intermediate and field densities.

In this redshift regime, the rest-frame optical emission lines commonly used are redshifted into the near-infrared (NIR). To study this critical transition period, surveys are needed that can measure emission lines and other galaxy properties in this redshift range.

1.2 Slitless Spectroscopy

In order to place galaxies in the proper context of galaxy evolution history, their redshifts must first be measured accurately. Galaxy characteristics like redshifts are most accurately measured through the identification of fixed spectroscopic features, such as nebular emission or absorption lines or broad features such at the 4000 Å and Lyman breaks. Obtaining spectroscopic measurements with sufficient signal-to-noise (S/N) to discern these features is not always practical, however. The S/N required to measure continuum emission or resolve nearby emission lines requires increased integration time for observations, particularly for faint sources. At UV and infrared wavelengths, ground-based spectroscopic observations are

impeded by telluric contamination, and technical constraints from issues of slit placement and similar concerns further complicate the use of ground-based spectroscopy. All these factors combine to reduce the applicability of high-resolution slit spectroscopy to studying a wider array of sources.

Alternative methods are available. Broadband photometry alone can be used to fit galaxy spectral energy distributions (SEDs) and thereby obtain redshifts (photo-zs) and other properties derived from the SED (Conroy, 2013, and references therein). With a sufficient number and wavelength range of photometric bands, these derived properties can be statistically accurate for a large sample. However, degeneracies in SED colors open up photometric fits to catastrophic errors. For example, the age of a galaxy's stellar population and the abundance of heavier elements in the galaxy (its metallicity) can each contribute to giving a galaxy's SED a redder color (Worthey, 1994), making it difficult to separate the effects of each, and thus to measure them. This makes it risky to rely on photometry-derived properties alone when studying specific objects or smaller samples, requiring follow-up spectroscopy for confirmation (Sawicki et al., 1997; Liu & Green, 1998; Pirzkal et al., 2013). This difficulty can be ameliorated somewhat with the introduction of narrowband photometry, which can measure emission lines with increased accuracy (Boroson et al., 1993), but these detections are limited to a narrow redshift window defined by the width of the narrowband.

Low-resolution wide-field slitless spectroscopy debuted at Lick Observatory (Palmer, 1903), and developed into an efficient and accurate method for identifying emission lines (Wasilewski, 1983) and measuring redshifts (Smith, 1978). The low-resolution of grisms and their lack of slit/mask limitations meant grism surveys could reach a given S/N for a number of objects with greater efficiency, though these surveys were still limited by atmospheric contamination. With the launch of the Hubble Space Telescope (HST), the technique of space-based grism slitless spectroscopy began with surveys with the

Near-Infrared Camera and Multi-Object Spectrograph (NICMOS; McCarthy et al., 1999), and produced numerous following surveys. This method proved capable of expanding the reach of observations to fainter galaxies, detecting objects at lower mass and greater distance.

1.3 The Faint Infrared Grism Survey

The Faint Infrared Grism Survey (FIGS) is an HST cycle 22 Treasury program (Proposal ID: 13779, PI: S. Malhotra) using HST's Wide-Field Camera 3 (WFC3) G102 near-infrared grism. The FIGS observations targeted four fields, whose positions are shown in Figure 1, and are designated as GN1, GN2, GS1, and GS2. GN1 and GN2 are in the GOODS-North region (Giavalisco et al., 2004; Grogin et al., 2011; Koekemoer et al., 2011), and GS1 and GS2 are in GOODS-South. The GS1 field is at the same location as the Hubble Ultra Deep Field (HUDF), and GS2 is at the same location as the Hubble parallel field UDF-PAR2.

FIGS took 40 orbits of WFC3 G102 observations in each field, thereby measuring deep NIR slitless spectra for thousands of individual galaxies. The background on the FIGS observations and data reduction are described in detail in Pirzkal et al. (2017).

1.4 Research Outline

FIGS measured spectra for thousands of galaxies with no pre-selection of objects and significant depth of observations, producing a dataset capable of numerous scientific applications. In this thesis, I explore a number of those applications, in order to probe the nature of galaxy evolution for fainter galaxies at $z < 2$.

In Chapter 2, we combine the FIGS spectra with catalogs of broadband photometry in order to compute combined spectrophotometric redshifts (SPZs). As described previously, purely photometric redshifts are subject to a number of uncertainty-producing observational

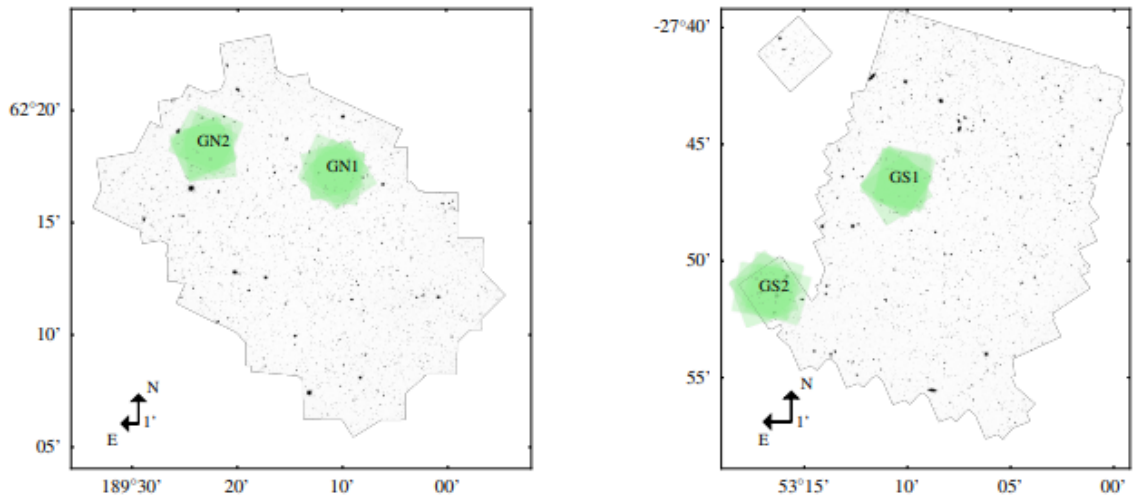

Figure 1: The locations of the four FIGS fields, using a figure from Pirzkal et al. (2017). The left panel shows the two fields in the GOODS-N region, and the right shows the two in GOODS-S. GS1 is at the same location as the HUDF, and GS2 is at the same place as UDF-PAR2.

degeneracies. These degeneracies can be broken by the addition of spectroscopic data, either through follow-up high-resolution spectroscopy or the addition of grism data to the redshift fit (Ryan et al., 2007). After producing an accurate SPZ catalog, we use the FIGS redshifts to measure the local density of galaxies in the FIGS fields at a range of redshifts, using the nearest-neighbor density metric (Papovich et al., 2010; Gobat et al., 2011). This technique provides an assessment of a galaxy's environment, discussed more in Chapter 4, and enables a systematic search for overdensities of galaxies, which may be candidate galaxy clusters or groups. We catalog the significant overdensity candidates found via this method in the FIGS fields.

In Chapter 3, we search for candidate Emission Line Galaxies (ELGs) in the GS1/HUDF FIGS field. We develop an algorithm for identifying emission lines in 1D spectra, and confirm candidates identified this way by using matching optical spectra (Xu et al., 2007; Bacon et al., 2017), including higher-resolution spectra from the VLT/MUSE instrument. We measure emission line fluxes for the Hα λ6563 and Hβ λ4861 Balmer recombination

hydrogen lines, and for the [OIII]$\lambda\lambda$4959,5007 and [OII]$\lambda\lambda$3727,3729 forbidden transition lines. For 14 objects, we are also able to measure the faint [OIII]$\lambda 4363$ auroral emission line. The fluxes of these emission lines can be used to measure the star formation rates (Kennicutt, 1998) and gas-phase metallicities (Izotov et al., 2006) of galaxies. We use the FIGS emission lines to place these objects on the Mass-Metallicity Relation (Tremonti et al., 2004) and the Fundamental Metallicity Relation (Mannucci et al., 2009), and compare to studies at different redshifts, discussing possible implications for star formation.

In Chapter 4, we take the method for identifying emission lines used in Chapter 3 and apply it to finding ELGs in all four FIGS fields. We present a catalog of emission line IDs, line fluxes and errors, line-derived redshifts, and rest-frame line equivalent widths (EW) for Hα, [OIII]$\lambda\lambda$4959,5007, and [OII]$\lambda\lambda$3727,3729 emitters. We also derive SFRs and stellar masses, and then place the FIGS ELGs on the specific star formation (SSFR, or SFR per stellar mass) versus mass plane, commonly known as the galaxy main sequence (Noeske et al., 2007). By using the nearest-neighbor and overdensity catalog derived in Chapter 2, we study line emission properties as a function of galaxy environment.

In Chapter 5, we study the flux ratio of two common tracers of star formation, the Hα emission line flux and the far-ultraviolet (FUV) continuum (Kennicutt, 1998), for 15 FIGS galaxies. We compare the tracer ratio to those measured in previous surveys (Meurer et al., 2009; Weisz et al., 2012) and find that we observe a wider variation in the Hα-FUV ratio at a given R-band surface brightness compared to these other results. We add a sample of "green pea" line emitters with high Hα-FUV ratios and search for correlations with other line emission properties of ELGs. The ratio of [OIII]$\lambda\lambda$4959,5007 to [OII]$\lambda\lambda$3727,3729 proves to be the most significant correlation, and we use BPASS stellar models (Eldridge et al., 2017) and CLOUDY photoionization models (Ferland et al., 2017) to explain this

correlation and the Hα-FUV ratio variation as a function of the age and metallicity of the stellar population.

In Chapter 6, we summarize the key results and conclusions of the studies presented in this work.

Chapter 2

SPECTROPHOTOMETRIC REDSHIFTS IN THE FAINT INFRARED GRISM SURVEY: FINDING OVERDENSITIES OF FAINT GALAXIES

2.1 Abstract[1]

We improve the accuracy of photometric redshifts by including low-resolution spectral data from the G102 grism on the Hubble Space Telescope, which assists in redshift determination by further constraining the shape of the broadband Spectral Energy Disribution (SED) and identifying spectral features. The photometry used in the redshift fits includes near-IR photometry from FIGS+CANDELS, as well as optical data from ground-based surveys and HST ACS, and mid-IR data from Spitzer. We calculated the redshifts through the comparison of measured photometry with template galaxy models, using the EAZY photometric redshift code. For objects with F105W < 26.5 AB mag with a redshift range of $0 < z < 6$, we find a typical error of $\Delta z = 0.03 * (1 + z)$ for the purely photometric redshifts; with the addition of FIGS spectra, these become $\Delta z = 0.02 * (1 + z)$, an improvement of 50%. Addition of grism data also reduces the outlier rate from 8% to 7% across all fields. With the more-accurate spectrophotometric redshifts (SPZs), we searched the FIGS fields for galaxy overdensities. We identified 24 overdensities across the 4 fields. The strongest overdensity, matching a spectroscopically identified cluster at $z = 0.85$, has 28 potential member galaxies, of which 8 have previous spectroscopic confirmation, and features a corresponding X-ray signal. Another corresponding to a cluster at $z = 1.84$ has 22 members, 18 of which are

[1]This chapter previously published as Pharo et al. (2018)

spectroscopically confirmed. Additionally, we find 4 overdensities that are detected at an equal or higher significance in at least one metric to the two confirmed clusters.

2.2 Introduction

The redshift interval $z \sim 1 - 3$ includes the era of peak star formation, and it hosts the greatest density of galaxy mergers (Madau & Dickinson, 2014). Measuring accurate redshifts of such distant galaxies is a difficult problem, and many objects in this range lack the high-resolution, ground-based spectroscopy that produces the most-accurate redshifts, particularly the less-massive, fainter objects. The method of fitting spectrophotometric grism redshifts provides the opportunity to get more precise redshift measurements for such objects.

Observing the objects present in this cosmic epoch provides vital information in the study of the formation and assembly of galaxies and of large scale structure (LSS) in the transition from the epoch of reionization to the modern low-redshift universe, and is vital to understanding our cosmic origins. However, the study of objects at such substantial redshifts necessarily introduces completeness problems: as the distance increases, lower-luminosity objects become more difficult to measure at a useful signal level, and thus may be rendered indistinguishable from low-redshift objects that are particularly faint or dust-extinguished. When conducting a study of high-redshift objects, the loss of the faint population biases the sample, and limits the conclusions that may be drawn (Bouwens et al., 2015; Finkelstein et al., 2015).

Mitigating this issue requires deep observations of the faint galaxy population to address the problem of completeness, and in order to be useful, those observations will require definitive measurements of that population's redshift. Determination of a galaxy's redshift

generally requires measurement of easily identifiable features in the galaxy's spectrum, such as known strong emission or absorption lines (eg, Hα) or characteristic breaks (the Lyman break and the 4000 Å break). If an object has more than one detected emission line, the wavelength ratio of the two can identify the spectral lines, whose observed wavelengths in turn pinpoint the redshift. However, not all objects will have detectable emission lines, and emission line signal-to-noise ratio will tend to decrease as the measured object gets fainter. Without emission lines, the location of a break (where the continuum flux level changes significantly) becomes the primary method of redshift identification (Steidel et al., 1996).

This is most easily and accurately accomplished with the $R \sim 1000 - 2000$ spectra offered by ground-based instruments, but for increasingly distant and faint objects, ground-based spectroscopy becomes untenable. The break can also be detected in flux changes in photometric measurements. Photometric redshift fitting codes such as BPZ (Benítez, 2000), Hyper-Z (Bolzonella et al., 2000), LePhare (Ilbert et al., 2006), and EAZY (Brammer et al., 2008) accomplish this by fitting broadband measurements against sets of template galaxy spectra. However, since the spectral coverage of a typical photometric band can cover $\sim$1000 Å, this method lacks sufficient observations to fully constrain the fit, and thus is prone to significant systematic errors in the redshift identification.

By combining low- to mid-resolution HST grism spectra with ground-based broadband photometry, Ryan et al. (2007) was able to achieve a fractional standard deviation of $\Delta z/(1+z_{spec}) \sim 0.04$, where Δz is the difference between the grism calculated redshift and the ground-based spectroscopic redshift. This made a noticeable improvement over the purely photometric redshifts, which measured $\Delta z/(1+z_{spec}) \sim 0.05$. This demonstrated that the addition of grism data could provide significant improvement in the calculations of redshifts for faint objects by identifying spectral features, and we find an improvement of

the same order with this method. Similar methods were developed with G141 grism data in the 3D-HST survey (Brammer et al., 2012; Momcheva et al., 2016).

In this paper, we present the catalog of SPZs developed for the Faint Infrared Grism Survey (FIGS) and our analysis of its quality. In §2.3, we describe the observations and data reduction methods for the FIGS spectra. In §2.4, we describe the computation of SPZs using EAZY. In §2.5, we present our results, and measure the redshift accuracy in comparison to ground-based spectroscopic redshifts. In §2.6, we explore the applications of this method to the study of LSS, and in §2.7 we address the implications of this study for future surveys. We summarize our conclusions in section §2.8. Throughout this paper, we use AB magnitudes, and Λ-CDM cosmology with $H_0 = 70.0$ km s^{-1}Mpc^{-1}, Ω_m=0.27, and $\Omega_\lambda = 0.73$.

2.3 Data and Methods

2.3.1 FIGS Observations and Spectral Extraction

2.3.1.1 Survey Description

The Faint Infrared Grism Survey (FIGS, HST/Cycle 22, ID:13779, PI S. Malhotra) used the HST WFC3-G102 infrared grism to obtain deep slitless spectroscopy of $\sim$ 6000 galaxies. FIGS achieved 40-orbit depth in 4 fields, designated GN1, GN2, GS1, and GS2 (see Table 1 for coordinates of each field). Objects in each field were observed in 5 different 8-orbit position angles (PAs) in order to mitigate contamination of the spectra by overlapping spectra from nearby objects. Each PA covers a 2.05'x2.27' field of view. The area of coverage in each field from which we derive the spectra used for SPZs is given in Table 1, for a total area of 17.7 square arcminutes.

Table 1: A description of the four FIGS fields.

Field	RA	Dec	Area[a]
GN1	12:36:41.4670	+62:17:26.27	4.51
GN2	12:37:31.0234	+62:18:26.91	5.06
GS1[b]	03:32:40.9514	–27:46:47.92	4.09
GS2	03:33:06.4675	–27:51:21.56	4.02

[a] Measured in arcmin^2.
[b] The HUDF.

2.3.1.2 1D and 2D Spectral Extraction

The FIGS G102 data reduction is described in detail in (Pirzkal et al., 2017). FIGS data were reduced in a manner that loosely follows the method used for GRAPES and PEARS, previous HST grism surveys (Pirzkal et al., 2004). First, we generated a master catalog of sources from deep CANDELS mosaics in the F850LP filter in ACS and the F125W and F160W filters in WFC3 (approximately the z, J, and H bands) (Grogin et al., 2011; Koekemoer et al., 2011). These mosaics provided absolute astrometric reference points for the FIGS F105W direct images and G102 dither exposures, along with individual FIGS F105W images. Contamination and background measurements were subtracted, and then 2D spectra were extracted using a process similar to that provided by the aXe extraction software (Kümmel et al., 2009). The final product is a set of multi-extension FITS files that each contain the spectrum of a science object, an error estimate, the object's contamination model, and its effective exposure map. Sources were extracted down to F105W < 29.0 mag.

One dimensional extractions were created from the 2D-extractions using two methods: Non-weighted extraction and Optimal extraction. The results in this paper were obtained using spectra made via Optimal extraction, which follows a non-iterative version of the algorithm described in Horne (1986). We used the simulated version of the 2D dispersed spectrum of the source to determine the expected profile of the spectrum as a function of

wavelength. This profile was normalized to unity in the cross dispersion direction and used as the extraction weight. This extraction weight was then used in combination with the 2D contamination subtracted 2D data, to produce an optimally extracted 1D spectrum. The optimal extraction has the advantage of producing higher S/N spectra with improved flux calibration, but only when the extraction weights (derived from the imaging data) are accurate.

2.3.1.3 PA Combination

Because the total data for each of the four fields comes in 8-orbit segments for separate PAs, one must consider how to merge the data in a set of contamination-subtracted PAs in order to achieve the best signal for the largest number of objects. The observed spectra are the convolution of the light profile of the object with its spectrum, and large differences in this light profile between different PAs (for example, in the cases of elliptical or irregular galaxies) will result in spectra that disagree strongly near the edge of the bandpass of the grism. They will also have continuum fluxes that are in disagreement, as the spectrum is smoothed by different amounts. We derived an object-specific spectral response for each source by dividing the extracted 1D data by the extracted 1D simulated data, and by the spectral energy distribution used to generate the FIGS simulations, which were generated from the available FIGS broad band photometry. The result is a normalized spectrum, which can be scaled back to the observed F105W photometry. These steps insure that the 1D spectra of extended sources are accurately flux-calibrated and avoid the issue of having a point-source sensitivity function applied to an extended object.

The FIGS spectra were flux calibrated using object specific sensitivity functions and then combined. For each wavelength bin, the inverse variance of the single PA spectra were used as weights to compute the weighted mean and standard deviation of the weighted mean.

Table 2: A description of the spectra samples of the four FIGS fields.

Field	Initial[a]	Not Matched[b]	Too Faint[c]	Low $\mathcal{N}$[d]	Bad Synthetic Flux[e]	Aperture Ratio[f]	Final[g]
GN1	1913	263	812	241	21	25	551
GN2	1003	84	161	222	20	50	466
GS1	3106	390	1917	241	11	32	515
GS2	2623	819[h]]	1223	194	13	27	347
Total	8645	1556	4113	898	65	134	1879

[a] The number of combined 1D spectra in each field, before any quality cuts have been made.

[b] The number of objects with spectra without additional matched photometric data (See §2.3.2.1).

[c] The number of objects with spectra and matching photometry, but with F105 > 26.5 mag.

[d] The number of objects with spectra and matching photometry, but with a net spectral significance less than 10 (See §2.3.2.2).

[e] The number of objects meeting previous criteria for which we were unable to calculate a synthetic F105W magnitude.

[f] The number of objects meeting previous criteria but rejected for having a large aperture correction or less than 90% full coverage. (See §2.3.2.3)

[g] The number of objects in each field that pass all quality criteria and are used in the final SPZ sample.

[h] GS2 lacks deep WFC3 imaging at some roll angles. See §2.3.2.1.

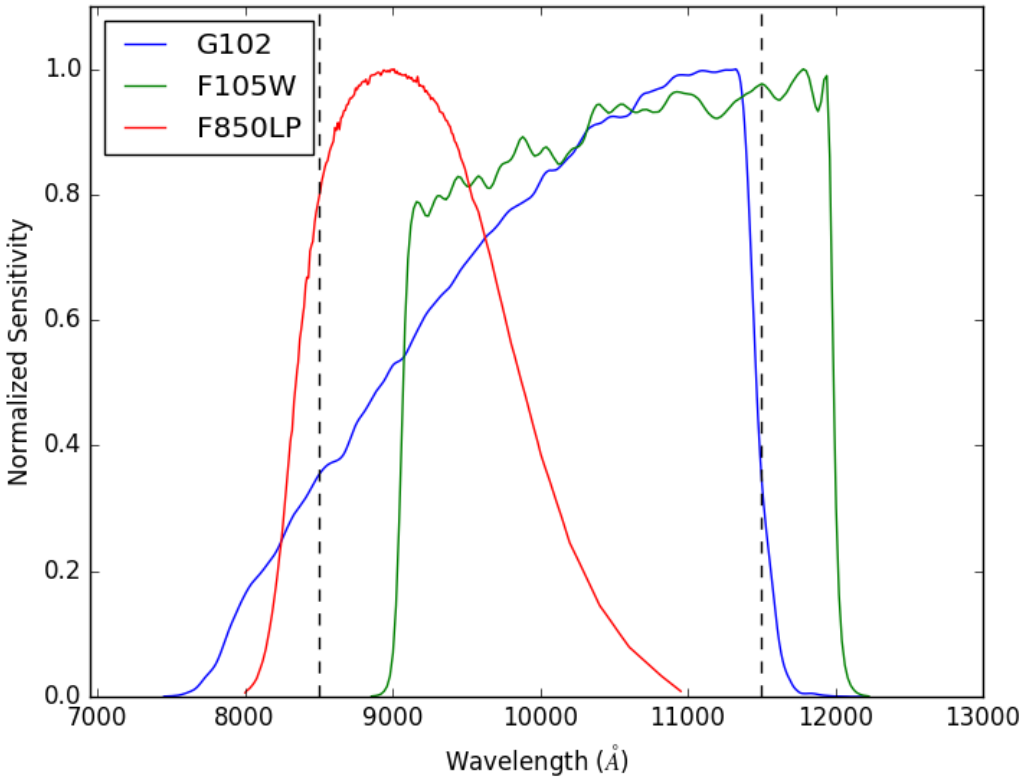

Figure 2: The sensitivity curves for the WFC3/G102 grism, as seen in Kuntschner et al. (2011), and the F105W and F850LP filters. The dashed vertical lines show the cutoffs for grism data used in the construction of redshifts. The curves have been normalized to their maximum sensitivity.

An iterative 3σ rejection was used to remove outlier single PA spectral bins.

2.3.2 The Sample

The sample of FIGS spectra used are described in detail in the following section, the results of which are summarized in Table 2.

2.3.2.1 Broadband Photometric Data

Given that the wavelength coverage of FIGS spectra is limited to the 8500-11500 Å wavelength range, additional data are often useful for constraining the parameters of the redshift fit. To extend the spectral range of the fit, we supplement the FIGS spectra and photometry with optical and mid-IR broadband photometry available from previous surveys: GOODS (Dickinson et al., 2003; Giavalisco et al., 2004), CANDELS (Koekemoer et al., 2011), MODS (Kajisawa et al., 2011), SEDS (Ashby et al., 2013), and HHDFN (Steidel et al., 2003; Capak et al., 2004). See Tables 3 and 4 for specific details on the broadband data used. We obtained these measurements from the combined, PSF-matched catalogs produced by 3D-HST (Skelton et al., 2014).

Because FIGS is targeting faint objects, there are some detected FIGS spectra for which we are unable to find matching photometry. These objects amount to $\sim 10\%$ of the objects in GN1, GN2, and GS1 (HUDF), and a number of these spectra would later be rejected for other reasons (eg, low spectral signal). To cut down on spectra for which we could not expect a useful signal, we then applied a magnitude cutoff at F105W < 26.5 mag.

About a third of the GS2 spectra, however, lack the matched photometry described in Table 3. GS2 is centered on one of the HUDF parallel fields outside GOODS-S, and parts of the FIGS WFC3-IR field lie outside the deepest WFC3 imaging data for some roll angles. If we check other criteria to identify usable spectra before photometric matching first, we find that there is an average of 40 objects per field which have viable FIGS spectra but do not have an existing match in the catalogs compiled by 3D-HST. Redshifts can still be computed successfully for these objects, though they lack significant constraints in the NIR and IRAC

Table 3: Sources of Broadband Photometry

Filters	Telescope/Instrument	Survey	Reference
U[1]	KPNO 4m/Mosaic	Hawaii HDFN	(Capak et al., 2004)
U, R[2]	VLT/VIMOS	ESO/GOODS	(Nonino et al., 2009)
U38, B, V, R_c, I[2]	WFI 2.2m	GaBoDs	(Hildebrandt et al., 2006; Erben et al., 2005)
G, R_s[1]	Keck/LRIS	Hawaii HDFN	(Steidel et al., 2003)
F435W, F606W, F775W, F850LP	HST/ACS	GOODS	(Giavalisco et al., 2004)
B, V, I_c, z'[1]	Subaru/Suprime-Cam	Hawaii HDFN	(Capak et al., 2004)
F140W	HST/WFC3	3D-HST	(Brammer et al., 2012)
F125W, F160W	HST/WFC3	CANDELS	(Koekemoer et al., 2011)
J, H, K_s[1]	Subaru/MOIRCS	MODS	(Kajisawa et al., 2011)
J, H, K_s[2]	VLT/ISAAC	ESO/GOODS, FIREWORKS	(Retzlaff et al., 2010; Wuyts et al., 2008)
3.6, 4.5 μm	Spitzer/IRAC	SEDS	(Ashby et al., 2013)
5.8, 8 μm	Spitzer/IRAC	GOODS	(Dickinson et al., 2003)

[1] Northern fields

[2] Southern fields

Table 4: Broadband Photometry Depths

Filter	5σ Depth (N)	5σ Depth (S)	$\lambda_{central}$ (Å)	Width(Å)
U	26.4	-	3593	721
R	26.2	27.5	6276	1379
U38	-	25.7	3637	475
B	26.7	26.9	4448	1035
V	27.0	26.6	5470	993
R_c	-	26.6	6517	1600
I	25.8	24.7	7671	1489
G	26.3	-	4751	940
R_s	25.6	-	6819	1461
F435W	27.1	27.3	4318	993
F606W	27.4	27.4	5919	2225
F775W	26.9	26.9	7693	1491
F850LP	26.7	26.5	9036	2092
z'	25.5	-	9028	1411
F140W	25.9	25.6	13924	3760
F125W	26.7	26.1	12471	2876
F160W	26.1	26.4	15396	2744
J	25.0	25.1	12517	1571
H	24.3	24.5	16347	2686
K_s	24.7	24.4	21577	3044
IRAC1	24.5	24.8	35569	7139
IRAC2	24.6	24.8	45020	9706
IRAC3	22.8	23.0	57450	13591
IRAC4	22.7	23.0	79158	27839

bands, potentially increasing errors, so we exclude such objects from the calculations in this paper. See §2.4 for a further discussion.

2.3.2.2 Net Significance

As described in the instrument calibration report (Kuntschner et al., 2011), the WFC3 G102 grism achieves a maximum throughput of 41% at 11000 Å and provides $\geq 10\%$ system throughput in the wavelength range $8035 - 11538$ Å (see Figure 2). At longer wavelengths, the throughput declines rapidly, making this the effective useful range of the

spectra. We assess the content of the individual spectra by computing the net significance (Pirzkal et al., 2004), which is determined by reordering the resolution elements in order of descending signal-to-noise (S/N) ratio, and then iteratively computing a cumulative S/N ratio from the current element and all lower elements. This continues until a maximum S/N ratio is computed. After the cumulative S/N ratio turns over, adding additional data will not increase the S/N ratio. The maximum is then the net significance of the spectrum, $\mathcal{N}$. As described in Pirzkal et al. (2017), a simulated FIGS spectrum with a continuum level of 3σ per bin is expected to have $\mathcal{N} \approx 4.5$. It is possible to obtain an artificially high value of $\mathcal{N}$ for an object if there is unaccounted contamination or errors in the level of background subtration. In order to avoid such objects and to ensure we used only objects with high signal, we imposed a netsig cutoff of $\mathcal{N} > 10$. This eliminates 7-20% of the initial number of objects in each field. Though it is still possible for contaminated or otherwise low-signal objects to bypass this cutoff, such objects are likely to be caught by further quality cuts.

2.3.2.3 Aperture Correction

Because the spectra will need to be combined with photometry in order to cover the wavelength range needed for a redshift fit, the flux values in the spectra need to be scaled to match those of photometric images. To do this, we define an aperture correction, which is the flux ratio between a photometric flux and a synthetic flux calculated from the spectrum in the same band, as described in Ryan et al. (2007). Figure 2 shows the grism throughput curve plotted against the two nearest HST broadband filters: F850LP and F105W. Both filters extend past the usable wavelength range of the grism, but the F105W band has the closest filter profile correspondence to the grism throughput, since the F850LP sensitivity anticorrelates with that of the grism, resulting in a much broader distribution of aperture

corrections. Consequently, we defined the aperture correction $\mathcal{A}$ in terms of a synthetic F105W band, calculated by integrating over the product of grism spectra with the F105W filter curve:

$$\mathcal{A} = \log_{10}\left(\frac{\text{F105W(obs)}}{\text{F105W(synth)}}\right) \tag{2.1}$$

If for some reason a synthetic F105W flux cannot be calculated from the spectrum (usually if oversubtraction of contamination left most of the fluxes negative), that spectrum is rejected for SPZ use.

The distribution of the aperture corrections in each field is displayed in Figure 3. The widths of the aperture correction distributions are a function of the spectral extraction method, the broadband apertures, and spectral contamination from nearby objects. However, as noted above, the F105W filter profile goes significantly redder than the G102 wavelength coverage. If an object spectrum in that region is not flat, then the aperture correction produced is likely to be quite large.

In all the fields, the distribution peaks sharply near 0, and the distributions feature a negative tail, indicating a tendency of the synthetic F105W measurements to exceed that of the HST photometry. The shape of this distribution becomes clearer when looking at Figure 4, which displays the aperture correction as a function of F105W magnitude (a proxy for the brightness of the spectrum). The aperture corrections only begin to strongly diverge from 0 for fluxes fainter than ~ 25.5 mag, with the most deviant objects typically found at the very faintest magnitudes. This is likely a function of contamination, which will make up a larger fraction of the total measured flux in an object with a faint true brightness. Consequently, accurately estimating the contamination in such objects is more difficult, increasing the likelihood that a faint object will retain some contaminating flux. Faint contaminated objects

are therefore more likely to have synthetic F105W measurements that are significantly larger than the broadband measurement, hence the negative tail in the distribution. To avoid the influence of such objects, we imposed a cutoff in aperture correction where any object with a ratio off from unity by a factor of 10 or more is rejected. Across all four fields, an average of 6% of the initial sample was rejected for this reason. This correction does not account for any objects whose continuum slope has been altered by the presence of unaccounted background or contamination, which may pass through the aperture correction if the overall integrated flux doesn't change much. Such objects were later weeded out via visual inspection.

Some objects do not have a measurement in all 5 PAs, and some PAs don't measure the flux across the total G102 wavelength range. This usually does not cause any issues with the combination of the different PAs, but it may if the only PAs with data do not have overlapping coverage. This can result in combined spectra with gaps in the flux, and such spectra tend to produce very confused results in the redshift fit. These and any other spectra with missed contamination were rejected by visual inspection. These final removals typically amounted to $\sim$1% of the initial sample.

2.4 Redshift Estimation

2.4.1 Photometric Fitting Code

To estimate the redshifts, we used EAZY (Brammer et al., 2008), a public photometric redshift code. A systematic comparison of 9 different photometric redshift codes (including EAZY) across 11 different photometric redshift catalogs (Dahlen et al., 2013) found that no particular code obtained significantly more accurate photometric redshifts compared to the

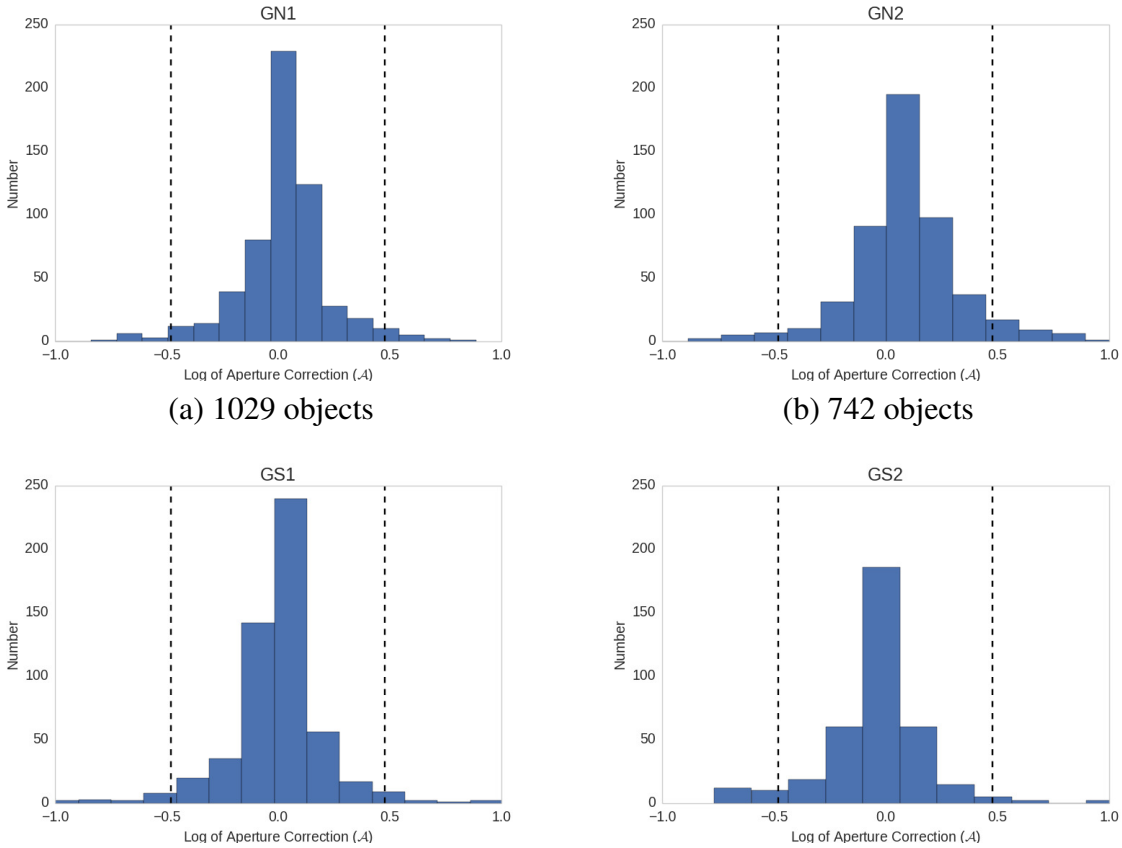

(a) 1029 objects

(b) 742 objects

(c) 1163 objects

(d) 805 objects

Figure 3: The distributions of $\mathcal{A} = \log_{10}(\text{F105W(obs)}/\text{F105W(synth)})$ in each field: (a) GN1 (b) GN2 (c) GS1 (d) GS2. These histograms are given in terms of the log of the ratio of the measured broadband F105W flux to the synthetic F105W flux, so a value of 0 indicates a 1:1 ratio. Bin widths are consistent for all four plots. To get a sense of the shape of each distribution, a Gaussian was fit to the distributions, and the FWHM calculated.

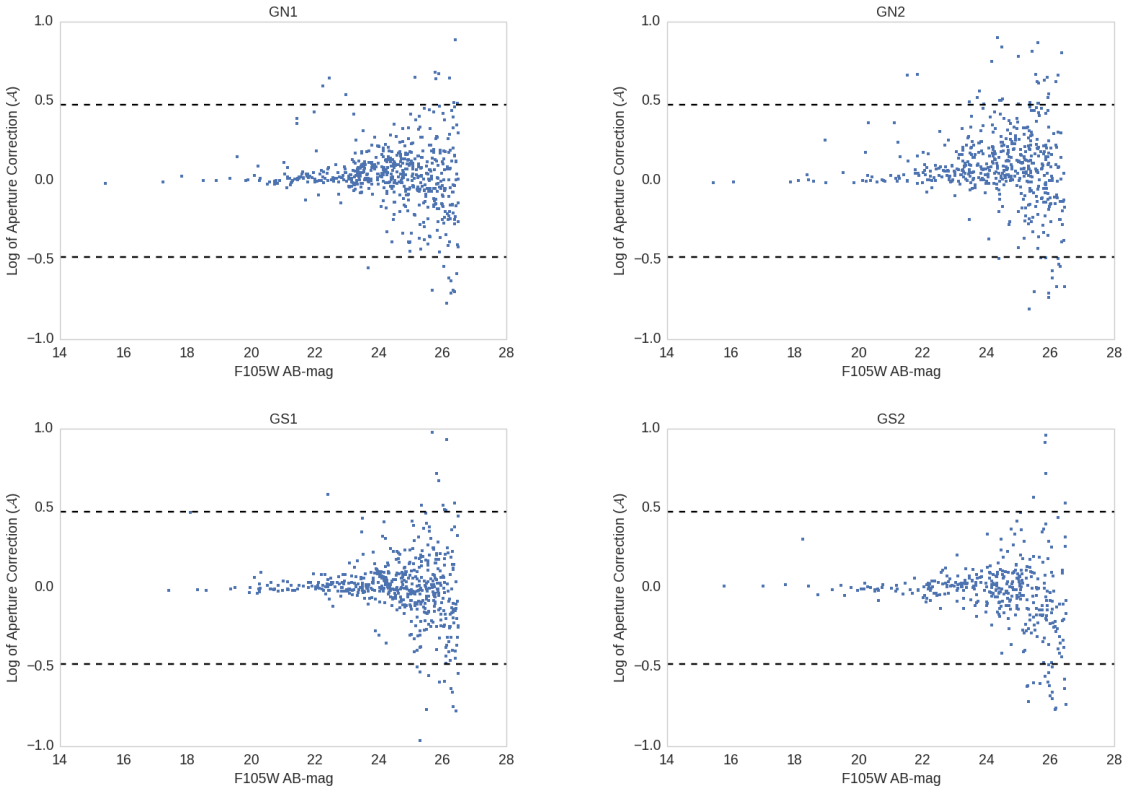

Figure 4: The aperture correction distributions ($\mathcal{A} = \log_{10}$ (F105W(obs)/F105W(synth))) as a function of F105W magnitude in each field: (a) GN1 (b) GN2 (c) GS1 (d) GS2. The aperture correction is given in terms of the log of the ratio of the measured broadband F105W flux to the synthetic F105W flux, so a value of 0 indicates a 1:1 ratio.

others. Given this, we use EAZY for its modifiability that allows the simple inclusion of grism data alongside photometry.

Given a set of photometric points and corresponding errors, EAZY can iterate over a grid of redshifted spectral templates, calculating synthetic fluxes to compare to the measured photometry. The differences between the synthetic templates fluxes and the observed fluxes are used to define a χ^2 statistic. This χ^2 is minimized across the range of template spectra and redshifts to find the best-fit template and redshift. EAZY's template spectra are derived from a library of ~ 3000 PÉGASE spectra (Fioc & Rocca-Volmerange, 1997), including spectra with variable-strength emission lines. Using the method of non-negative matrix

factorization (Blanton & Roweis, 2007), Brammer et al. (2008) were able to reduce the large template set to a set of 5 basis templates that, in linear combination, can represent the full range of colors of the initial set. These basis templates, along with a dusty starburst template (a Calzetti extinction law is applied), make up the template set EAZY uses for fitting.

Despite the breadth of this template set, there remains uncertainty in the spectral properties (eg, variations in dust extinction) that go into constructing template galaxies, which may result in mismatches between the templates and an observed galaxy. To account for this, EAZY provides a template error function to account for this uncertainty when fitting observations to the templates. The template error function provides a per-wavelength error in the template flux derived from the residuals of a large set of redshift fits. This allows the template set to accomodate observational spectral variations that aren't accounted for in the physics from which the templates are derived.

Furthermore, to avoid degeneracies in the redshift fitting wherein the redshift probability distribution produces more than one peak, EAZY also provides a grid of magnitude priors in R- and K-bands, which assigns probabilities to measuring a band at a certain brightness at a given redshift, a technique first applied in Benítez (2000). This typically reduces the incidence of catastrophic failures, where the difference between the grism redshift and spectroscopic redshift is more than 10% of (1+z_{spec}), by providing a mechanism for avoiding wrong-peak selection in the case of a bimodal probability distribution. In our sample, we use the R-band magnitude prior, calculated from the observer-frame R-band flux.

2.4.2 Inclusion of Grism Data

To include the FIGS spectra in a photometric fitting code, we followed the procedure in Ryan et al. (2007) and reformatted the spectra into a series of narrow photometric bands

that could be supplied to EAZY alongside broadband photometry. After passing the net significance and aperture correction procedures without rejection, an individual spectrum is divided into sub-samples along its operating wavelength range. The number (and therefore width) of these sub-samples can influence the results of the redshift fit. We experimented with a number of bins ranging from a few (width ~ 750 Å) to treating each grism element as its own bin (a width of 24.5 Å), in order to obtain the best results. Typically, grism points derived from fewer, broader wavelength bins are better at avoiding errors introducted by problems in the combined spectra (eg, over-subtraction of contamination), since each bin will include a larger number of pixels, reducing the influence of one or two bad pixels. However, the redshift quality of the whole sample is best with a larger number of narrower bins, as this allows for the more precise location of breaks and emission lines. The cases where over-subtraction or other errors produce inaccurate results are few enough in number that they can be flagged individually, so we attempted the redshift fits with the narrowest grism bands. Bands narrower than a few grism pixels caused the fitting routine to stall and fail to produce a redshift fit. Consequently, we chose to proceed with grism bands $\sim$140 Å wide (which corresponds to ≤ 22 spectral "pixels" per spectrum), which was the narrowest range to fit successfully. This may not result in any loss of improvement, as the typical spatial scale of objects in FIGS is a few pixels, so the spectra are smoothed to this extent anyway.

The flux in each of these subsamples is integrated to produce a new "narrowband" flux in each sample. These narrowband fluxes are written into an EAZY input catalog alongside FIGS and 3D-HST broadband photometry. EAZY is also given a "filter profile" for each narrowband in the form of a tophat function bound by the wavelength range of the grism band. EAZY provides the option to smooth the filter profiles $R(\lambda)$ by applying a Gaussian such that $\mathcal{R}_i = (1/b_i)\Sigma_j R(\lambda) \cdot G(\lambda_i, \lambda_j, \sigma)$ where G is a Gaussian function and $b_i = \Sigma_j G$. After testing several cases, we obtain the best results with smoothing enabled with $\sigma = 100$

Table 5: A summary of the SPZ and photo-z quality results for the four FIGS fields.

Field	N. Spec-z	F105W[a]	Med(Δz_{SPZ})[b]	Med(Δz_{PZ})[c]	SPZ Outliers[d]	PZ Outliers[d]
GN1	200	23.3	0.019	0.026	0.07	0.08
GN2	147	23.2	0.024	0.028	0.09	0.10
GS1	131	23.5	0.023	0.029	0.09	0.10
GS2	101	23.2	0.027	0.031	0.15	0.16

[a] The median F105W magnitude of the SPZ-spectroscopic comparison sample.
[b] The quantity described is the median value of $(z_{SPZ} - z_{spec})/(1 + z_{spec})$ for the field.
[c] The quantity described is the median value of $(z_{PZ} - z_{spec})/(1 + z_{spec})$ for the field.
[d] This refers to the fraction of objects for which the fits are catastrophic failures, meaning $|(z_{SPZ} - z_{spec})/(1 + z_{spec})| > 0.1$.

Å. We run EAZY on a redshift grid of $z = 0.01 - 6.0$, which is the redshift range tested in EAZY's design, with $\Delta z = 0.01 \cdot (1 + z_{prev})$.

Figure 5 shows an example of EAZY input and output for one of the FIGS objects exhibiting a particularly noticeable 4000 Å break. The location of the break is more obvious at the higher resolution of the grism data, which confine it to a ~ 100 Å wavelength range, as opposed to the ~ 1000 Å coverage provided by the broadband photometry alone.

2.5 SPZ Accuracy

In order to gauge the accuracy of the SPZs compared to photometric redshifts without spectral data (photo-zs), it is helpful to compare the redshifts from both methods to known spectroscopic redshifts (ie, the conventional standard for accurate redshifts). We created a matching set of photometric redshifts for the SPZ objects by simply running the same catalogs through EAZY stripped of their grism measurements, leaving only the broadband photometry as input for the fit.

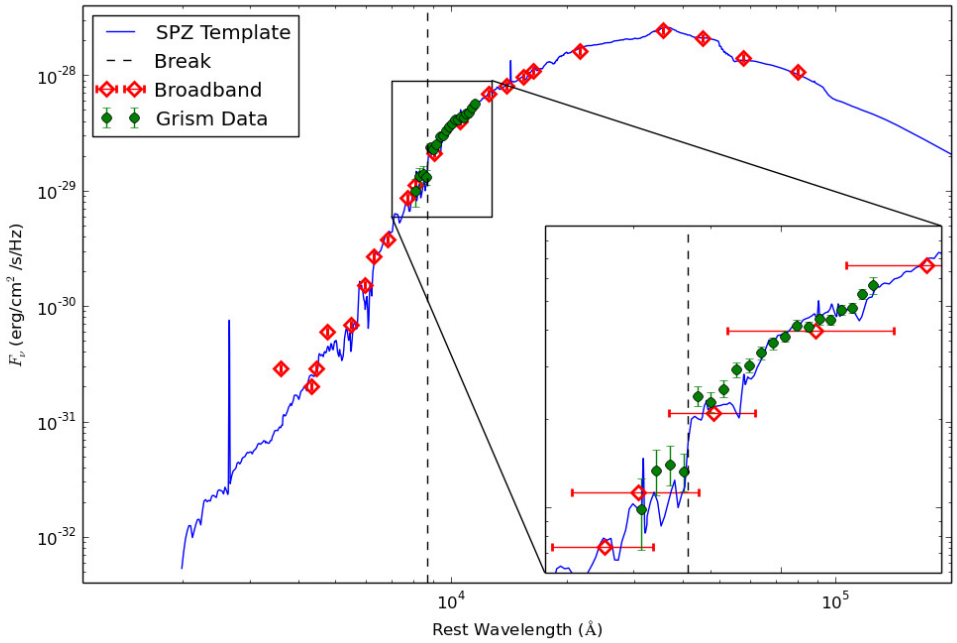

Figure 5: Full: a spectral energy distribution (SED) of an example FIGS galaxy showing the EAZY input and output. Red points are FIGS and 3D-HST broadband data, and green points are the grism spectral data from FIGS. Both sets of points go into EAZY's calculations. In addition to the redshift, EAZY also outputs the template spectrum for which the χ^2 is minimized (shown in blue). Inset: a close-up of the SED around the grism wavelength coverage. Vertical error bars represent the flux error (which is typically too small to see in the broadband), and horizontal error bars represent the effective width of the broadband filters. The wavelength width of the grism points is ~ 140 Å . The dashed line marks the location of the 4000 Å break at the predicted redshift. One can see the break precisely in the narrowband SED as well as in the output template. The input includes photometric points beyond the wavelength range depicted. The wavelengths of the plot were restricted in order to focus on the grism region.

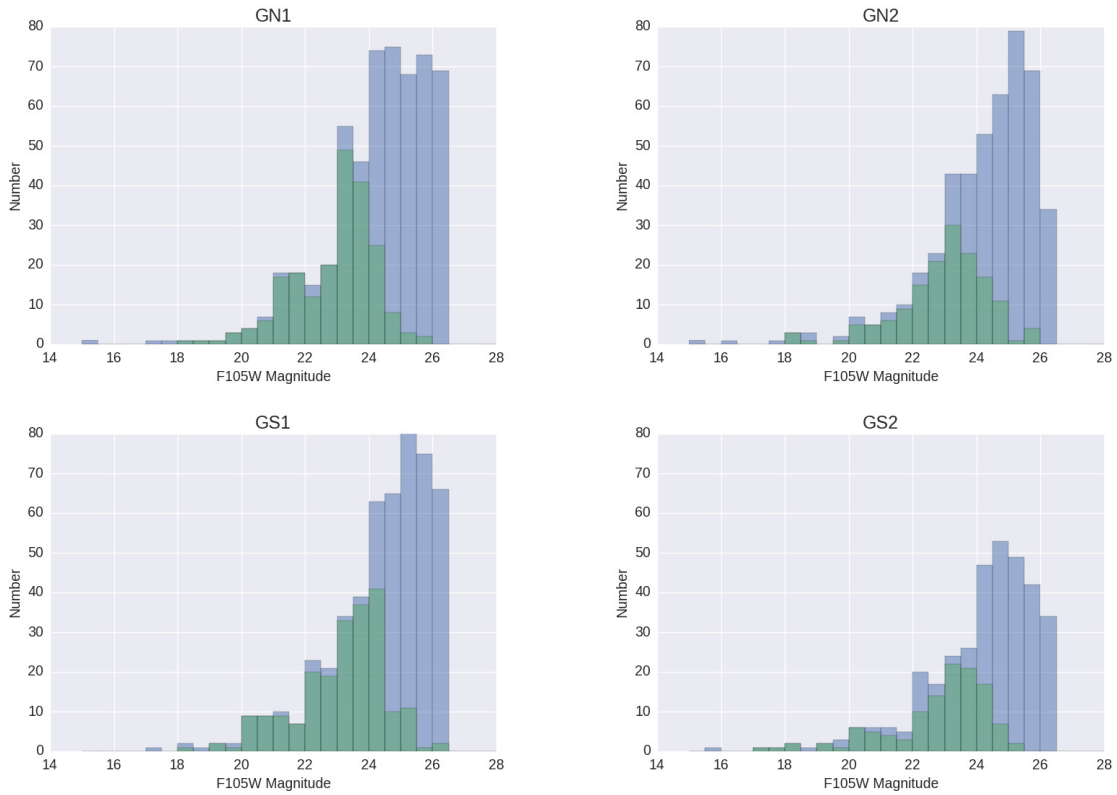

Figure 6: These histograms show the F105W magnitude distribution for each field for the total sample of SPZ objects (blue) and the sample of objects with matching spectroscopic redshifts (green). The median values in each sample are (clockwise from top left): GN1, 24.6 mag for SPZs, 23.3 mag for spec-zs; GN2, 24.6 mag for SPZs, 23.2 mag for spec-zs; GS2, 24.5 for SPZs, 23.2 for spec-zs; GS1, 24.8 mag for SPZs, 23.5 mag for spec-zs.

The SPZ and photo-z catalogs could each be compared to spectroscopic redshifts for the same objects. To find as many matches with confirmed spectroscopic redshifts as possible, we consulted a compilation of public spectroscopic surveys in GOODS-N and CDFS (N. Hathi, private communication). The spectroscopic redshifts in these compilations were assigned quality flags based on the redshift quality indicated in the parent survey. In order to ensure the best possible comparison sample, only the spectroscopic redshifts from the two highest-quality bins were used.

Since the limiting magnitude of the FIGS dataset goes beyond the limits of ground-based

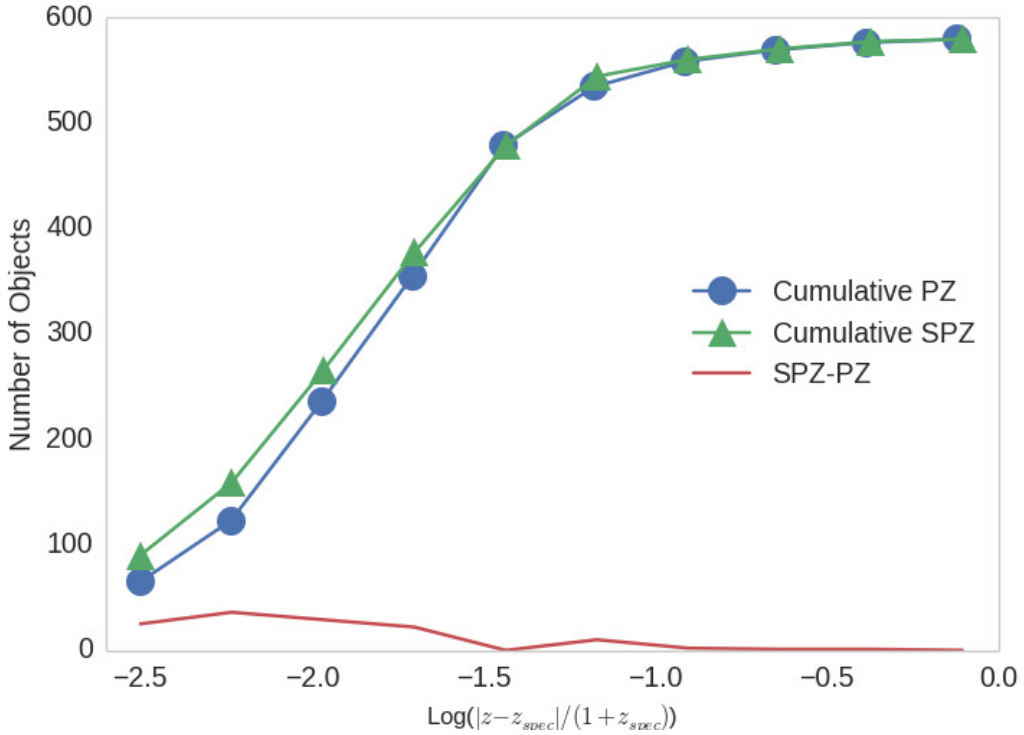

Figure 7: A cumulative count of the SPZ-galaxies starting at $\log(|z - z_{spec}|/(1 + z_{spec})) \leq -2.5$. Triangle points (green) show the number of SPZs at a given or greater accuracy. Circle points (blue) show the number of purely photometric redshifts (PZs) at a given or greater accuracy. The red line is the number of SPZs minus the number of PZs, which demonstrates the excess of SPZs in the most accurate bins.

spectra, one should expect objects with spectroscopic redshifts in the FIGS fields to be readily detected. Consequently, these objects can be found using simple (RA,DEC) matching. This was done with a separation tolerance of 1 arcsecond to account for offsets in different surveys, though for the vast majority of matches the separation is much smaller. This matched set of spectroscopic redshifts was then assured to provide a high-accuracy comparison for the matched SPZs. The number and magnitudes of the SPZ-spectroscopic comparison sample are given in Table 5, and a comparison of magnitudes between the spectroscopic redshifts and the total sample of SPZ objects are given in Figure 6.

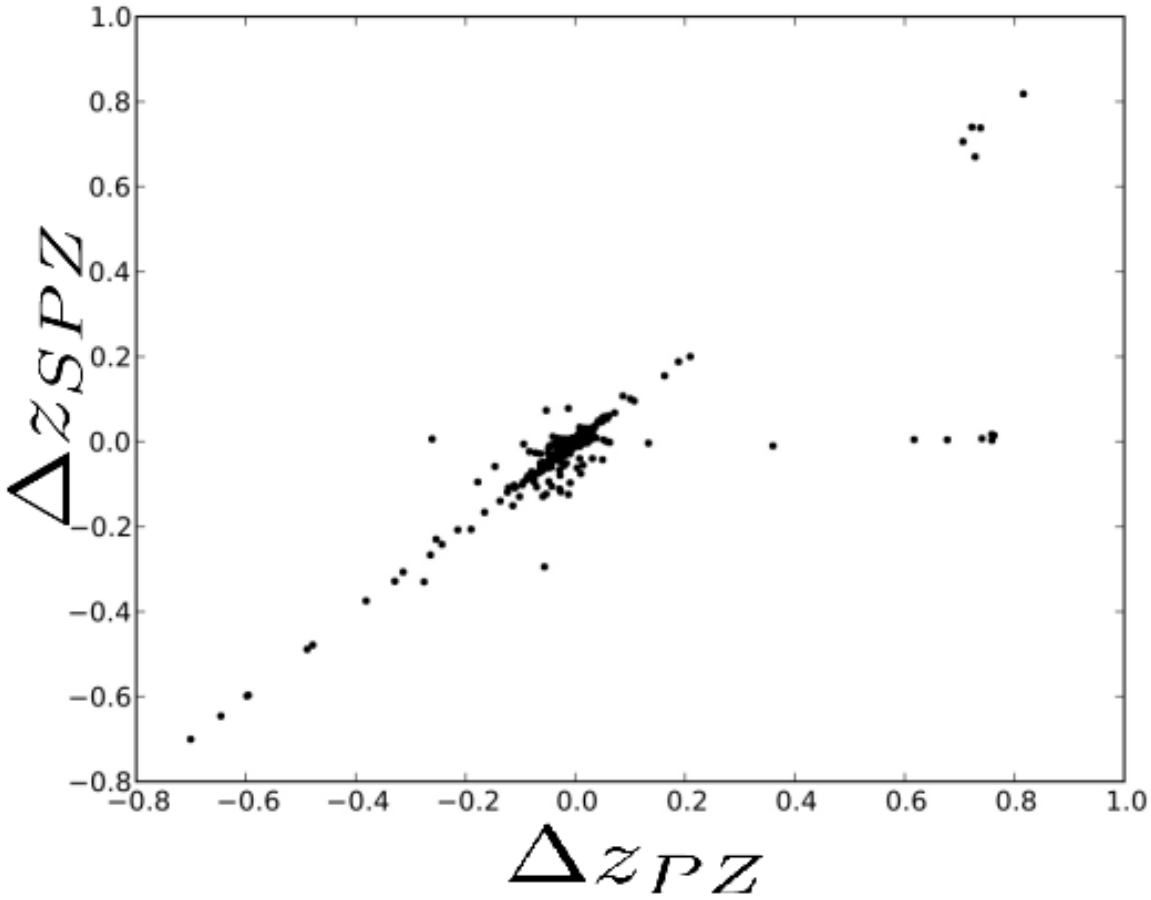

Figure 8: A plot of the SPZ difference $\Delta_{SPZ} = (z_{SPZ} - z_{spec})/(1 + z_{spec})$, vs the photo-z difference $\Delta_{PZ} = (z_{PZ} - z_{spec})/(1 + z_{spec})$. This illustrates the cases where the method of redshift calculation can make a significant change. One can see a number of objects where the photometric redshift produces a $D_{PZ} > 0.1$, a catastrophic failure, while the D_{SPZ} is quite low.

For FIGS objects with existing spectroscopic redshifts of the highest accuracy, we calculate the term:

$$\Delta z_{SPZ} = \frac{z_{SPZ} - z_{spec}}{1 + z_{spec}} \tag{2.2}$$

This measures the closeness of each SPZ redshift to the true value given by the spectroscopic redshift. For comparison, we also calculate Δz_{PZ} for the purely photometric redshifts. The median Δz_{SPZ} and Δz_{PZ} for each field is given in Table 5, as well as the outlier rates,

defined as the fraction of objects for which $|(z - z_{spec})/(1 + z_{spec})| > 0.1$. We observe an improvement in Δz_{SPZ} over Δz_{PZ} from 0.03 to 0.02 in three of the four fields (see Table 5), and an improvement in the outlier rate in all four.

The distribution of redshift accuracy for the entire sample is illustrated in Figures 7 and 8, where the accuracy of a given object's redshift is measured by:

$$\log\left(\Delta z_{SPZ}\right) = \log\left(\frac{|z_{SPZ} - z_{spec}|}{1 + z_{spec}}\right) \tag{2.3}$$

such that more negative results represent redshift fits closer to the spectroscopic redshift. We calculated these for the spectroscopically matched SPZ and photo-z sets, and plotted a histogram of the results in Figure 7. Values of $\log\log(\Delta z_{SPZ}) \leq -2.4$ (which implies $|z_{SPZ} - z_{spec}| \leq 0.004 \cdot (1 + z_{spec})$) were binned together, leading to the larger number of objects seen in the highest-accuracy bin. For the whole sample, the SPZs increase the population of this most-accurate bin by 52% over photometric redshifts. For F105W < 24 mag, SPZs increase it by 69%. Figure 8, which plots Δz_{SPZ} versus Δz_{PZ}, provides an alternative comparison of the results, which calls attention to the number of objects that SPZs rescue from catastrophic failure.

The median redshift difference for SPZs is 0.023, and 0.029 for photo-zs. Use of the SPZ method increases the number of objects in the most accurate bin by $\sim 67\%$. Furthermore, one can see that the SPZ method reduces the incidence of catastrophic failure, by reducing the total number of objects for which $\log(\Delta z_{SPZ}) > -1$ from 8% to 7% across all four fields. For the subset of objects where F105W < 24 mag, the median redshift difference for SPZs is 0.021, and is 0.027 for photo-zs.

Figure 9 shows Δz_{SPZ} versus the spectroscopic redshift. The blue shaded region in each plot corresponds to the redshift range in which the 4000 Å break falls within

the grism coverage ($z = 1.025 - 1.875$). The improvement in accuracy of SPZs over photometric redshifts in this range is comparable to that of the overall sample, and is larger only in GN2. This could indicate that the addition of grism data can be useful in constraining the SED fit even without the 4000 Å break falling in its range, either by identifying features at other redshifts (eg, emission lines) or by conclusively ruling out the presence of a 4000 Å break where broadband data could not. This may also be explained by the blue-region objects being fainter: Figure 10 shows that the majority of catastrophic failures occur beyond F105W > 24 mag. There are also considerably fewer objects in this range with high-accuracy spectroscopic redshifts compared to lower redshifts. These figures also seem to show a slight systematic offset in $(z - z_{spec})/(1 + z_{spec})$: the median $(z - z_{spec})/(1 + z_{spec}) \sim -0.01$ in both SPZs and photo-zs, suggesting a tendency to slightly underestimate the redshift.This could perhaps be explained by the misidentification of the Balmer break (3646 Å) as the 4000 Å break, or the application of the magnitude prior to the redshift calculation could be causing a slight preference for lower redshifts. The results given in Table 5 reflect the median error without correcting for this bias.

2.6 Finding Galaxy Overdensities

After confirming the accuracy of the SPZ set, we performed a pilot study by analyzing the FIGS fields for evidence of significant overdensities in LSS. We began by constructing one-dimensional redshift distributions for each field (Figure 11). This preliminary analysis shows some possible redshift peaks, including one at $z \simeq 0.85$ in GN1. The peak is a bit more dominant in the photometric redshift set at a somewhat higher redshift, but still

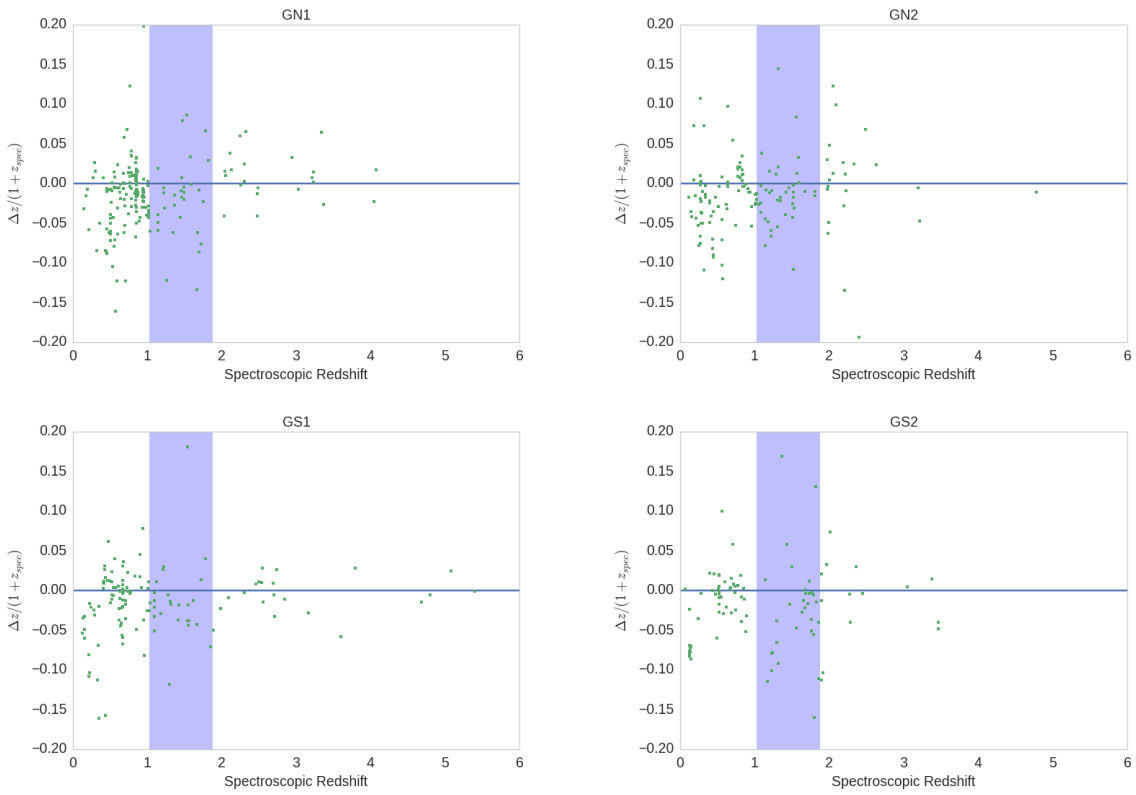

Figure 9: The SPZ $\Delta z_{SPZ} = (z_{SPZ} - z_{spec})/(1 + z_{spec})$ versus the known spectroscopic redshifts for each field, clockwise from top left GN1, GN2, GS2, GS1. The blue shaded region reflects the redshift range in which the 4000 Å break falls within the grism wavelength coverage.

noticeable in the SPZ. Furthermore, given the lower accuracy and higher outlier rate among photo-zs, peaks in the distribution are more likely to be spurious.

2.6.1 Confirmation of a Previously Known Overdensity at $z = 0.85$

To see if there was a matching angular overdensity, we plotted the J2000.0 (RA, DEC) positions of the objects in this peak redshift bin in a two-dimensional histogram (Figure 12, left). This shows several points with a high concentration of objects, the peak of which has a number of sources ~ 4 times the mean in GN1.

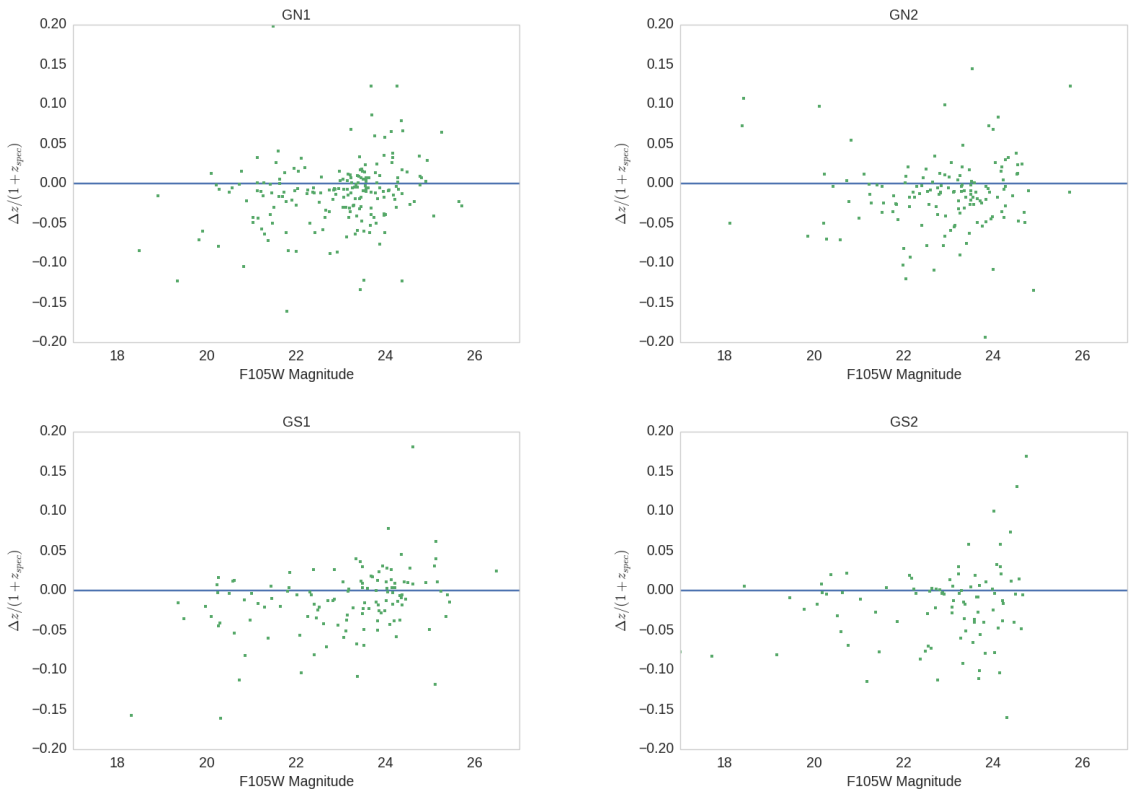

Figure 10: The $\Delta z_{SPZ} = (z_{SPZ} - z_{spec})/(1+z_{spec})$ of SPZ objects versus F105W magnitude for each field, clockwise from top left GN1, GN2, GS2, GS1.

The same process was repeated with the spectroscopic redshift dataset, which shows an overdensity in the same region. To assess this overdensity, we applied a method used for the identification of a candidate cluster in Z-FOURGE (Spitler et al., 2012). We used SPZs to construct a 7th-nearest-neighbor density distribution for the $z = 0.8 - 0.9$ redshift slice in GN1 (Figure 13). This was accomplished by constructing a 500x500 grid of points across the whole GN1 field. For each point, the number density of nearby objects was determined by:

$$n = \frac{N}{\pi r_7^2} \tag{2.4}$$

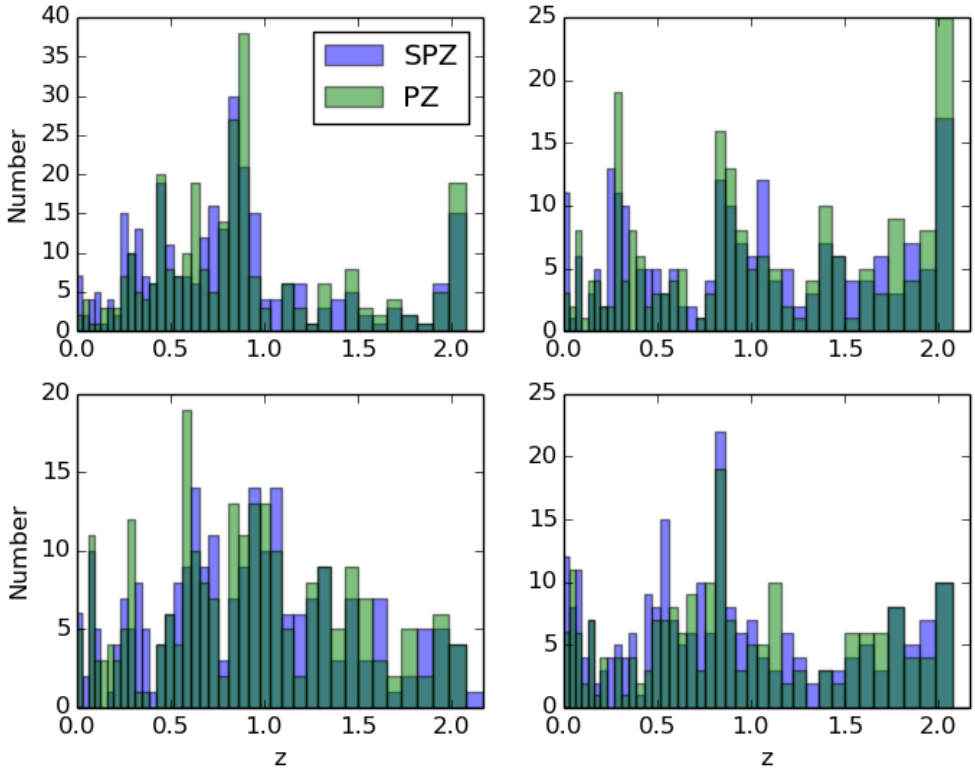

Figure 11: A breakdown of the redshift distributions by FIGS field (clockwise from top left: GN1, GN2, GS2, GS1), using both SPZs (blue) and photo-zs (green). The bin widths are given by $\Delta z = 0.03 \cdot (1 + z)$ in order to roughly match the error threshold of the redshifts. The full photo-z dataset could include many more objects than are presented here; this includes only those with a matching SPZ.

where r_7 is the distance from the point to its seventh-nearest neighbor and $N = 7$ is the number of objects in the redshift slice within the distance r_7. Once this density is calculated for each point in the field, the mean nearest-neighbor density for the slice is determined and used to scale the densities. Spitler and others have tested nearest-neighbor results for values of N ranging from 5-9, and find little change in the significance of cluster detection (Papovich et al., 2010). We performed this analysis for varying values of N as well, and find the same result (see §2.6.2).

The coordinates and redshift of this overdensity correspond to a $z = 0.85$ galaxy cluster

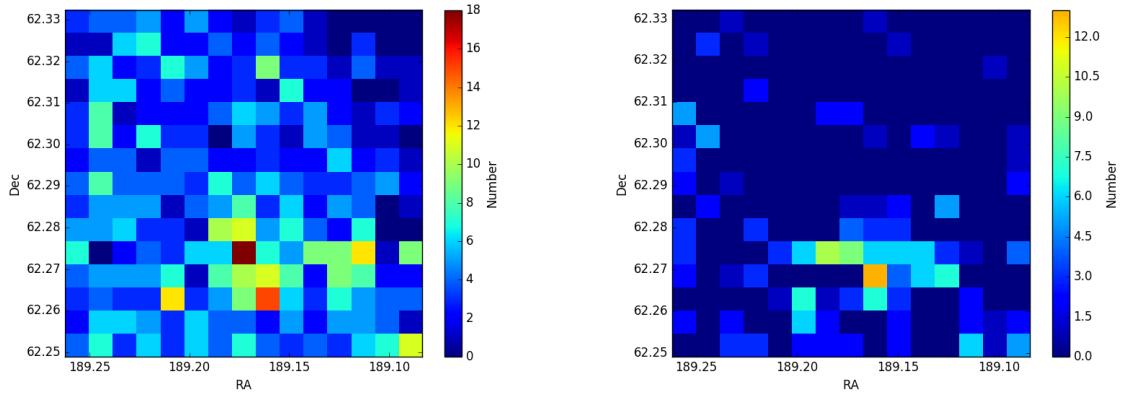

Figure 12: A 2D histogram of redshift $z \sim 0.85$ objects in GN1 from SPZs (left) and spectroscopic redshifts (right). The color of each square bin scales with the number of objects contained in that angular area. Since the objects have already been selected for a narrow redshift range, correlation and overdensity of objects in this plot indicate a spatial correlation. The mean number of objects per bin in GN1 in the SPZ plot is ~ 4.

serendipitously identified with spectroscopic redshifts by Dawson et al. (2001). However, the nearest-neighbor density plot shown in Figure 13 indicates some possible substructures within the overall cluster, which is difficult to identify with the smaller spectroscopic sample alone.

2.6.2 Systematic Search for LSS

Having verified the viability of the method by recovering the $z = 0.85$ cluster, we applied the same nearest neighbor calculation to the rest of the FIGS dataset in slices of $\Delta z = 0.1$. First, we checked the appropriateness of using $N = 7$ for a nearest-neighbor radius r_N by recalculating the density map for the same slice with the value of N varying from 5 to 10. For values $N > 7$, the overdensity is still present, though the significance is diminished with respect to the field background, peaking at 6-7 times the mean density rather than 14.3. For $N < 7$, the significance of the $z = 0.85$ cluster remains at a level comparable to $N = 7$, but other regions in GN1 where there is no spectroscopically confirmed overdensity increased

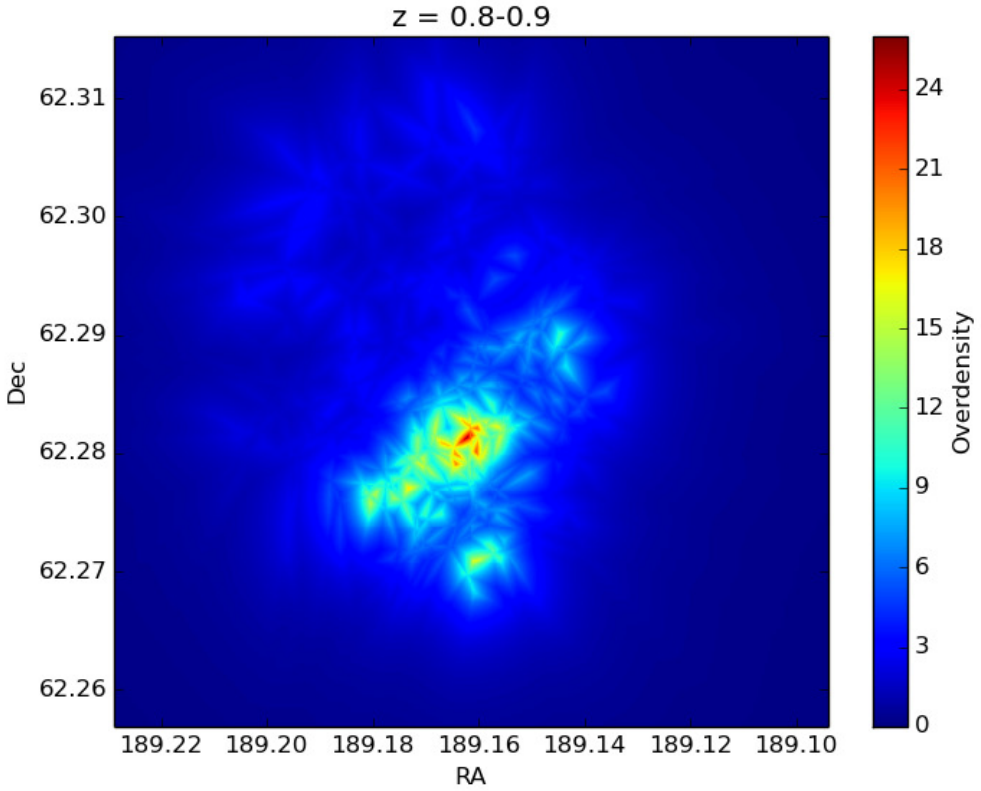

Figure 13: A 7th-nearest-neighbor density map for GN1 in the redshift slice $z = 0.8$ to $z = 0.9$. The color corresponds to the Overdensity factor, which is the density at a given point normalized by the median density of the whole field. The location of the peak overdensity corresponds to a serendipitously spectroscopically identified galaxy cluster at $z = 0.85$.

to a significance unsupported by the spectroscopic coverage. Thus, we settled on $N = 7$, as it demonstrated the best confirmation of the existing overdensity.

We applied the n_7 calculation to each field in slices of $\Delta z = 0.1$ from $z = 0$ to $z = 6$ (the maximum redshift we allowed in the EAZY calculation). If a slice contained too few objects to perform the calculation, it was skipped (as was the case for many of the high-z slices). In order to avoid boundary misses, where an overdensity would be missed if its mean redshift were at the boundary between two Δz steps, we iterated in steps of $0.5 \cdot \Delta z$.

For these slices, we applied two different measures of overdensity significance. First,

we normalized each point in the density grid by the median nearest neighbor density for that redshift slice. This is superior to normalizing by the mean, since the value of the mean will be biased toward a high density peak if one exists. For each slice, we recorded the peak median-normalized density (called $\mathcal{M}$). This checks the significance of an overdense region relative to the density of the entire field at a given redshift range, but may underestimate significance if the angular size of the structure is large relative to the size of the whole field. For the second method, which is based on the method used by Spitler, we calculated the standard deviation in the nearest neighbor density grids of adjacent slices (eg, for the $\Delta z = 0.3-0.4$ slice, we take the average standard deviation of the densities in $\Delta z = 0.2-0.3$ and $\Delta z = 0.4 - 0.5$), and normalized the density grid by this. The peak value was recorded as $\mathcal{S}$. For this method, $\mathcal{S}$ was determined from the nearest redshift slices that did not overlap the Δz of the current slice.

After this broad search, we also conducted a narrower search with $\Delta z = 0.03 \cdot (1 + z_{prev})$ from $z = 0$ to $z = 4$ (at higher redshift there were too few objects per slice). This Δz was selected to match the expected redshift error as determined from our accuracy tests, while also encapsulating the velocity range of a rich cluster, so each redshift slice should contain only objects with the potential to be closely associated.

The overdensity candidates derived from both searches are summarized in Table 6, where we record any redshift slice for which $\mathcal{M} > 10$ and $\mathcal{S} > 10$ via either method, using as a cutoff the lowest-significance detection recorded by Spitler et al. (2012). We consulted the NASA/IPAC Extragalactic Database's list of known clusters to see if the search missed any known clusters. There weren't any listed clusters in the FIGS fields that were missed.

For comparison, we also ran the systematic search using photometric redshifts with $\Delta z = 0.03 \cdot (1 + z_{prev})$ from $z = 0$ to $z = 4$. The results of this comparison are summarized in Table 7. Generally, the photo-z search produced results of lower significance than the

SPZ search. The photo-z search misses the $\mathcal{M}, \mathcal{S} > 10$ cutoff for detection for several overdensities found by the SPZ method, and finds only two that the SPZ method doesn't detect (and one of these is marginal). Furthermore, the photo-z method finds the peak density for GN1-0.8 to be in the 0.870-0.926 redshift bin instead of 0.825-0.880, which we know from spectroscopic redshifts to be correct. This suggests that SPZs are better suited for accurately identifying known overdensities.

2.6.3 A Potential Overdensity at $z = 1.84$

The known $z = 0.85$ cluster in GN1 produced peaks of $\mathcal{M} = 25.16$ and $\mathcal{S} = 25.09$ with the broad search method. We find 4 other slices with a more significant detection in $\mathcal{S}$. Of these, the GS1/HUDF $\Delta z = 1.8 - 1.9$ slice is most significant in $\mathcal{M}$ with $\mathcal{M} = 18.20$. The density map for this slice is shown in Figure 14.

The location of this overdensity matches that of a $z = 1.84$ overdensity identified in Mei et al. (2015) through the visual inspection of G141 spectra and redshifts, and in Kochiashvili et al. (2015) by a search of NIR narrowband-selected emission-line galaxies. Mei et al. identifies 13 candidate members of a $z = 1.84$ protocluster at (53.15565, -27.77930, J2000.0) at a limiting magnitude of F160W < 26 mag, as well as a number of nearby possibly associated galaxy groups at $z = 1.87 - 1.95$. This is very near to the point of peak SPZ density (53.15357, -27.77756, J2000.0) identified via the nearest-neighbor method.

This redshift slice contains 22 objects with SPZs, for 3 of which we have matching spectroscopic redshifts. The characteristics of these objects are summarized in Table 8, where they are grouped by FIGS redshift. Two of the 3 are consistent with $\Delta z = 1.8 - 1.9$, and the third is $z = 2.067$. Furthermore, in the CDFS 7 Ms X-ray source catalogs (Luo et al., 2017), we were able to visually identify a number of close X-ray active sources at this redshift,

Table 6: Potential overdensities identified through the nearest-neighbor method.

ID	RA	Dec	z_1	$\mathcal{M}_1$	$\mathcal{S}_1$	z_2	$\mathcal{M}_2$	$\mathcal{S}_2$	N. Galaxies
GN1-0.2	189.211302	+62.303195	0.2-0.3	11.9	47.1	-	-	-	43
GN1-0.3	189.148053	+62.292436	0.25-0.35	16.5	21.3	0.315-0.354	10.1	10.2	10
GN1-0.4	189.202382	+62.276415	0.4-0.5	10.5	13.7	0.435-0.478	5.9	10.3	26
GN1-0.6	189.141025	+62.290214	-	-	-	0.645-0.694	20.4	16.2	24
GN1-0.7	189.177515	+62.272790	-	-	-	0.735-0.787	17.0	18.1	29
GN1-0.8	189.162108	+62.281327	0.8-0.9	25.2	25.1	0.825-0.880	28.2	24.4	28
GN1-1.2	189.191840	+62.281093	1.25-1.35	15.9	10.3	1.290-1.359	13.3	21.5	7
GN1-1.6	189.149675	+62.287408	1.6-1.7	10.7	21.3	1.680-1.760	7.4	12.9	13
GN1-1.9	189.203733	+62.277585	1.95-2.05	13.0	50.4	1.965-2.054	17.5	15.6	24
GN1-3.2	189.185353	+62.280742	-	-	-	3.21-3.336	27.4	18.4	13
GN2-0.2	189.358060	+62.290507	0.2-0.3	13.8	41.4	0.255-0.293	8.3	64.4	31
GN2-0.5	189.357597	+62.310505	0.5-0.6	10.0	11.6	0.540-0.586	5.8	12.8	16
GN2-0.9	189.376327	+62.290928	-	-	-	0.915-0.972	11.1	15.0	18
GS1-0.1	53.185189	-27.791704	0.1-0.2	10.8	12.9	0.105-0.138	10.7	26.3	15
GS1-0.2	53.166696	-27.787796	0.25-0.35	10.9	27.5	0.270-0.308	12.7	26.2	29
GS1-0.5	53.170932	-27.794401	0.5-0.6	12.3	10.7	-	-	-	23
GS1-0.7	53.161736	-27.789378	-	-	-	0.765-0.818	10.1	15.8	29
GS1-0.9	53.158430	-27.787889	0.9-1.0	11.5	47.8	0.900-0.957	6.0	16.1	48
GS1-1.8	53.153574	-27.777564	1.8-1.9	18.2	41.7	1.815-1.899	20.4	12.8	22
GS2-0.0	53.276137	-27.856452	0.05-0.15	48.9	160.6	0.075-0.107	100.0	378.8	17
GS2-0.1	53.275942	-27.861384	0.1-0.2	15.0	11.4	-	-	-	23
GS2-0.7	53.282187	-27.861471	0.7-0.8	12.1	23.7	0.780-0.833	15.6	32.6	28
GS2-1.6	53.288724	-27.859740	-	-	-	1.665-1.745	16.1	17.2	20
GS2-1.7	53.286967	-27.859913	1.7-1.8	11.9	14.6	1.710-1.807	13.8	13.6	19

The first set of (z, $\mathcal{M}$, $\mathcal{S}$) was derived from the nearest-neighbor search with $\Delta z = 0.1$. The second set was derived with $\Delta z = 0.03 \cdot (1 + z_{prev})$. $\mathcal{M}$ and $\mathcal{S}$ are significance measures detailed in §2.6.2.

Table 7: Overdensity Search Comparison

ID	z_{SPZ}	$\mathcal{M}_{SPZ}$	$\mathcal{S}_{SPZ}$	z_{PZ}	$\mathcal{M}_{PZ}$	$\mathcal{S}_{PZ}$
GN1-0.3	0.315-0.354	10.05	10.18	-	-	-
GN1-0.4	0.435-0.478	5.89	10.30	-	-	-
GN1-0.5	-	-	-	0.510-0.555	10.79	10.56
GN1-0.6	0.645-0.694	20.43	16.15	0.630-0.679	21.75	19.80
GN1-0.7	0.735-0.787	17.01	18.10	0.750-0.803	24.95	12.88
GN1-0.8	0.825-0.880	28.23	24.41	0.870-0.926	15.11	13.18
GN1-1.2	1.290-1.359	13.31	21.49	1.290-1.359	10.56	13.46
GN1-1.6	1.680-1.760	7.40	12.86	-	-	-
GN1-1.9	1.965-2.054	17.51	15.60	-	-	-
GN1-3.2	3.210-3.336	27.43	18.41	-	-	-
GN2-0.2	0.255-0.293	8.29	64.43	0.255-0.293	7.32	27.85
GN2-0.5	0.540-0.586	5.81	12.79	-	-	-
GN2-0.9	0.915-0.972	11.05	15.04	0.930-0.988	7.04	10.81
GS1-0.1	0.105-0.293	10.67	26.33	-	-	-
GS1-0.2	0.270-0.308	12.72	26.22	0.255-0.293	4.71	16.67
GS1-0.5	-	-	-	0.495-0.54	18.65	34.87
GS1-0.7	0.765-0.818	10.07	15.83	0.765-0.818	4.78	10.60
GS1-0.9	0.900-0.957	6.04	16.14	-	-	-
GS1-1.8	1.815-1.899	20.41	12.83	1.83-1.915	5.77	14.05
GS2-0.0	0.075-0.107	100.00	378.80	0.06-0.092	10.49	25.48
GS2-0.7	0.780-0.833	15.59	32.57	0.795-0.849	13.25	11.82
GS2-1.6	1.665-1.745	16.10	17.19	1.68-1.76	21.01	13.81
GS2-1.7	1.710-1.807	13.78	13.60	1.725-1.807	19.90	14.75

$\mathcal{M}$ and $\mathcal{S}$ are significance measures detailed in §2.6.2

most of which are spectroscopically confirmed. The SPZ overdensity, when combined with the Mei et al. overdensity detection and possible presence of X-ray sources, suggests further corroboration of the use of SPZs to identify LSS via this method. Furthermore, it opens up the possibility of using SPZ searches to identify fainter candidate cluster members in already-identified overdensities at comparable redshift (eg, a GOODS-S but non-HUDF cluster identified in Kurk et al. (2009)).

With the narrower search method, the $z = 0.85$ cluster achieves similar significance, with $\mathcal{M} = 28.23$ and $\mathcal{S} = 24.41$. The $z = 1.84$ overdensity in GS1 measures a lower but

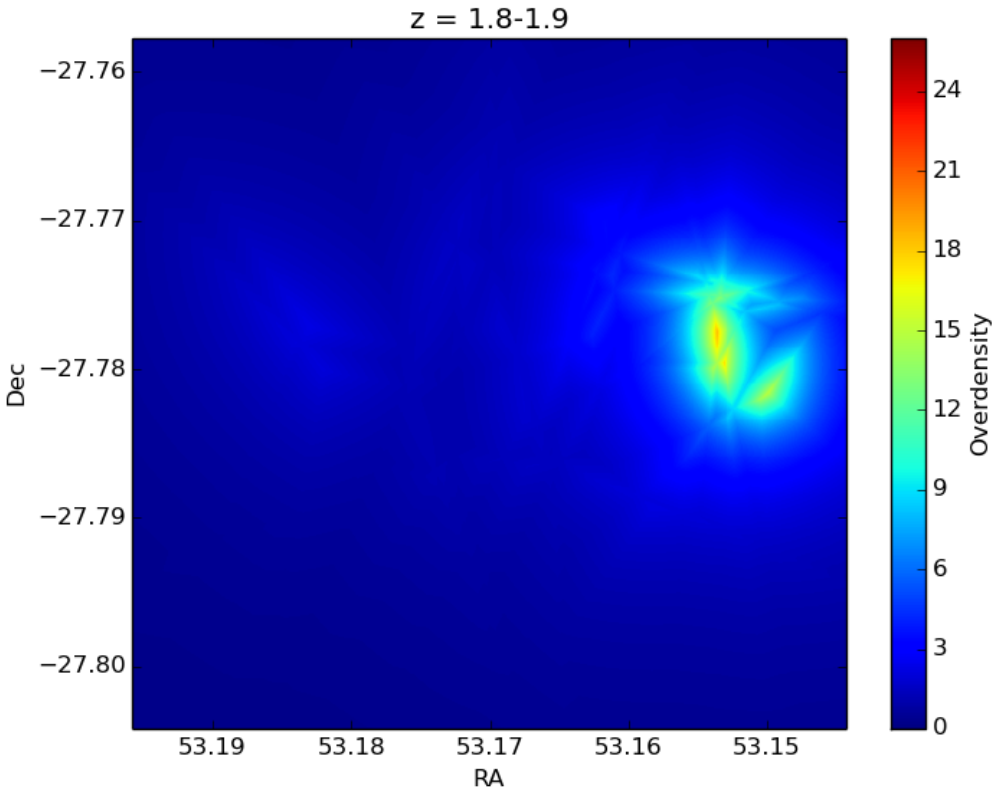

Figure 14: A 7th-nearest-neighbor density map for the GS1/HUDF redshift slice $\Delta z = 1.8 - 1.9$, normalized by the median density.

still significant detection via the $\mathcal{S}$ method, but measures a slightly higher significance via the $\mathcal{M}$ method. There are 4 other detections with a greater significance in at least one metric, including a hugely significant detection in GS2 at $\Delta z = 0.075 - 0.107$ (described in Table 9), and a similar number of detections at comparable significance. The GS2 detection does not appear to match any known overdensity, though it could potentially be associated with nearby diffuse X-rays at $z = 0.126 - 0.128$ (Finoguenov et al., 2015). This is also consistent with the two objects with known spectroscopic redshifts.

2.7 Implications for Future Surveys

The availability of grism spectra for computing SPZs via this method will only increase, as grism surveys will be a key component of future space missions, including the *James Webb Space Telescope* (Gardner et al., 2006; Jansen et al., 2017) and the *Wide Field Infrared Survey Telescope*. For example, NIRISS on *JWST* will provide multi-object slitless spectroscopy at slightly lower resolution but with ~ 5 times the wavelength coverage compared to HST/WFC3. *WFIRST* is anticipated to include a grism mode with $R \sim 550 - 880$ (Spergel et al., 2015) in the near-infrared. The expanded wavelength coverage of NIRISS and the increased resolution of *WFIRST*'s grism will allow surveys with either instrument to obtain redshifts via the method we describe with improved accuracy and outlier rates. This should result in a much larger collection of high-accuracy redshifts than are obtainable with ground-based spectroscopy alone. With FIGS, we produced ~ 1900 redshifts for four 2.05'x2.27' fields, roughly three times the available number of spectroscopic redshifts and complete down to F105W < 26.5 mag. Wide-field slitless spectroscopy with NIRISS will operate with a similar 2.2'x2.2' field of view.

This will have major implications for cosmological studies conducted with the new instruments. The wide field of *WFIRST* and Euclid and the deep reach of *JWST* will enable more thorough LSS studies via cluster identification and weak lensing studies of a vast number of objects. Systematic LSS analyses will require dividing cluster and lensing samples into precise redshift slices, making redshift accuracy a measure of key importance. The application of grism spectra to the redshift measurement via this method can significantly expand the number of objects that are usable for such studies, enabling more and better cluster identifications and improved LSS science. With FIGS, we were able to identify a serendipitously identified and spectroscopically confirmed cluster without reliance on spec-

Table 8: SPZ Objects in $\Delta z = 1.8 - 1.9$

FIGS ID	RA[a]	Dec	z_{SPZ}	z_{spec}	F105W
1482	53.148895	-27.777508	1.815	2.067	24.90
1601	53.157875	-27.779194	1.815	-	26.02
3040	53.162968	-27.800512	1.815	-	25.03
4300	53.15081	-27.769133	1.815	-	25.47
4284	53.184544	-27.768220	1.827	-	25.50
1049	53.172508	-27.771004	1.843	-	25.83
1477	53.158291	-27.777449	1.843	-	24.49
1623	53.154522	-27.779718	1.843	1.837	24.03
1664	53.15287	-27.780123	1.843	-	24.80
1781	53.149021	-27.781952	1.843	-	24.13
1061	53.15604	-27.770947	1.871	-	25.13
1524	53.148975	-27.778151	1.871	-	26.05
2091	53.192116	-27.785559	1.871	-	26.37
4197	53.187511	-27.76623	1.871	-	26.59
4258	53.152287	-27.770088	1.871	1.852	23.66
4322	53.188129	-27.768982	1.871	-	26.06
1499	53.152458	-27.7777	1.9	-	25.83
1167	53.170788	-27.772615	1.9	-	26.57
1905	53.182251	-27.783314	1.9	-	24.93
2010	53.145897	-27.784681	1.9	-	25.20
2266	53.192822	-27.787857	1.9	-	27.35
4177	53.186508	-27.768625	1.9	-	27.38

[a] Using J2000.0 coordinates.

troscopic redshifts, which could provide a few advantages for LSS searches, as demonstrated via our systematic overdensity search. Furthermore, the accuracy of SPZs may allow for the identification of high-z overdensities in regions where spectroscopic redshifts are not plentiful. It is also possible that grism-enabled analysis of spectroscopically confirmed clusters can provide additional information about substructure within overdensities.

Table 9: SPZ Objects in $\Delta z = 0.075 - 0.107$

FIGS ID	RA[a]	Dec	z_{SPZ}	z_{spec}	F105W
1052	53.275558	-27.859404	0.083	-	24.78
1164	53.278240	-27.853859	0.083	-	24.20
1463	53.263836	-27.866632	0.083	-	24.86
1491	53.280373	-27.867067	0.083	-	25.28
3121	53.285057	-27.841299	0.083	-	26.41
3303	53.284992	-27.849686	0.083	-	24.16
3318	53.274483	-27.850365	0.083	-	22.24
1042	53.276077	-27.859423	0.094	-	22.10
1053	53.275337	-27.859568	0.094	-	23.28
1098	53.278564	-27.860065	0.105	-	26.48
1139	53.278801	-27.860723	0.105	-	26.33
1156	53.278751	-27.860992	0.105	-	26.19
1204	53.272770	-27.861732	0.105	-	25.16
1316	53.286377	-27.864700	0.105	0.1337	22.62
1364	53.258823	-27.864935	0.105	0.1275	22.48
3439	53.277348	-27.861378	0.105	-	25.99

[a] Using J2000.0 coordinates.

2.8 Conclusions

FIGS is a WFC3-G102 grism survey from which we obtained ~ 6000 galaxy spectra, which we have combined with broadband photometry in order to produce more accurate spectrophotometric redshifts (called SPZs). Across all four fields and all magnitudes, we achieve a median $\Delta z/(1 + z_{spec})$ of 0.02 for SPZs, as compared to 0.03 for pure photometric redshifts, uncorrected for the slight systematic bias described in §2.5. The SPZs also featured a lower rate of catastrophic failure in redshift fits (8% to 7% overall). SPZs provide an accurate redshift measurement for a larger number of objects per field than can be achieved with ground-based spectroscopy. As grism surveys become more common in upcoming missions, this will allow for the calculation of more comprehensive catalogs of high-accuracy redshifts.

Analysis of the redshift distributions in the SPZs enabled us to independently identify a previously spectroscopically confirmed galaxy cluster at $z = 0.85$, and to identify a known overdensity at $z = 1.84$ using the nearest-neighbor density method. Applying this method systematically across redshift slices in the FIGS fields, we were also able to detect a potentially new overdensity at $z \sim 0.1$, and four other candidate overdensities with a significance comparable to that of the $z = 0.85$ cluster in at least one measure. Given the higher accuracy of SPZs compared to photometric redshifts, this suggests an alternative to detect large scale structure in regions where spectroscopic redshifts are rare. SPZs can also provide the identification of additional cluster member galaxies, which may make it possible to better analyze substructure within a cluster.

Chapter 3

EMISSION LINE METALLICITIES

3.1 Abstract[2]

We derive direct measurement gas-phase metallicities of $7.4 < 12+\log(O/H) < 8.4$ for 14 low-mass Emission Line Galaxies (ELGs) at $0.3 < z < 0.8$ identified in the Faint Infrared Grism Survey (FIGS). We use deep slitless G102 grism spectroscopy of the Hubble Ultra Deep Field (HUDF), dispersing light from all objects in the field at wavelengths between 0.85 and 1.15 microns. We run an automatic search routine on these spectra to robustly identify 71 emission line sources, using archival data from VLT/MUSE to measure additional lines and confirm redshifts. We identify 14 objects with $0.3 < z < 0.8$ with measurable [OIII]λ4363 Å emission lines in matching VLT/MUSE spectra. For these galaxies, we derive direct electron-temperature gas-phase metallicities with a range of $7.4 < 12 + \log(O/H) < 8.4$. With matching stellar masses in the range of $10^{7.9} M_{\odot} < M_{\star} < 10^{10.4} M_{\odot}$, we construct a mass-metallicity (MZ) relation and find that the relation is offset to lower metallicities compared to metallicities derived from alternative methods (e.g.,R_{23}, O3N2, N2O2) and continuum selected samples. Using star formation rates (SFR) derived from the $H\alpha$ emission line, we calculate our galaxies' position on the Fundamental Metallicity Relation (FMR), where we also find an offset toward lower metallicities. This demonstrates that this emission-line-selected sample probes objects of low stellar masses but even lower metallicities than many comparable surveys. We detect a trend suggesting galaxies with higher Specific Star Formation (SSFR) are more likely to have lower metallicity. This could be due to cold

[2]This chapter previously published as Pharo et al. (2019)

accretion of metal-poor gas that drives star formation, or could be because outflows of metal-rich stellar winds and SNe ejecta are more common in galaxies with higher SSFR.

3.2 Introduction

The identification and study of nebular emission lines in galaxies can provide insight into star formation rates, ionization parameters, and gas-phase metallicities, among other physical parameters. The gas-phase metallicity can be related to star formation and mass growth in galaxies via the mass-metallicity (MZ) relation, an observed correlation between a galaxy's stellar mass and its gas-phase metallicity, and by the Fundamental Metallicity Relation (Mannucci et al., 2010; Lara-López et al., 2010), an empirical plane relating the metallicity and the stellar mass to the star formation rate.

These relations have been well-established for local star-forming galaxies (Tremonti et al., 2004), which show an increase in gas-phase metallicity as stellar mass increases from $10^{8.5} M_{\odot}$ to $10^{10.5} M_{\odot}$, after which the metallicity flattens. Further surveys have pushed the study of the relation out to higher redshifts, typically finding lower levels of metallicity out to $z \sim 3$ (Lilly et al., 2003; Maier et al., 2005; Erb et al., 2006; Mannucci et al., 2009). For these studies, the gas-phase metallicity is often measured through empirical and theoretical strong line ratio calibrations, such as R_{23} (Kobulnicky & Kewley, 2004), N2O2 (Kewley & Dopita, 2002), and O3N2 (Pettini & Pagel, 2004), using [OIII], [OII], and Balmer-series hydrogen lines (see Table 10 for description of ratios), or via modeling UV indicators including CIII]1907 (Amorín et al., 2017). However, offsets between local and high-redshift galaxies on diagnostic plots such as the Baldwin-Phillips-Terlevich (BPT) diagram (Baldwin et al., 1981; Steidel et al., 2014; Sanders et al., 2015), which compares the [OIII]λ5007/Hβ line ratio to the [NII]λ6568/Hα line ratio, indicate that conditions in the interstellar medium

may differ at different redshifts (Kewley et al., 2013). If so, there may be undetected biases in the line ratio calibrations. Some studies have also indicated, however, that the presence of very strong emission lines is itself an indicator of low gas-phase metallicity, regardless of the redshift (Finkelstein et al., 2011; Xia et al., 2012; Yang et al., 2017). Given these uncertainties and outliers, it is necessary to seek out samples of ELGs for which we can precisely determine the metallicity, and thus better understand its relationship to the other emission properties of galaxies.

A more direct method for measuring the gas-phase metallicity involves the ratio of the auroral [OIII]λ4363 Å emission line to the [OIII]λ4959,5007 Å lines, which is sensitive to the electron temperature of the ionized gas (Izotov et al., 2006; Aller, 1984; Dopita & Evans, 1986; Kewley & Dopita, 2002). A direct measurement of the electron temperature allows for the derivation of abundances with a minimum of other assumptions compared to the more common strong-emission-line diagnostics using the ratios described above. For example, the R_{23} relation is double-branched, with each R_{23} value corresponding to both a high-metallicity and a low-metallicity solution, requiring additional data or assumptions to break the degeneracy. Consequently, direct-temperature-derived metallicities are more reliable (Izotov et al., 2006). This method is not always practical, as the auroral line is typically quite weak (50-100 times weaker than typical strong lines, per Sanders et al. (2017)) and may require stacking spectra to get a reliable signal (Andrews & Martini, 2013), but it provides more accurate metallicity measurements.

In this paper, we describe our systematic search for Emission Line Galaxies (ELGs) in 1D spectra from the Faint Infrared Grism Survey (FIGS). In §3.3, we describe the survey and procedures for data collection and reduction. In §3.4, we describe the line search method and the flux measurements for confirmed ELGs. In §3.5, we detail the measurement of the gas-phase metallicity, and in §3.6, we explore the mass-metallicity relation and other properties

Table 10: Common Strong Line Ratios

Name	Ratio
N2	log([NII]λ6584/Hα)
O2	log([OII]λ3727+3729/Hβ)
O3	log([OIII]λ4959+5007/Hβ)
R_{23}	log(([OIII]λ4959+5007 + [OII]λ3727+3729)/Hβ)
N2O2	N2 - O2
O3N2	O3 - N2

available from our line measurements. Finally, we summarize in §3.7. For this paper we will use H_0 = 67.3 km s^{-1} Mpc^{-1} and $\Omega_M = 0.315$, $\Omega_\Lambda = 0.685$ (Planck Collaboration et al., 2014). All magnitudes are given in the AB system (Oke & Gunn, 1983).

3.3 Survey Description and Data

3.3.1 FIGS Observations and Spectral Extraction

3.3.1.1 Survey Description

The Faint Infrared Grism Survey (FIGS, HST/Cycle 22, ID:13779, PI S. Malhotra) used the HST WFC3-G102 (see Figure 15) infrared grism to obtain deep slitless spectroscopy of $\sim$ 6000 galaxies. FIGS achieved 40-orbit depth in 4 fields, designated GN1, GN2, GS1 (UDF), and GS2 (HDF-PAR2) (see Table 11 for coordinates of each field). Objects in each field were observed in 5 different 8-orbit position angles (PAs) in order to mitigate contamination of the spectra by overlapping spectra from nearby objects. Each PA covers a 2.05'x2.27'

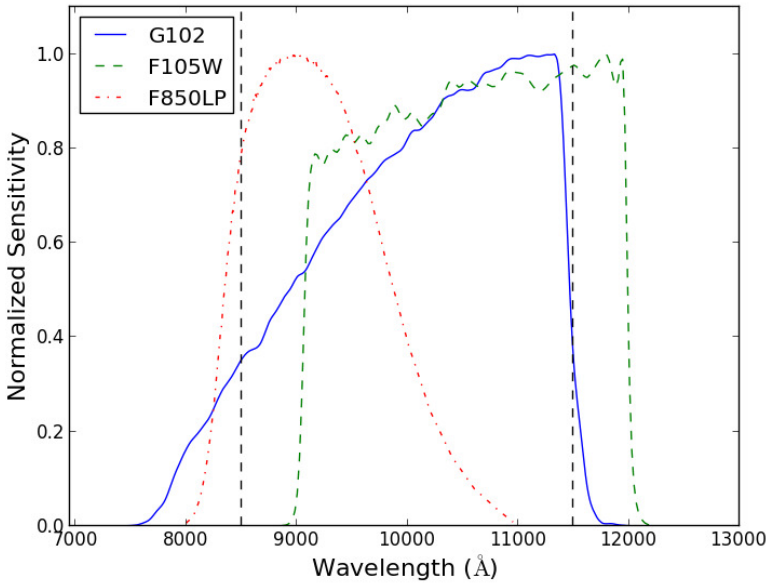

Figure 15: The sensitivity curves for the WFC3/G102 grism, as seen in Kuntschner et al. (2011), and the WFC3-F105W and ACS-F850LP filters. The dashed vertical lines show the cutoffs for grism data used in the emission line search. The curves have been normalized to their maximum sensitivity, so this plot gives the sensitivity at each wavelength in terms of its percentage of the peak sensitivity.

Table 11: A description of the four FIGS fields.

Field	RA	Dec	Area[a]
GN1	12:36:41.467	+62:17:26.27	4.51
GN2	12:37:31.023	+62:18:26.91	5.06
GS1[b]	03:32:40.951	–27:46:47.92	4.09
GS2[c]	03:33:06.468	–27:51:21.56	4.02

[a] Measured in arcmin^2.
[b] The HUDF.
[c] The HDF Parallel Field.

field of view. The area of coverage in each field from which we derive the usable spectra is given in Table 11, for a total area of 17.7 square arcminutes.

3.3.1.2 Spectral Extraction

In this paper, we used 1D spectra which were generated using the methods described

in Pirzkal et al. (2017). Here we briefly summarize this process. FIGS data were reduced in a manner that loosely follows the method used for GRAPES and PEARS, previous HST grism surveys (Pirzkal et al., 2004; Xu et al., 2007; Rhoads et al., 2009; Straughn et al., 2009; Xia et al., 2012; Pirzkal et al., 2013). First, we generated a master catalog of sources from deep CANDELS survey mosaics in the F850LP filter in ACS and the F125W and F160W filters in WFC3 (approximately the z, J, and H bands) (Grogin et al., 2011; Koekemoer et al., 2011). The data were astrometrically corrected to match the absolute astrometry of the GOODS catalogs. The background levels of the grism observations were estimated using a two-components model which include a constant Zodiacal light background as well as a varying HeI light background. Individual spectra were generated using a Simulation Based Extraction (SBE) approach that accounts for spectral contamination from overlapping spectra, as well as allow the use of an optimal extraction approach (Horne, 1986) when generating 1D spectra from 2D spectra. The reader is referred to Pirzkal et al. (2017) for a complete description of these processes. When the extractions were complete, we had an average of ~ 1700 spectra per field, with a typical 3σ detection limit of $m_{F105W} = 26$ mag and an emission line sensitivity of 10^{-17} ergs cm^{-2} s^{-1}.

3.3.2 Optical Data

We supplemented our infrared FIGS spectra with archival high-resolution optical IFU spectra taken with the Multi-Unit Spectroscopic Explorer (MUSE) instrument (Bacon et al., 2010) from the Very Large Telescope (VLT). This expands the available spectroscopic wavelength coverage considerably, enabling confirmation of detected emission lines in FIGS via the identification of complementary emission lines at optical wavelengths. These lines also make possible the mass-metallicity results shown in §5. We used the publicly

available IFU spectra from the MUSE Hubble Ultra Deep Survey (Bacon et al., 2017), a mosaic of nine 1×1 arcmin^2 MUSE fields in the HUDF. In order to extract spectra for emission-line objects in our sample, we applied the following procedure: Using the known sky coordinates for each object, 1D spectrum was generated by summing up flux within a 2 arcsecond aperture (centered on the object) at each wavelength slice, across the entire MUSE wavelength range. We extracted FIGS candidate spectra from the reduced MUSE datacube. The MUSE data wavelength coverage extends from 4752 Å to 9347 Å with a spectral resolution of 2.3 Å, though the sensitivity drops off precipitously at wavelengths lower than 5000 Å and higher than 9200 Å, so we restrict our usage to between these wavelengths. MUSE has a 3σ line sensitivity of $\sim 3 \cdot 10^{-19}$ ergs cm^{-2} s^{-1}, and thus is deep enough to detect the weak [OIII]4363 line for FIGS-selected ELGs.

3.4 Line Identification and Flux Measurement Methods

3.4.1 Line Identification

Because we obtained our infrared spectra via slitless grism spectroscopy, there is no pre-selection of ELG candidates via the placement of slits or by broadband magnitude cutoffs. This has the advantage of enabling the detection of ELGs with potentially very low continuum levels, and so might allow for the study of smaller and/or fainter galaxies with nebular line emission. However, this does require an efficient method for selecting ELG candidates from the total sample of FIGS objects. In order to search the ~ 6000 FIGS spectra for emission lines, we developed a code to automatically search for and identify peaks in a 1D spectrum.

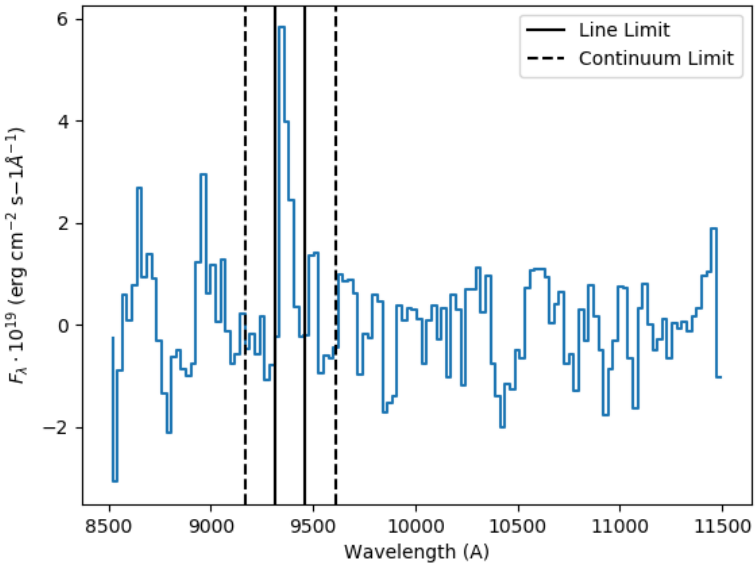

Figure 16: An example of the line-finding routine. This plot shows the continuum-subtracted flux for one PA of FIGS object GS1-2375. This shows an iteration of the line-finding routine when centered at 9388 Å. The routine sums the flux of the pixels within the solid black lines, which is considered to be the candidate line flux. Then, the continuum flux is estimated from the median flux of the pixels between the solid and dashed lines. This continuum is subtracted from the line flux, and the S/N is calculated.

First, the continuum flux needs to be estimated at each wavelength element. The G102 grism measures the spectrum every 24.5 Å, and we use the spectrum from 8500 Å to 11500 Å. The algorithm iterates over each wavelength element in a given spectrum, estimating the continuum flux at that wavelength and subtracting it. This estimation is accomplished via a median-flux filter, where, given a number of wavelength elements for the width of a prospective line, the algorithm measures the flux in a number of elements outside the guessed line width in both the blue and red wavelength directions. The median flux of all of these points is assumed to represent the continuum there, and is subtracted from that point's flux. This serves to estimate the local value of the continuum while avoiding the influence

of the line flux itself or of other features or changes in the spectrum. See Figure 16 for an example continuum-subtracted spectrum.

Next, the signal-to-noise ratio (S/N) is calculated at each wavelength with the residual flux and the flux error (determined by the standard deviation in the fluxes selected for measuring the continuum), once more iterating through the list of wavelength elements. The signal is determined by a sum of the fluxes across 5 points centered on the wavelength of the current iteration, and the noise is the same but added in quadrature. Then the maximum S/N is identified; if the ratio exceeds 5, we fit a Gaussian at the central wavelength element, integrate it to get the flux, and subtract the Gaussian from the residual flux. Then we check the next-highest S/N, and if it still exceeds 5, the routine repeats until the peak S/N is below the detection threshold.

We run this routine on the individual PA spectra in each field, and record all instances of $S/N > 5$. If the code finds a peak in at least two PAs with centroids at the same or adjacent wavelength elements (24.5 Å in either direction), it declares a detection. In this paper, we focus on only one of the fields, GS1/HUDF, and specifically on candidates with optical data available for line confirmation. A broader catalog of 1D-selected ELGs from FIGS will be explored in the following chapter. A search for ELGs in the FIGS 2D spectra can be found in Pirzkal et al. (2018).

In the GS1/HUDF field, where we have matching optical MUSE spectra, this method produces 137 candidate emission line objects. Of these, 131 had matches in the MUSE source catalog within 1 arcsecond of separation. Using our FIGS redshift catalogs (Pharo et al., 2018), we matched the candidate list with their redshifts and sorted the candidates according to the likely spectral emission line at that redshift. We use the wavelength of the peak S/N pixel to get an approximate rest-frame line centroid. We also compared our

candidates with emission lines identified in the GRAPES Survey with the HST ACS G800L grism (Xu et al., 2007).

When identifying the FIGS-spectra emission lines, we considered common strong lines: Lyα, Hα, Hβ, [MgII]λ2798 Å, [OIII]λ5007 Å, and [OII]λ3727 Å, though fainter lines could often be seen in the higher-resolution MUSE spectra. We identified the FIGS lines by determining the ratio of observed wavelengths between two detected emission lines, a fixed property for a given pair of emission lines that is not dependent on the redshift. If no other emission line was detected, we identified the line with the object's photometric redshift. This produced 32 [OIII]λ5007 Å candidates ($z \simeq 0.82 - 1.35$), 22 Hα candidates ($z \simeq 0.30 - 0.80$), and 17 [OII]λ3727 Å candidates ($z \simeq 1.30 - 2.0$). The remaining detections were ruled out if visual inspection found contamination or some other false detection (eg, due to a sharp change in continuum slope), if other line detections in MUSE ruled out a possible line, or if the galaxy had bad redshift calculations. These tended to be among the faintest objects, which are more susceptible to contamination from nearby objects. In order to cast a wide net for ELGs, we did not impose a continuum magnitude limit on the search, relying on visual inspection and other spectra to confirm our detections.

Of the 32 [OIII] candidates from FIGS, 11 were confirmed by inspecting matching MUSE spectra, which means we either measured the same line in the region of overlapping wavelength coverage (8500 - 9300 Å), or measured a second line which produced a wavelength ratio consistent with an [OIII]$\lambda\lambda$4959+5007-[OII]$\lambda\lambda$3727+3729 pair. However, due to the presence of atmospheric emission lines in MUSE and the fact that we cannot know [OII] strength just from [OIII] detection, lack of a clear [OII] detection does not rule out the line being [OIII]. Matches with the GRAPES line list confirmed an additional 7 candidates, leaving 13 unconfirmed (though the line ID is still implied by the redshift) and 1 confirmed to be Hα.

Table 12: The GS1/HUDF emission line candidates by identification

ID	Initial	MUSE	GRAPES	Photo-z	Wrong	Total
[OIII]	32	11	7	13	1[a]	31
Hα	22	15	3	5	0	23
[OII]	17	4	1	12	0	17

[a] Later confirmed to be $H\alpha$.

We used a similar process for the FIGS Hα candidates, of which 15 were confirmed by MUSE, 3 by GRAPES, and 5 were unconfirmed except by photometric redshift (photo-z). For [OII], MUSE can only reliably provide confirmation if the [OII] line is in the overlap region, or if another feature (eg, 4000 Å break), happens to be visible. Only 4 could be confirmed this way, and 1 more from GRAPES, leaving 12 candidates unconfirmed. See Table 12 for a summary of these results.

3.4.2 Flux Measurement

We calculated the emission line fluxes for all of the emission line candidates, regardless of their confirmation status. Beginning with the brightest FIGS line in the spectrum (Hα, [OIII], or [OII], depending on the candidate line ID), we performed a Gaussian fit using the Kapteyn Package (Terlouw and Vogelaar, 2015) at the wavelength of the peak in each PA where there was a 5σ detection, allowing the Gaussian amplitude and sigma to be free parameters with an initial guess based on the peak flux. The centroid was allowed to vary between the adjacent pixels in order to determine the best-fit line center. We interpolated a Gaussian function from the fit, from which we derived the total line flux. Once all PAs for a single object and line had been fit, we averaged the individual fluxes and propagated the individual errors to get the final line measurement.

Once the primary line fit was completed, we recalculated the redshift based on the line

center and used this new redshift measurement to predict the locations of other lines. The Gaussian function representing the previous fit was subtracted from the flux, and then we attempted to fit the next line. We repeated this process for any common, strong emission lines within the wavelength coverage. In the FIGS spectra, the only non-primary line detected with any significance was Hβ. If an object had matching MUSE spectra, we applied the same process there as well. Total flux errors were estimated based on the propagation of errors in the Gaussian fit parameters, which the Kapteyn fitting package determined in part based on flux errors in the constituent pixels.

For the 18 objects where the Hα emission line was detected in FIGS and for which a matching optical spectrum was available, the extinction was measured via the Balmer decrement. All the galaxies for which we later derive T_e-based metallicities are included in this set. In order to correct for stellar absorption of the Balmer lines, we follow the procedure used in Ly et al. (2014), which covers objects a similar redshift. For objects without measurements in both $H\alpha$ and $H\beta$, we applied an extinction correction using the Calzetti et al. (2000) reddening model, following the procedure used in a study of ELGs with R_{23} at comparable redshift (Xia et al., 2011). The full catalog of flux measurements is listed in Appendix A.

3.4.3 Line Comparisons in FIGS and MUSE

In addition to using emission lines in optical spectra to confirm line detections in FIGS, the measurement of additional line fluxes for an ELG makes it possible to measure gas-phase metallicities, but it is first necessary to check the consistency of the flux measurements between the two sources of spectra. We were able to check this by looking at emission lines that appeared in both the G102 and MUSE spectra. For emission lines observed between

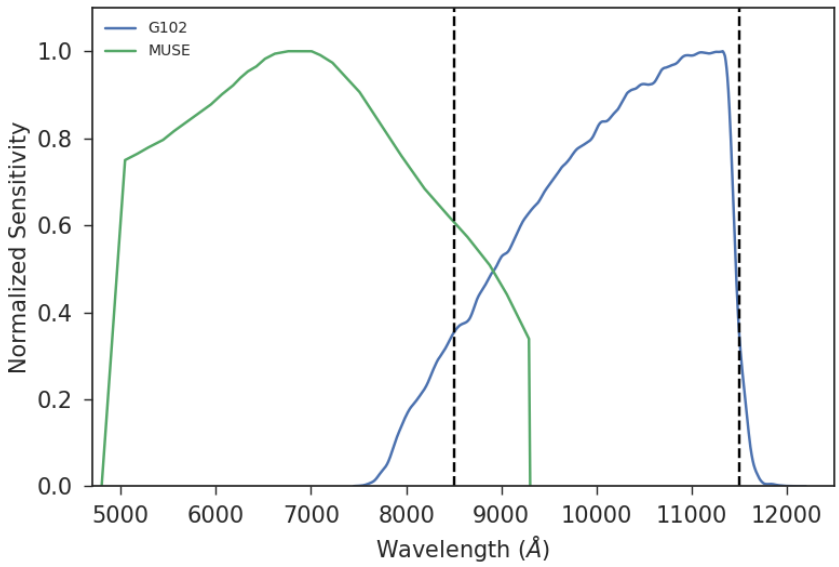

Figure 17: The sensitivity curve for the WFC3/G102 grism (Kuntschner et al., 2011), and for MUSE (Bacon et al., 2010). The dashed vertical lines show the cutoffs for grism data used in the emission line search. The curves have been normalized to their maximum sensitivity.

8500 Å and 9200 Å (See Figure 17), where the throughput of both instruments is good, we were usually able to measure the line flux in both FIGS and MUSE. This provided the opportunity to compare line measurements between the space-based HST/WFC3 and the ground-based VLT/MUSE instruments. In Table 13, we show the flux measurements of the six matching objects, where the [OIII]$\lambda\lambda$5007,4959 were measured. The matching fluxes are within the measured 1σ flux errors for four of the six objects, including the two which are part of the later analysis in this paper. Object 2654 was primarily detected by the Hα line, and one PA of the FIGS spectra contains non-removed contamination at the predicted location of the [OIII] line, which skewed its average flux measurement high. Removing this one PA from the flux measurement brings the FIGS spectra flux into agreement with what we measure in MUSE, bringing the number of well-matched spectra to five of six objects.

Because so few objects have an emission line appear in both spectra, it is difficult to judge whether any systematic offset is present from the few where the flux differs. Examining these

Table 13: FIGS-MUSE Objects

FIGS ID	RA	Dec	λ (Å)	z	FIGS Flux[a]	MUSE Flux [a]
1467	53.151047	-27.777309	8735	0.736	347.7 ± 27.1	365.3 ± 36.2
1689	53.162483	-27.780346	8615	0.719	890.6 ± 39.0	860.9 ± 56.7
1851	53.152782	-27.782698	8855	0.766	967.2 ± 58.4	1007.1 ± 97.3
2560	53.184158	-27.792637	8687	0.738	1821.9 ± 208.1	2041.8 ± 121.9
2654	53.182205	-27.793993	8687	0.735	$315.0^{b} \pm 45.5$	352.1 ± 50.6
8178	53.187664	-27.783779	8663	0.734	176.6 ± 28.7	94.3 ± 34.3

[a] Measured in 10^{-19} erg/cm^2/s.
[b] Flux calculated after removing one PA for uncorrected contamination, which significantly altered the flux average.

cases does, however, suggest some possible causes for difference in FIGS and MUSE flux due to contamination or other artifacts, which we checked for visually in our further results. We examined the individual PAs for the 14 objects used in the mass-metallicity analysis to search for any unnoticed contamination that could affect the FIGS lines as with Object 2654, or for any other issues. We discovered no such contamination in any lines required for the metallicity measurement. Object 1299 possibly suffers from oversubtraction of the Hα line. However, this object is detected in 5 PAs, so the effect is small.

We also compared the redshifts derived individually from the FIGS line detection and the MUSE line. We calculated the redshift of each object in Table 13 based on the best-fit central wavelength of the line fit for each spectrum. The differences are plotted as a function of MUSE redshift in Figure 18. We find a root-mean-square (RMS) redshift difference ($\Delta z/(1+z)$) between the two sources of spectra of $\sigma_z = 0.002$. Xia et al. (2011) found an RMS of $\sigma_z = 0.006$ when comparing redshifts derived from the HST ACS PEARS grism survey and from Magellan's LDSS-3 spectrograph ($R = 100$, as compared to $R = 210$ for G102). This indicates FIGS has a wavelength calibration of at least comparable accuracy to PEARS, given the spectral resolution in each.

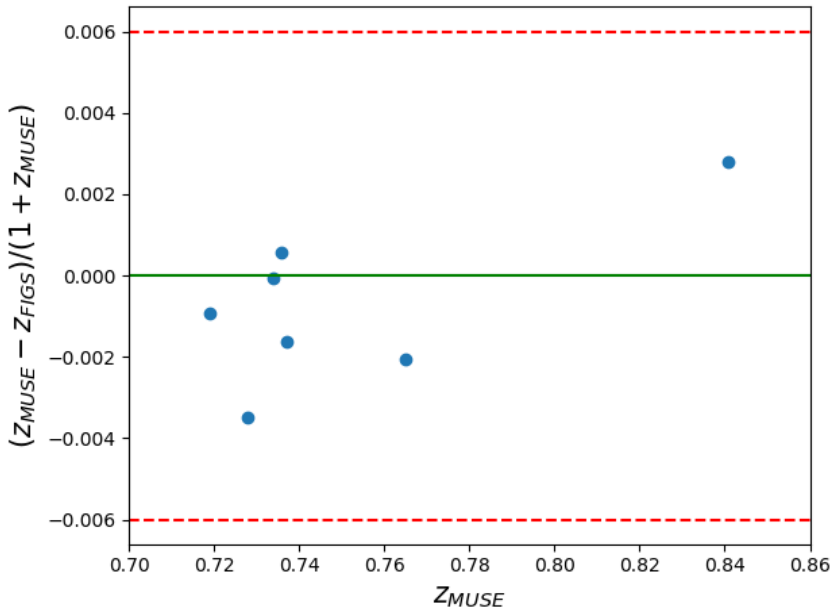

Figure 18: The differences in redshift calculated from the FIGS emission lines and the MUSE emission lines are shown here in blue, with the green line showing a difference of 0. The dashed red lines give the bounds of the RMS wavelength error from (Xia el at. 2011) between the ACS grism and the LDSS3 spectrograph. We measure and RMS redshift difference of $\sigma_z = 0.002$.

3.5 Metallicity Measurements

Strong nebular emission lines provide the means to measure the gas-phase oxygen abundance in a galaxy, which serves as a proxy for the metallicity. For objects with a [OIII]λ4363 Å auroral line detected at $S/N \geq 3$, we used the direct metallicity measurement described in Ly et al. (2014), based on the empirical relations in Izotov et al. (2006). This method first estimates the [OIII]4363 electron temperature (T_e) based on the nebular-to-auroral flux ratio:

$$\log\left(\frac{[OIII]\lambda\lambda 4959, 5007}{[OIII]\lambda 4363}\right) = \frac{1.432}{t_3} + \log C_T \tag{3.1}$$

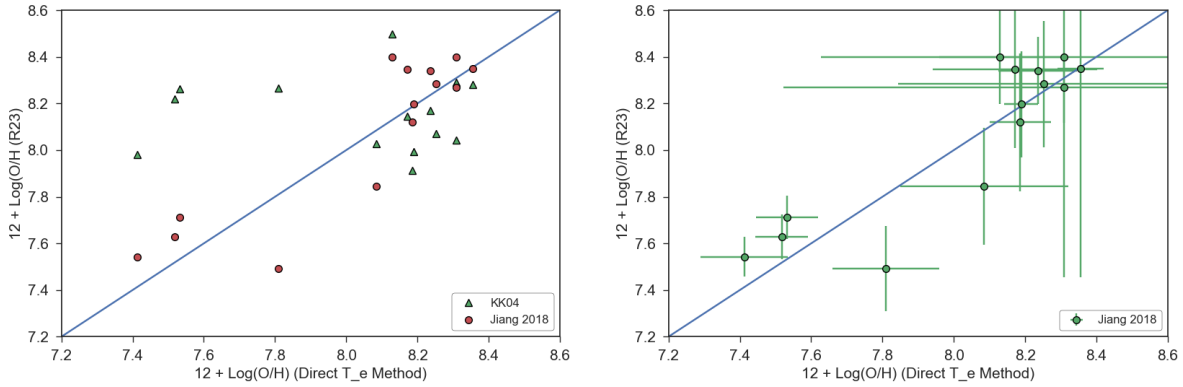

Figure 19: Left: R_{23} metallicities compared with T_e-derived metallicities, using both the KK04 (Kobulnicky & Kewley, 2004) parameterization (green triangles) and new calibration based on Green Peas (Jiang et al. 2018) (red circles). Both R_{23} methods place all of the FIGS objects on the lower branch, but the KK04 parameterization tends to overestimate the lowest-metallicity objects, while the Green Pea calibration reduces the scatter considerably. Right: The comparison of the calibrated R_{23} metallicities with T_e metallicities including errors.

where $t_3 = T_e([OIII])/10^4$ K, and

$$C_T = (8.44 - 1.09t_3 + 0.5t_3^2 - 0.08t_3^3) \cdot \frac{1 + 0.0004x}{1 + 0.044x} \tag{3.2}$$

where $x = 10^{-4} n_e t_3^{-0.5}$, and n_e is the electron density (cm^{-3}). Since we are unable to resolve the $[SII]\lambda\lambda 6717, 6732$ doublet in FIGS, and it is too red to appear in MUSE spectra, we cannot directly measure n_e, but C_T is only strongly dependent on n_e in the high-density regime ($n_e > 10^4$ cm^{-3}), where n_e is large enough for the x term to be important. We tested the temperature calculation with $n_e = 10, 100, 100$ cm^{-3} using a range of measured line ratios from Ly et al. (2014), and the resulting temperatures were virtually identical for the different density measurements. Thus, we can safely adopt the assumption of Ly et al. (2014) that $n_e \approx 100$ cm^{-3} for our calculations.

With the temperature estimated, the ionic abundances of oxygen can be determined from the line ratios $[OII]\lambda\lambda 3726, 3729/H\beta$ and $[OIII]\lambda\lambda 4959, 5007/H\beta$:

$$12 + \log\left(\frac{O^+}{H^+}\right) = \log\left(\frac{[OII]}{H\beta}\right) + 5.961 + \frac{1.676}{t_2} \tag{3.3}$$

$$12 + \log\left(\frac{O^{++}}{H^+}\right) = \log\left(\frac{[OIII]}{H\beta}\right) + 6.200 + \frac{1.251}{t_3} \tag{3.4}$$

where t_2 is the [OII] electron temperature, assuming a two-temperature model $t_2 = T_e([OII])/10^4$ K $= -0.577 + t_3(2.065 - 0.498t_3)$ from Izotov et al. (2006). In nebular regions, oxygen ions in ionization states other than O^+ and O^{++} make up a negligible fraction of the population, so the total oxygen abundance can be determined from

$$\frac{O}{H} = \left(\frac{O^+}{H^+}\right) + \left(\frac{O^{++}}{H^+}\right) \tag{3.5}$$

14 objects have sufficient [OIII]4363 signal ($S/N \geq 3$) in the MUSE optical spectra, as well as the other requisite [OIII], [OII], and Hβ lines, to perform this direct metallicity measurement. Refer to the full line table in Appendix A for the fluxes and origins of individual lines. We summarize metallicity and electron temperature measurements for these objects in Table 14. For one of these objects, FIGS ID 2560, we observed a strong peak at the location of the [OI]λ6300 emission line in one PA, a possible indicator of Seyfert or LINER properties. By consulting line ratio diagnotics in Kewley et al. (2006), our measurements match the characteristics of a Seyfert galaxy, which could explain the very high temperature measurement, and could skew the metallicity calculation if the [OI] line is real.

For ELGs without a significant [OIII]4363 detection, we computed metallicities iteratively using the R_{23} diagnostic (Pagel et al., 1979), given by the ratio $R_{23} = ([OII] + [OIII])/H\beta$. We tested the effectiveness of this method compared to the direct measurement by calculating metallicities using both methods for the 14 objects where this was possible,

and we found some significant disagreement in the results between the two, particularly at low metallicity, as can be seen in Figure 19. This is not unusual: Kewley & Ellison (2008) shows that different metallicity diagnostics can produce different measurements of oxygen abundance with a scatter of up to 0.7 dex. However, Christensen et al. (2012) has demonstrated that using an R_{23} calibration with a correction for the ionization parameter based on the [OIII]/[OII] ratio (Pilyugin & Thuan, 2005) agreed well with direct metallicities of $z \sim 2$ galaxies. To address this, we applied a new empirical R_{23} calibration with an [OIII]/[OII] ratio correction, based on a sample of 800 "green pea" galaxies at $0.011 < z < 0.411$ with reliable direct metallicity measurements (Jiang et al., 2019). This new calibration reduced the scatter between T_e-derived metallicities and R_{23}-derived metallicities, as can be seen in Figure 19, demonstrating that we could obtain reliable metallicity measurements using R_{23}. Thus, we were able to add 8 additional objects to our metallicity sample via the calibrated R_{23} method.

Error measurements for the metallicities are obtained via the propagation of the initial flux errors through the electron temperature calculation combined with error introduced by the extinction correction, and are reported at 1σ. Electron temperature errors are determined by the errors of the line fluxes going into the [OIII] line ratio: [OIII]5007,4959 and [OIII]4363. These are summarized in Table 14.

3.6 Results and Discussion

3.6.1 Mass-Metallicity Relation

We obtained stellar masses from the catalogs in Santini et al. (2015). Santini et al. presented a series of mass catalogs derived from CANDELS photometry (UV to through mid-IR in GOODS-S) and redshifts. The catalogs were computed using a variety of stellar

Table 14: FIGS T_e Metallicities

FIGS ID	12+Log(O/H)	$Log(M_\star)$	$Log(T_e/K)$	SFR($M_\odot$/yr)	z
950	7.81 ± 0.15	8.92	4.46 ± 0.09	0.71 ± 0.18	0.678
1016	8.25 ± 0.23	9.12	4.01 ± 0.10	0.17 ± 0.15	0.622
1103	8.17 ± 0.23	9.80	4.03 ± 0.06	0.59 ± 0.23	0.334
1171	7.52 ± 0.07	8.58	4.35 ± 0.09	0.76 ± 0.13	0.606
1295	8.19 ± 0.05	9.74	4.00 ± 0.08	1.41 ± 0.17	0.420
1299	8.31 ± 0.68	9.87	4.02 ± 0.13	0.59 ± 0.76	0.622
1392	8.19 ± 0.09	9.87	4.01 ± 0.08	3.18 ± 1.27	0.668
1689	7.41 ± 0.12	8.20	4.34 ± 0.08	0.65 ± 0.18	0.719
2168	7.53 ± 0.09	7.99	4.38 ± 0.05	0.12 ± 0.02	0.468
2378	8.09 ± 0.24	10.06	4.08 ± 0.05	2.92 ± 1.20	0.436
2517	8.13 ± 0.17	9.64	4.09 ± 0.07	5.99 ± 2.13	0.459
2560[a]	8.24 ± 0.11	9.88	4.51 ± 0.07	5.61 ± 1.01	0.738
2783	8.31 ± 0.79	7.88	4.03 ± 0.13	0.06 ± 0.13	0.532
4198	8.36 ± 0.06	10.44	4.00 ± 0.14	3.10 ± 0.39	0.669

For object coordinates and line fluxes, see the table in Appendix A. Stellar mass error is ≤ 0.1 dex. See §3.6.1 for discussion.
[a] Object 2560 has possible indicators of being a Seyfert galaxy. See §3.5 for details.

mass codes and a range of preferred modeling parameters. We considered only the mass catalogs whose fits included contributions from nebular emission, which restricted our choice to four of the mass catalogs presented by Santini et al. We use the mass values from one of these, their $6a_\tau NEB$ method, which is fit to BC03 templates (Bruzual & Charlot, 2003) using a Chabrier Initial Mass Function (IMF) and includes the widest range of considered metallicities out of the four methods that consider nebular emission in their SED fits. Santini et al. do not provide individual estimates of the mass error, but they did investigate the distributions of mass estimates as compared to the median masses from the list of mass catalogs. They quantified the typical deviation from the median mass with the distribution's semi interquartile range, which they found to be usually less than 0.1 dex, giving a reasonable upper bound on the mass uncertainty.

We matched the Santini et al. catalog with our 22 objects with T_e or R_{23} metallicity

measurements within an angular separation of 1 arsecond and confirmed that the CANDELS redshifts provided by the Santini catalog matched the line-derived redshifts for the objects. Then we produced a relation between the stellar mass and the gas-phase oxygen abundance for the 14 objects with T_e-derived metallicities, as can be seen in Figure 20. This subsample has a median redshift of $z = 0.614$. We parameterize the FIGS mass-metallicity relation with a quadratic function of the form

$$12 + \log\left(\frac{O}{H}\right) = A + Bx + Cx^2 \tag{3.6}$$

where $x = \log(M_\star/M_\odot) - 10$. We use a Python function, curve-fit from the SciPy package (Jones et al., 2001–), to perform a least squares fit of the FIGS data to this parameterization. The MZ relation is best fitted by

$$12 + \log\left(\frac{O}{H}\right) = 8.240 + 0.367x - 0.018x^2 \tag{3.7}$$

The 1σ errors in the parameters are determined from the diagonal of the covariance matrix, which gives $\sigma_A = 0.033$, $\sigma_B = 0.089$, and $\sigma_C = 0.051$. We estimate the uncertainty in the fit by performing a Monte Carlo simulation at each stellar mass in the range of the fit (1000 points between $\log(M_\star/M_\odot) = 7.70$ and 10.44), assuming a Gaussian distribution around these errors. For each mass point, the fit parameters are sampled 10000 times, and the standard deviation of the result is used to estimate the 1σ uncertainty in the fit. This is represented by the shaded region in Figure 20.

3.6.2 Comparison with Other MZ Relations

Figure 20 shows the FIGS-MUSE mass-metallicity relation for the T_e-measured objects plotted alongside mass-metallicity relations from other surveys at similar redshift. Our

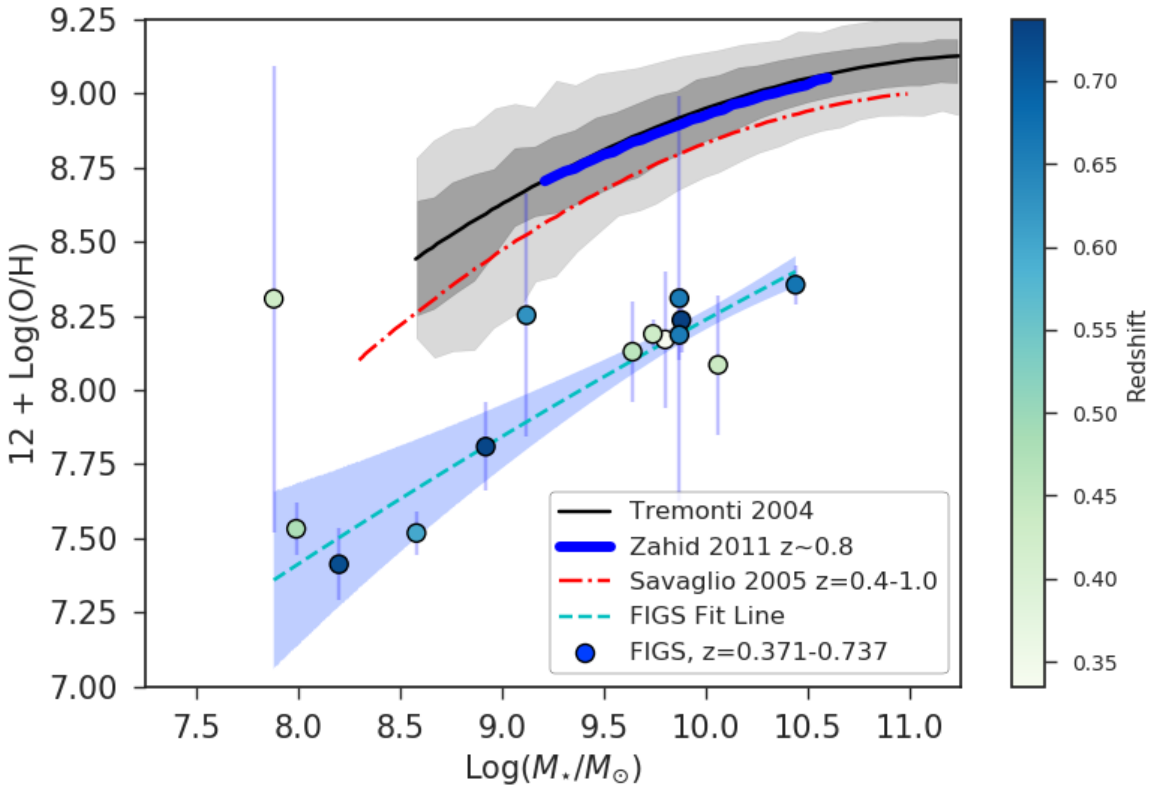

Figure 20: The MZ relation between the stellar masses as measured by Santini et al. (2015) and the gas-phase oxygen abundances for FIGS objects as measured by $[OIII]\lambda 4363$ in matching MUSE spectra. The FIGS objects are given by circles with errorbars in metallicity, and are shaded by redshift, with a median of $z = 0.614$. The black line and contours represent local SDSS galaxies as measured in Tremonti et al. (2004). The thick blue, solid line represents the $z \sim 0.8$ upper-branch R_{23} metallicities from Zahid et al. (2011), and the red, dot-dash line represents the $0.4 < z < 1.0$ upper-branch R_{23} metallicities from Savaglio et al. (2005). The blue dashed line is the non-linear least squares fit to the FIGS objects, using SciPy's curve-fit function (See Equation 3.7 for parameters) (Jones et al., 2001–). The blue shaded region is the 1σ uncertainty of the fit as measured from a Monte Carlo of the 1σ uncertainties in the fit parameters.

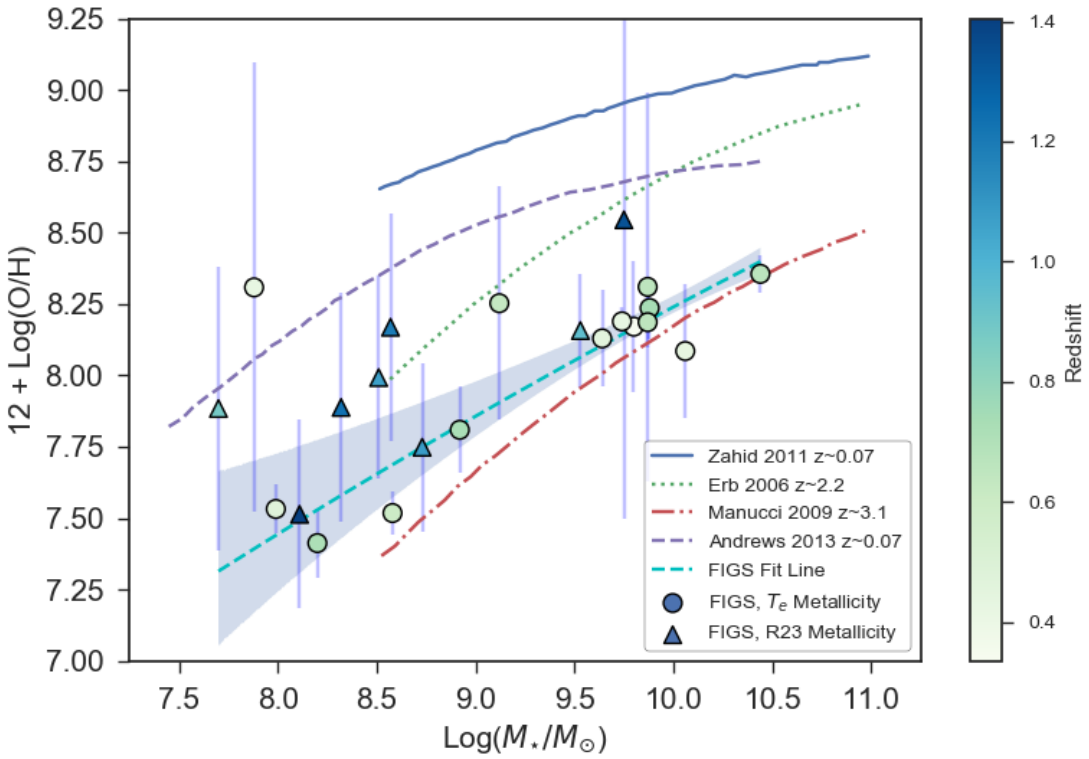

Figure 21: The relation between the stellar masses as measured by Santini et al. (2015) and the gas-phase oxygen abundances as measured by $[OIII]\lambda 4363$. The FIGS objects are given by circles (direct metallicity measurement) and triangles (calibrated R_{23}) with blue errorbars in metallicity, and are shaded by redshift. The blue solid line represents the $z \sim 0.07$ relation for local galaxies described in Zahid et al. (2011); the purple dashed line represents the $z \sim 0.07$ direct-metallicity relation from Andrews & Martini (2013); the green dotted line Erb et al. (2006) and the red dash-dot line Mannucci et al. (2009) represent R_{23}-derived relations at $z = 2.2$ and $z = 3.1$. The blue dashed line is the non-linear least squares fit to the FIGS objects, using SciPy's curve-fit function (See Equation 3.7 for parameters) (Jones et al., 2001–). The blue shaded region is the 1σ uncertainty of the fit as measured from a Monte Carlo of the 1σ uncertainties in the fit parameters.

measurements are offset to lower metallicity by $\sim 0.6 - 0.7$ dex compared to these surveys. The curve from Zahid et al. (2011) is fit from stacks of DEEP2 objects at $z \sim 0.8$, for which metallicities were derived using the R_{23} method. Zahid et al. (2011) notes that since $[NII]/H\alpha$ measurements were not available, they were unable to break the R_{23} degeneracy and instead assume the metallicities lie on the R_{23} upper branch, though they observe that this assumption breaks down at $M_\star < 10^9 M_\odot$. Savaglio et al. (2005) derived an MZ relation for 56 $0.4 < z < 1.0$ galaxies from the Gemini Deep Deep Survey and the Canada-France Redshift Survey, also using the R_{23} upper branch for metallicity. As described in §3.5, when we apply the R_{23} calculation to the 14 FIGS objects, both methods place all of them on the low-Z branch, which is itself enough to alter the metallicity measurement by up to $\sim$1 dex, enough to explain the offset in metallicity between the two surveys.

A more "direct" MZ comparison can be made from the Andrews & Martini (2013) (hereafter AM13) result, shown in Figure 21 as a purple dashed curve. The AM13 MZ relation is derived from stacks of direct-method metallicity calculations of local SDSS galaxies at $z = 0.07$. The direct-metallicity FIGS measurements are denoted by circles and the calibrated-R_{23} measurements denoted by triangles. Despite also using the [OIII]4363 T_e method, AM13 find higher metallicities than we find, with a median metallicity offset of +0.65 dex.

3.6.3 Discussion of the Offset

In this section, we examine possible causes for the low-metallicity offset of our sample.

3.6.3.1 Redshift

In Figures 20 and 21, the FIGS points are colored according to the line-centroid-derived

redshift, but no significant trend in redshift emerges from among these 14 ELGs. This agrees with the results of Savaglio et al. (2005), who also found no significant redshift evolution in metallicity in their sample at a similar redshift range.

The median redshift in the AM13 sample is $z = 0.07$, with a maximum of $z = 0.25$. This is lower than the minimum redshift in the FIGS sample ($z = 0.371$), and the median redshift in the FIGS T_e-derived sample is $z = 0.614$. Previous surveys (Maiolino et al., 2008; Zahid et al., 2013) suggest the metallicity evolution from $z = 0$ to $z \sim 0.8$ is roughly 0.1-0.2 dex at a given stellar mass. This is not large enough to account for the offset between FIGS and AM13, though possibly the R_{23} measurements used by the previous surveys underestimate this evolution. This offset does allow for the FIGS objects to fall within the scatter of the metal-poor galaxies in the AM13 sample.

Jones et al. (2015) selected a sample of 32 DEEP2 galaxies with [OIII]4363 emission at $z \sim 0.8$ from which they calculated gas-phase metallicities in the range $7.8 < 12 + \log(O/H) < 8.4$. They do not include a mass-metallicity relation, but most of the FIGS objects have metallicities that are consistent with this metallicity range to within the 1σ error. Of the three objects with significantly lower measured metallicity, only one is at a redshift at the higher end of the sample redshift ($z = 0.719$), and thus at a comparable redshift to the Jones sample, and all three are at relatively low mass.

3.6.3.2 IMF

Inconsistency in the IMF used to derive stellar masses for different studies can produce offsets in stellar mass, which in turn would affect the MZ Relation. Masses for the Zahid et al. (2011) relation were also calculated using a Chabrier IMF, while the Savaglio et al. (2005) relation uses masses with an IMF derived by Baldry & Glazebrook (2003) that

produces masses 1.2 times smaller than Kroupa. A calculation of IMF offsets (Zahid et al., 2012) suggests an offset of +0.03 dex between Kroupa-derived and Chabrier-derived stellar masses, and an offset of -0.07 dex between Chabrier masses and those used in Savaglio et al. (2005). The Andrews & Martini (2013) relation used masses derived from a Kroupa IMF, which should result in a +0.03 mass offset compared to the Chabrier masses used in the FIGS relation. These offsets are all comparable to the < 0.1 dex scatter in stellar masses in the Sanders et al. (2015) catalogs, and are much too small to explain the metallicity offset.

3.6.3.3 Contributions of Multiple HII Regions

Another explanation for the low metallicities we measure is the possibility that the lines we detect are dominated by emission from particularly extreme regions within the galaxy. An HII region with an especially low metallicity and large electron temperature could produce stronger [OIII]4363 emission for that region. In a small galaxy, the flux from such a region could dominate compared to flux from milder regions, resulting in that region's low metallicity measurement reducing the overall metallicity measurement for the galaxy (Sanders et al., 2017). This could perhaps explain the extremely low metallicities of the lowest-mass objects, but does not account for the lower M-Z relation overall.

3.6.3.4 Selection Effects, Line Emission, and Star Formation

In Figure 21, we have also included the FIGS objects with calibrated R_{23} metallicities (see §3.5), denoted by triangles. There continues to be no significant redshift evolution, as these new, higher-z objects tend to have higher metallicity. This is likely a selection effect: the highest redshift objects are also exclusively R_{23}-calibrated. This means that there

cannot have been a detected [OIII]4363 line, which itself implies possibly lower [OIII]4363 emission, which in turn implies a higher metallicity for the objects in the calibration sample. Furthermore, these objects are typically fainter, resulting in larger flux errors which contribute to broader error bounds on the metallicities. The high-z objects are still consistent with the possible range of the MZ fit, and there are a few objects in the R_{23} sample where we measure low metallicities comparable to what we measure with [OIII]4363. This means that [OIII]4363 selection alone cannot fully account for the metallicity offsets, and so lends support to the findings in Xia et al. (2012), which suggest that emission line strength itself is an indicator of low metallicity.

More recently, Amorín et al. (2017) find a sample of $2.4 < z < 3.5$ galaxies with $7.4 < 12 + \log(O/H) < 7.7$ using strong UV emission lines. They find low metallicities consistently across a broad range of stellar masses, up to $\log(M_\star/M_\odot) = 9.8$. Their sample also shows indicators of recent star formation, suggesting a link between star formation and metallicity somewhat independent of the stellar mass. We explore the effects of star formation for the FIGS objects in the following section.

3.6.4 SFR and the Fundamental Metallicity Relation

We calculate the star formation rate (SFR) for the 14 objects with direct-measurement metallicities based on the line flux conversion given in Kennicutt (1998)

$$SFR(M_\odot \text{year}^{-1}) = 7.9 \cdot 10^{-42} L(H\alpha)(\text{erg s}^{-1}) \tag{3.8}$$

using the extinction-corrected $H\alpha$ line flux. The SFR error is estimated based on the line flux error. The metallicity as a function of SFR is shown in Figure 22, along with a non-linear

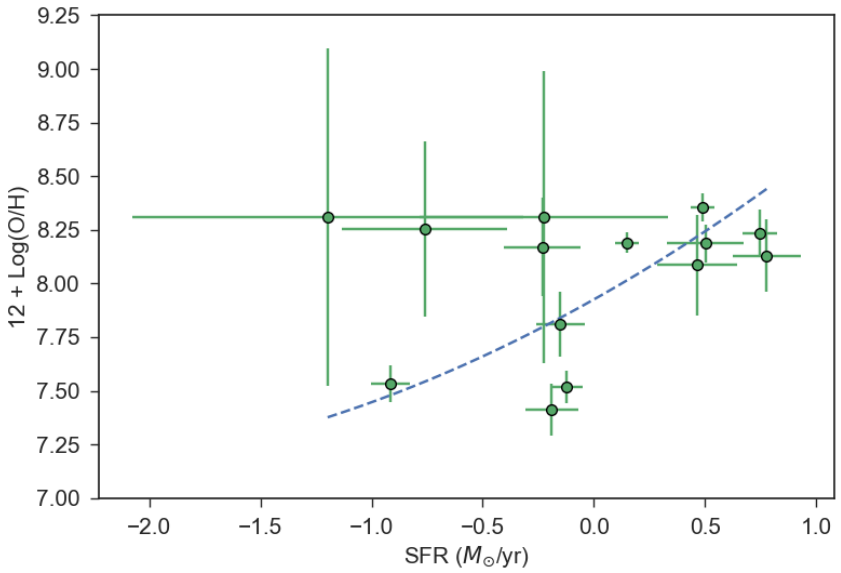

Figure 22: The gas-phase metallicity of the FIGS objects as a function of the SFR. The dashed line shows the non-linear least-squares fit, which shows a trend of increasing metallicity with increasing SFR.

fit. This shows a trend of metallicity increasing with the SFR. In Figure 23, we plot the gas-phase metallicity versus the Specific Star Formation Rate (SSFR), which is the SFR per stellar mass, as well as the fit of the FIGS objects. This shows a slight trend of declining metallicity with increased SSFR, with the lowest metallicity (and smallest mass) galaxies having SSFR $> 10^{-9}$ yr^{-1}. Ellison et al. (2008) has shown a relation where metallicity is lower for galaxies with higher SSFR at a given stellar mass, with a metallicity offset of up to 0.15 dex at the lowest stellar masses ($M_\star \sim 10^{8.5} M_\odot$ in their study). This suggests that the large SSFR we observe in several of the FIGS objects could be a driver for the low-metallicity offset compared to other mass-metallicity relations. If this is the case, it likely has implications for how star formation interacts with the nebular gas. There are two plausible scenarios. First, inflows of circumgalactic gas could both bring lower-metallicity gas into the galaxy and trigger new star formation, producing strong line emission in the metal-deficient medium around the new stars. Alternatively, recent star formation in a galaxy

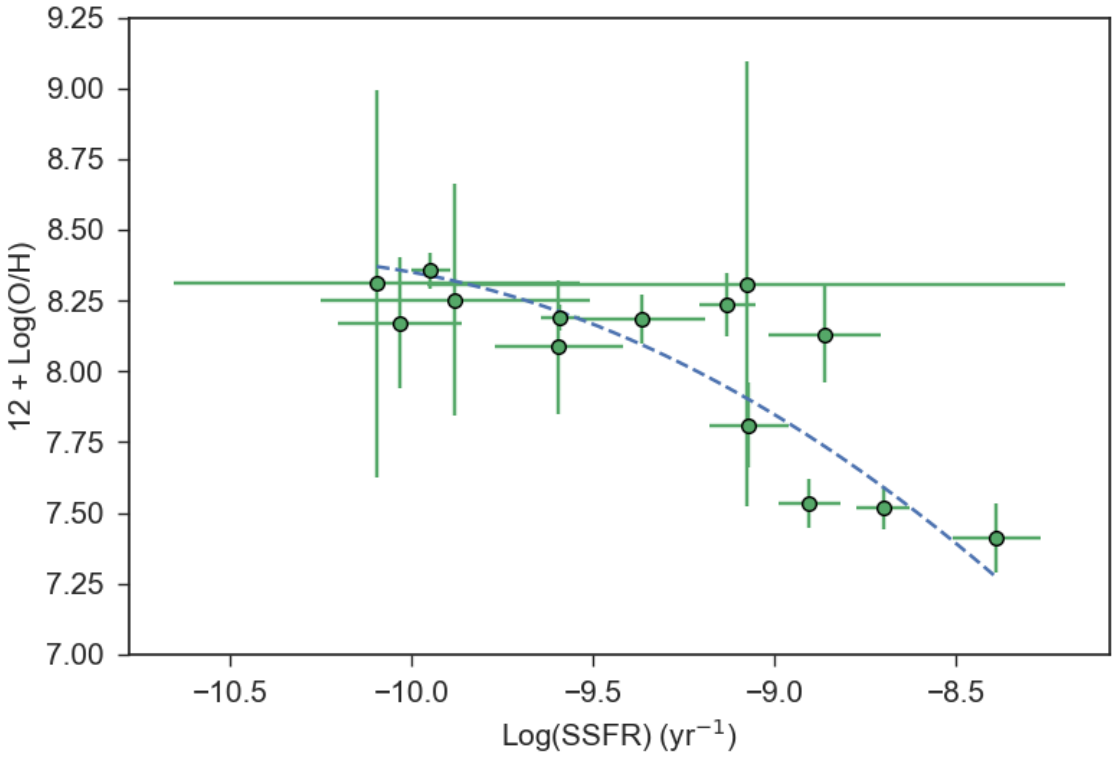

Figure 23: The gas-phase metallicity as a function of the specific star formation rate (SSFR). The dashed line shows the non-linear least-squares fit of the FIGS points.

produces strong stellar winds and supernovae, which could cause outflows that push the most metal-enriched gas out of the galaxy. In either case, increased star formation would show a clear link with measuring reduced metallicity in a galaxy's nebular gas.

Further investigation of the relationship between these parameters is needed. Mannucci et al. (2010) refers to the dependence of the gas-phase metallicity on stellar mass and the SFR as the Fundamental Metallicity Relation, for which they obtain the projection

$$12 + \log\left(\frac{O}{H}\right) = \log\left(\frac{M_\star}{M_\odot}\right) - 0.32 \cdot \log(SFR). \tag{3.9}$$

This projection, derived from a sample of SDSS $z = 0.07 - 0.30$ ELGs which had an Hα $S/N > 25$, minimizes the scatter in metallicity around the relation. Mannucci et

al. also find good agreement with the FMR and this projection for galaxies up to $z = 2.5$. We calculated this projected FMR for the FIGS galaxies with SFR, plotted in Figure 24, to see how well our results match this relation. The FIGS 14 objects follow the trend of the lower FMR, but sit lower on the plot due to their lower metallicities. This is perhaps partially accounted for by the differences between direct and R_{23} metallicity measurements as described in §3.6.1, though the metallicities used in Mannucci et al. were derived from either R_{23} or from the [NII]λ6584/Hα ratio. Mannucci et al. estimates a 0.09 dex offset in metallicity between these two methods, making the magnitude of the offset from R_{23} and direct measurements difficult to determine. Figure 24 also shows a difference in the range of values for the $M_\star$-SFR axis, with the Mannucci sample occupying a higher range of values than the FIGS sample. This is due to differences in stellar mass between the two samples. While the FIGS objects span a range of SFR similar to that seen in Mannucci et al., the $M_\star$ values are lower, and we do not know how well Mannucci's projection reduces scatter at lower stellar mass.

We also tried comparing our results to the Fundamental Plane of Metallicity (FPZ) derived by Hunt et al. (2016) using the Metallicity Evolution and Galaxy Assembly (MEGA) data set. Hunt et al. attempted to derive a fundamental relation between metallicity, mass, and SFR from a large set of galaxies with a wide range of properties and redshifts, including a variety of methods for measuring the metallicity (the direct method among them, but not predominantly so). With this data set, Hunt et al. performed a Principal Component Analysis to derive a plane relating the three variables:

$$12 + \log\left(\frac{O}{H}\right) = -0.14\log(SFR) + 0.37\log\left(\frac{M_\star}{M_\odot}\right) + 4.82 \tag{3.10}$$

In Figure 25, we plotted the FIGS objects on this plane. The blue line gives the one-to-one

correspondence given by Equation 3.10, with the shaded region providing the $\sigma = 0.16$ scatter from Hunt et al.'s narrowest residual distribution. The FIGS points lie systematically below this, though within the total scatter of MEGA objects around it. The dashed and dot-dashed lines show linear fits to the FIGS points: the red (dashed) line allows both parameters of the linear fit to move freely, while the purple (dot-dash) line assumes the same slope as the one-to-one correspondence and only lets the y-intercept vary. This produces an overall metallicity offset of ~ 0.3 dex. The linear fit demonstrates that the higher-metallicity FIGS ELGs are actually fairly consistent with 1σ range of the FPZ measure, and that the lowest-metallicity objects are the ones driving the offset.

This all suggests that our sample of galaxies with direct metallicity measurements includes some uniquely low-mass, low-metallicity objects.

3.7 Conclusions

By using near-infrared spectroscopy from FIGS, we were able to identify 71 ELGs in the GS1/HUDF field, primarily through the identification of Hα, [OIII]λ5007, and [OII]λ3727 emitters in the redshift range of $0.3 < z < 2.0$. We were able to confirm 41 out of the 71 ($\sim 58\%$) by identifying complementary lines in matching optical data, either with ACS grism spectroscopy from the previous GRAPES survey, or from new MUSE-VLT optical spectroscopy. We measure line fluxes down to a sensitivity of 10^{-17} ergs cm^{-2} s^{-1} in FIGS and $\sim 3 \cdot 10^{-19}$ ergs cm^{-2} s^{-1} from MUSE-VLT.

Out of these objects, we found 14 for which we were able to measure the auroral [OIII]4363 emission line in MUSE optical spectra with a S/N ratio of at least 3, with a redshift range of $0.3 < z < 0.8$ and with stellar masses down to $10^{7.9} M_{\odot}$. We used these measurements to calculate the gas-phase metallicity via the electron temperature, and from

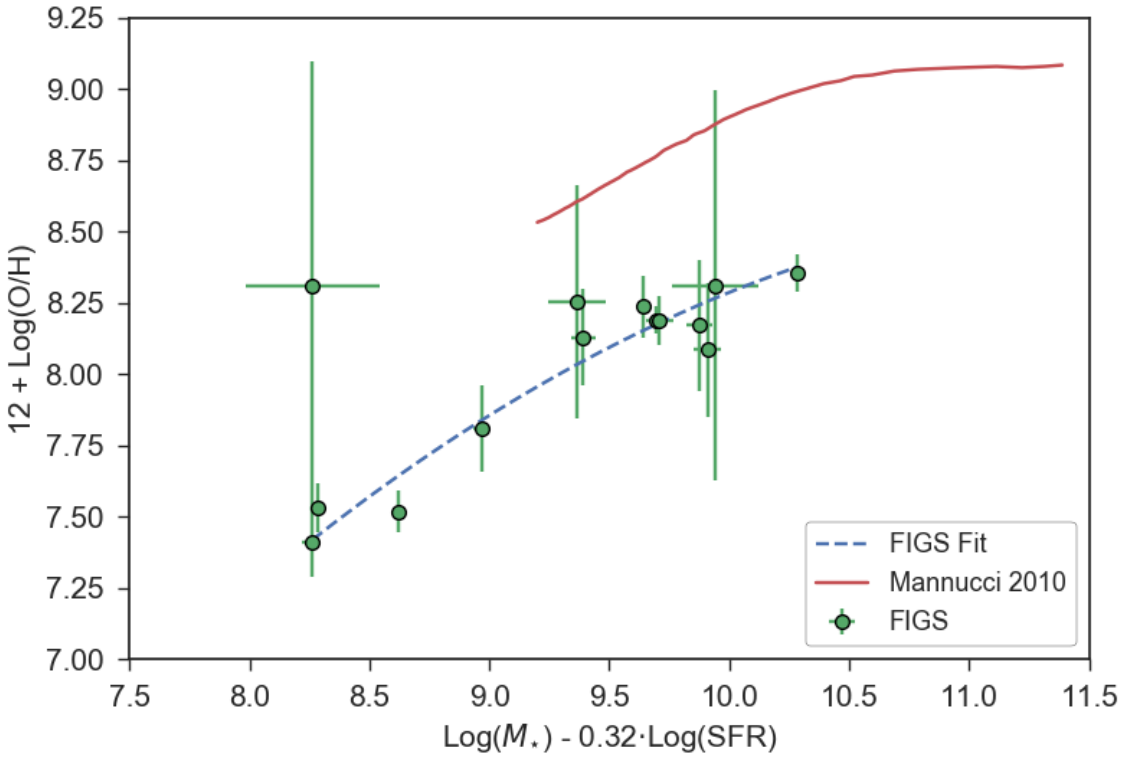

Figure 24: The gas-phase metallicity as a function of the Fundamental Metallicity Relation (FMR), as given by Mannucci et al. (2010). The Mannucci relation is shown by the red solid line, with the FIGS points in green. The blue dashed line gives the non-linear least-squares fit of the FIGS points.

this we produced a mass-metallicity relation. When compared to MZ relations at similar redshifts, we find a significant offset to lower metallicity. We examined several possible causes for the offset, and find that redshift evolution does not account for the difference in metallicity. The offset can be only partially explained by differences with this metallicity derivation method compared to the more common R_{23} method, as previously seen in Andrews & Martini (2013); Sanders et al. (2016). Selecting [OIII]4363 line emitters does select for lower metallicity in general, but with a new R_{23} calibration we found other galaxies at similarly low metallicity, so selection effects alone cannot account for the difference. To further explore the metallicity offset, we determined the SFR, SSFR, and FMR

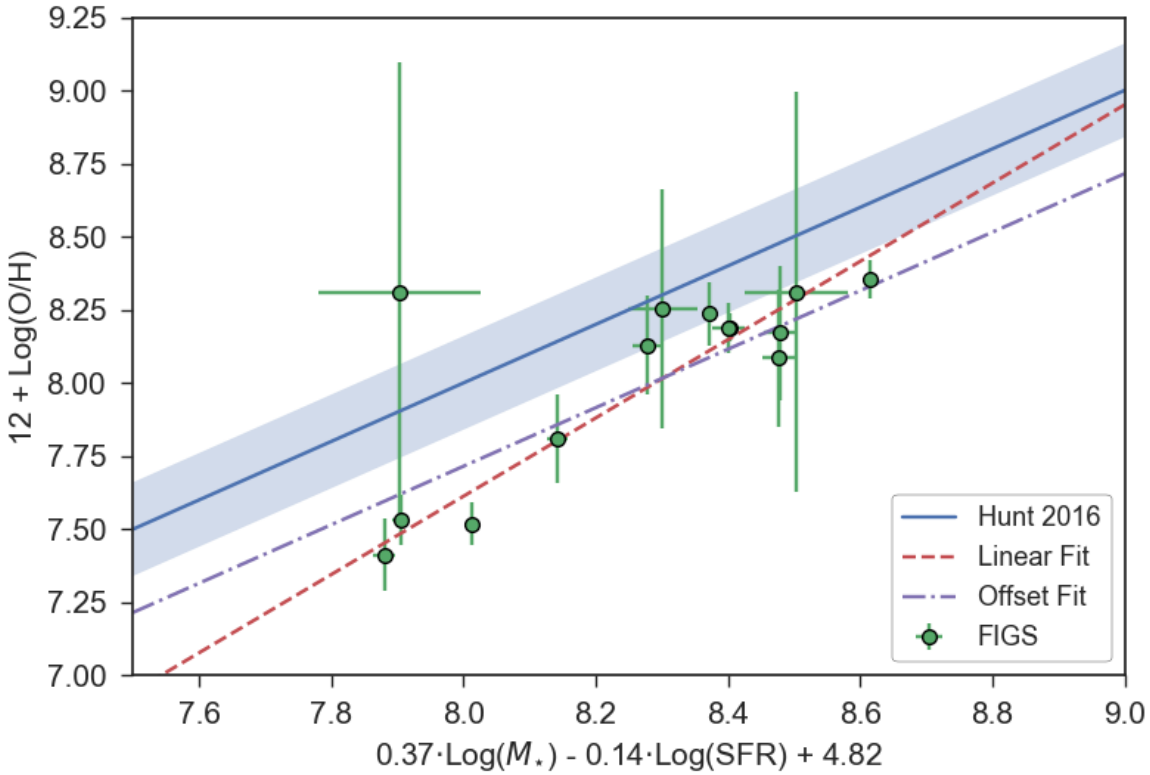

Figure 25: This plot shows the 14 direct-method FIGS objects plotted using the Fundamental Plane of Metallicity formulation from Hunt et al. (2016). The blue line shows the one-to-one correlation of metallicity to combined mass and SFR around which the formulation was based. The FIGS points are in green, and the dashed red line represents the simple linear fit to the FIGS data. The dot-dashed purple line shows the linear fit to the FIGS data if the slope is fixed to match the Hunt correlation. This results in a metallicity offset of 0.28.

for the sample. We find a trend between metallicity and SSFR, showing that the low-mass, low-metallicity FIGS objects have a large SSFR and are low-metallicity outliers in attempts to find a fundamental relationship between these parameters. This suggests that recent star formation is connected to inflows or outflows of nebular gas, leading to the measurement of low-metallicity gas in the galaxy. The existence of such outliers shows the need for further spectroscopic analysis of low-mass galaxies, which may be host to significant activity well after the universal peak of star formation at $z \simeq 2$.

Chapter 4

A CATALOG OF EMISSION-LINE GALAXIES: STUDYING ENVIRONMENTAL INFLUENCE ON STAR FORMATION

4.1 Abstract

We present a catalog of 208 $0.3 < z < 2.1$ Emission Line Galaxies (ELG) selected from 1D slitless spectroscopy obtained using Hubble's WFC3 G102 grism, as part of the Faint Infrared Grism Survey (FIGS). We identify ELG candidates by searching for significant peaks in all continuum-subtracted G102 spectra, and confirm candidates via emission lines in matching spectra, published spectroscopic redshifts, and photometric redshifts. We provide derived emission line fluxes and errors, redshifts, and equivalent widths (EW) for Hα $\lambda 6563$, [OIII]$\lambda\lambda 4959, 5007$, and [OII]$\lambda\lambda 3727$ emission lines, for emission line galaxies down to AB(F105W) > 28 and $> 10^{-17}$ erg cm^{-2} s^{-1} line flux. We use the resulting line catalog to investigate a possible relationship between line emission and a galaxy's environment. We use nearest-neighbor distances to investigate the typical surroundings of ELGs compared to non-ELGs, and we find that [OIII] emitters are preferentially found at intermediate galaxy densities near galaxy groups. We characterize these ELGs in terms of the galaxy specific star formation rate (SSFR) versus stellar mass, and find no significant influence of environment on that relation. We calculate star formation rates (SFR), and find no dependence of SFR on local galaxy surface density for $0.3 < z < 0.8$ Hα emitters and for $0.8 < z < 1.3$ [OIII] emitters. We find similar rates of close-pair interaction between ELGs and non-ELGs. These findings suggest that environmental factors do not have a consistent impact on inducing star formation.

4.2 Introduction

The detection and measurement of nebular line emission in galaxies has long been a useful tool in the study of galaxy evolution. Hydrogen recombination lines, such as Hα λ6563 and Hβ λ4861, and forbidden transitions in ionized oxygen, such as [OIII]$\lambda\lambda 4959, 5007$ and [OII]$\lambda 3727$, can be used to measure a galaxy's recent star formation (Kennicutt, 1998), its gas-phase composition (Kobulnicky & Zaritsky, 1999), and dust extinction (Calzetti et al., 1994), among other properties. Furthermore, the spectroscopic identification of an emission line enables the measurement of a galaxy's redshift with much higher precision than is achievable with methods relying on broadband photometry alone, even with relatively low-resolution slitless spectroscopy or narrowband photometry (Xu et al., 2007; Xia et al., 2011; Ferreras et al., 2014; Pharo et al., 2018). Measurements of fundamental galaxy properties like luminosity, as well as assessments of a galaxy's interactions with nearby galaxies and their environments, rely in part on this measure of distance.

Another key aspect of the study of galaxy evolution is the potential influence of a galaxy's surrounding environment on its development, particularly in how it relates to star formation. In the local universe, red, passive galaxies are associated with overdensities, while blue galaxies with active star formation (of which line emission is an indicator) are more likely found in low-density environments and dark matter halos (Dressler, 1980; Balogh et al., 2004; Kauffmann et al., 2004) and in galaxies with lower stellar mass (Pasquali et al., 2009). At higher redshift, the picture is less clear, with some studies matching the local result (Patel et al., 2009), while others find a weak star formation dependence on environment (Grützbauch et al., 2011; Scoville et al., 2013). Elbaz et al. (2007); Cooper et al. (2008); Tran et al. (2010) find that star formation activity correlates with density at high redshift, and Sobral et al. (2011) and Darvish et al. (2014) report an increase in star formation at

intermediate density, potentially associated with groups or filaments rather than rich clusters. In order to make clearer sense of this picture, further studies capable of accurately measuring both local environments and star formation are needed. The identification of line emission in galaxies can achieve this purpose.

Emission line galaxies (ELGs) can be detected in several ways. In principle, the most straightforward method is the use of ground-based spectroscopy, but this is not always practical for the faintest objects, requiring some pre-selection of targets and spectral features. Another common approach is the use of narrowband photometric surveys (e.g., Boroson et al., 1993; Rhoads et al., 2001; Geach et al., 2008; Sobral et al., 2011, 2012; Coughlin et al., 2018), which detect emission lines by measuring the flux excess between narrowband photometry and nearby broadband photometry. This method is useful for obtaining a large number of detections, but these detections are limited to a narrow redshift window defined by the width of the narrowband.

A third approach for ELG detection is the use of low-resolution, slitless spectroscopy. Recent surveys have made use of the Hubble Space Telescope's (HST) ACS (APPLES, Pasquali et al., 2003; GRAPES, Pirzkal et al.; Malhotra et al.; Rhoads et al., 2004; PEARS, Pirzkal et al.; Rhoads et al., 2009), Wide-Field Camera 3 (WFC3) G102 (WISP, Atek et al., 2010; GLASS, Treu et al., 2015; FIGS, Pirzkal et al., 2018), and G141 (WISP, Atek et al., 2010; GLASS, Treu et al., 2015; 3D-HST, Momcheva et al., 2016) grisms to identify ELGs over a broad redshift range ($0 < z < 7.5$) and without a pre-selection of targets that might exclude continuum-faint sources (Rhoads et al., 2013; Tilvi et al., 2016; Larson et al., 2018). In the Faint Infrared Grism Survey (FIGS; Pirzkal et al., 2017), we apply this approach with deep WFC3 G102 observations taken at multiple position angles in order to maximize emission line sensitivity, minimize spectral contamination, and more accurately measure

the central wavelengths of emission lines (Xu et al., 2007; Straughn et al., 2008, 2009; Xia et al., 2011, 2012; Pirzkal et al., 2013).

The FIGS grism data therefore provides an opportunity to study how an ELG's emission properties relate to its environment. First, the slitless grism selection enables the unbiased detection of continuum-faint ELGs, which can be used for a study of star formation in the FIGS fields. Second, grism studies have shown that the combination of grism spectroscopy with broadband photometry can significantly improve photometric redshift accuracy (Ryan et al., 2007; Brammer et al., 2012; Pharo et al., 2018), and that these improved redshift catalogs can be used to better identify and study galaxy overdensities (Pharo et al., 2018). With FIGS data, we can then measure emission lines and star formation rates (SFRs) across a broad redshift range, and evaluate their local environments using improved grism redshifts.

In this paper, we present a catalog of emission line galaxies derived from an automated search of 1D slitless spectra from FIGS obtained with HST's WFC3 G102 grism. In this catalog, we list the line fluxes, redshifts, and observed equivalent widths (EW) for 208 strong-line (Hα, [OIII]$\lambda\lambda 5007, 4959$, and [OII]$\lambda 3727$) emitters in a redshift range of $0.3 < z < 2.1$. We then combine this catalog with a previous study of overdensities in the FIGS fields to study ELG properties as a function of their local galaxy environment. In §4.3, we briefly describe the FIGS data collection and reduction, as well as the sources of additional spectra we used to supplement our study. In §4.4, we detail our search methods for identifying and confirming ELG candidates in 1D spectra. In §4.5, we describe our line flux measurements, present the final ELG catalog, and summarize its properties. In §4.6, we study these properties as functions of the local environment and stellar mass. For this paper we will use $H_0 = 67.3$ km s^{-1} Mpc^{-1} and $\Omega_M = 0.315$, $\Omega_\Lambda = 0.685$ (Planck Collaboration et al., 2014). All magnitudes are given in the AB system (Oke & Gunn, 1983).

4.3 Survey Description and Data

4.3.1 FIGS Observations

The Faint Infrared Grism Survey (FIGS, HST Cycle 22, PID:13779, PI S. Malhotra) used the HST WFC3-G102 infrared grism (see Figure 26) to obtain deep slitless spectroscopy of $\sim$ 6000 galaxies. FIGS achieved 40-orbit depth in 4 fields, designated GN1, GN2, GS1 (HUDF), and GS2 (HDF-PAR2). Objects in each field were observed in 5 different 8-orbit position angles (PAs) in order to mitigate the contamination of spectra from overlapping spectra from nearby objects. Each PA covers a 2.05'x2.27' field of view. The total area of coverage over all fields is 17.7 square arcminutes.

4.3.2 Spectral Extraction and Properties

In this paper, we used 1D spectra which were generated using the methods described in Pirzkal et al. (2017). Here we briefly summarize this process. We reduced FIGS data in a manner that loosely follows the method used for GRAPES and PEARS, the previous deep HST grism surveys (Pirzkal et al., 2004; Malhotra et al., 2005; Xu et al., 2007; Rhoads et al., 2009; Straughn et al., 2009; Xia et al., 2012; Pirzkal et al., 2013). First, we generated a master catalog of sources from deep CANDELS survey mosaics in the F850LP filter in ACS and the F125W and F160W filters in WFC3 (approximately the z, J, and H bands; Grogin et al., 2011; Koekemoer et al., 2011). We astrometrically corrected the data to match the absolute astrometry of the GOODS V2.0 catalogs. We estimated the background levels of the grism observations by using a two-component model, which included a constant Zodiacal light background as well as a varying He I light background. To generate the

individual spectra, we used a Simulation Based Extraction (SBE) approach that accounts for spectral contamination from overlapping spectra, as well as allowing the use of an optimal extraction approach (Horne, 1986) when generating 1D spectra from 2D spectra. We refer the reader to Pirzkal et al. (2017) for a complete description of these processes. We initially extracted all sources down to a continuum level of F105W < 30 mag. When the extractions were complete, we had an average of ~ 1700 spectra per field, with a typical 3σ continuum detection limit of $m_{F105W} = 26$ mag and an emission line sensitivity of 10^{-17} erg cm^{-2} s^{-1}.

The middle panel of Figure 26 shows the throughput curve for the G102 grism compared to other spectral and broadband curves. We restricted use of the G102 spectra to wavelengths between 8500 and 11500 Å, where the grism throughput is greater than 20%.

4.3.3 Additional Spectral Data

4.3.3.1 MUSE/VLT

For the GS1/HUDF FIGS field, we supplemented our infrared FIGS spectra with deep archival high-resolution optical IFU spectra taken with the Multi-Unit Spectroscopic Explorer (MUSE) instrument (Bacon et al., 2010) from the Very Large Telescope (VLT). This expands the available spectroscopic wavelength coverage for the GS1 field considerably, enabling confirmation of detected emission lines in FIGS via the identification of complementary emission lines at optical wavelengths, even for many faint sources. We used the publicly available IFU spectra from the MUSE Hubble Ultra Deep Survey (Bacon et al., 2017), a mosaic of nine 1×1 arcmin^2 MUSE fields in the HUDF. In order to extract spectra for emission-line objects in our sample, we first used the known sky coordinates for each object in FIGS to find RA-Dec matches in the MUSE data. At each wavelength slice, we placed a 2 arsecond aperture centered on the object, which

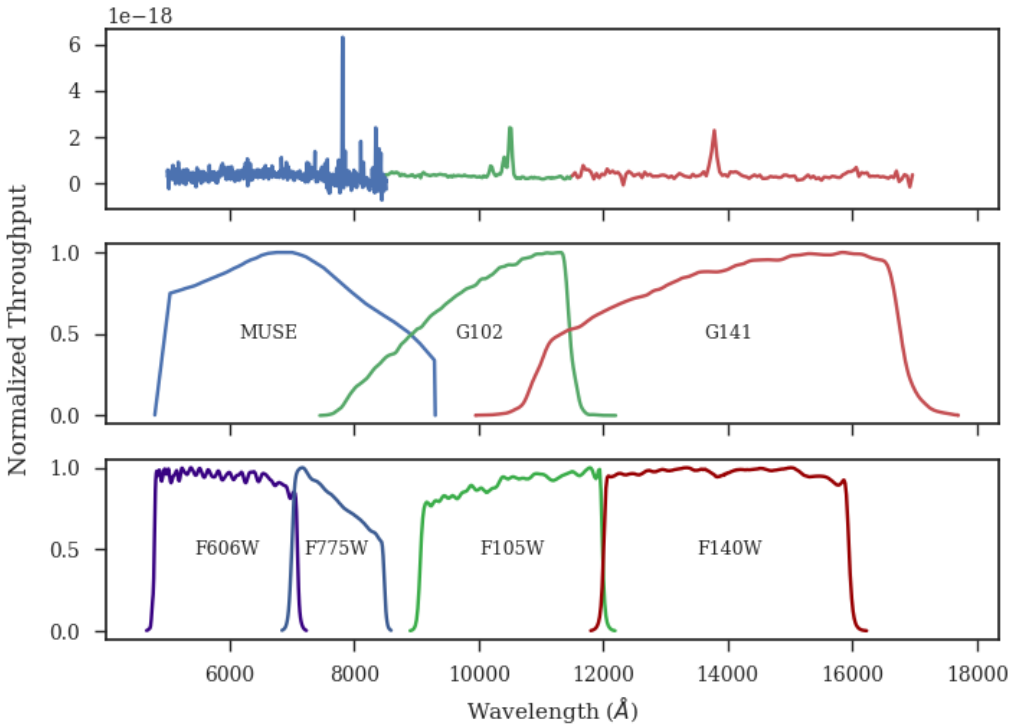

Figure 26: The top panel shows the spectrum of an example ELG from FIGS at z=1.098, with spectra from MUSE/VLT (blue), the HST WFC3 G102 grism (green), and the G141 grism (red). The y-axis for this panel is F_λ. The middle panel gives the throughput curves for each spectrograph, normalized to the maximum throughput of each. The lower panel shows the throughput curves for HST photometric bands at comparable wavelengths. In this example, [OIII]$\lambda\lambda$4959,5007 are detected in the FIGS G102 spectrum, with Hα+[NII] detected in G141, and [OII]3727 detected in MUSE/VLT.

we determined was able to capture the total flux from most line-emitting sources at the redshifts considered. Then, we generated 1D spectra for the matched objects by summing up the flux within the aperture at each wavelength, across the entire MUSE wavelength range (see Figure 26 for the MUSE wavelength coverage compared to WFC3 G102). This produced a catalog of extracted FIGS candidate spectra from the reduced MUSE datacube. The MUSE data wavelength coverage extends from 4752 Å to 9347 Å with a spectral resolution of 2.3 Å, though the sensitivity begins to drop off at wavelengths lower than 5000 Å, and at wavelengths higher than 9200 Å, the noise from sky emission begins to

dominate, so we restrict our usage of the MUSE spectra to between these wavelengths. MUSE has a 3σ line sensitivity of $\sim 3 \cdot 10^{-19}$ erg cm^{-2} s^{-1}, and thus should detect lines of strength comparable to or even considerably less than the lines found in FIGS G102 spectra.

4.3.3.2 IDs from GRAPES

In the GS1/HUDF field, we were also able to make use of line identifications from the Grism ACS Program for Extragalactic Science (GRAPES) (Xu et al., 2007), which used the G800L grism from HST ACS, a low-resolution (40 Å per pixel at 8000 Å) optical grism. Xu et al. (2007) were able to identify lines from ~ 6000 Å to ~ 9500 Å, a similar region of coverage to VLT/MUSE. This enabled us to search for complementary optical lines for FIGS sources while simultaneously confirming some ELGs from GRAPES.

4.3.3.3 G141 Grism Data

In the other FIGS fields (GN1, GN2, GS2), we also made use of archival WFC3 G141 grism spectra collected in HST proposal 13266 from WISPS (Atek et al., 2010) and 3D-HST (Brammer et al., 2012). Inclusion of this data effectively extended the FIGS spectral coverage out to ~ 1.7 micron. The additional G141 spectra are not as deep as the FIGS G102 data, with $> 90\%$ completeness down to J< 24 mag (Ryan, 2013). They also have lower spectral resolution than the WFC3 G102 spectra (46.5 Å per pixel at 14000 Å) and thus were of limited use for candidate confirmation, but they allowed for the detection of strong line

emission in some objects.

4.3.3.4 Spectroscopic Redshifts

We assembled compilations of published high-quality spectroscopic redshifts (spec-zs) in the GOODS-N and CDFS fields (N. Hathi, private communication). These fields are well-studied, and the existence of independent spectroscopy allowed us to confirm the emission-line-derived redshifts (and thus, the identified emission line) of some of our brighter sources. Many of the published spec-z catalogs included quality designations distinguishing the reliability of different spectra. The exact scales of quality used differed somewhat between surveys, but we generally used only those results deemed “good" or better by the original survey. Our compilations included spec-zs from Wirth et al. (2004), Malhotra et al. (2005), Grazian et al. (2006), Pasquali et al. (2006), Reddy et al. (2006), Ravikumar et al. (2007), Barger et al. (2008), Hathi et al. (2008), Straughn et al. (2008), Vanzella et al. (2008), Wuyts et al. (2008), Ferreras et al. (2009), Hathi et al. (2009), Rhoads et al. (2009), Straughn et al. (2009), Vanzella et al. (2009), Wuyts et al. (2009), Balestra et al. (2010), Silverman et al. (2010), Yoshikawa et al. (2010), Cooper et al. (2011), Xue et al. (2011), Cooper et al. (2012), Ono et al. (2012), Finkelstein et al. (2013), Kurk et al. (2013), Le Fèvre et al. (2013), Pirzkal et al. (2013), Trump et al. (2013), Song et al. (2014), Kriek et al. (2015), Le Fèvre et al. (2015), Morris et al. (2015), Wirth et al. (2015), Trump et al. (2015), Momcheva et al. (2016), Herenz et al. (2017), Inami et al. (2017), and McLure et al. (2018).

4.4 Emission Line Identification Methods

4.4.1 Search for ELG Candidates

We conducted a blind search for ELGs among the FIGS 1D spectra. Because we obtained our infrared spectra via slitless grism spectroscopy, there was no pre-selection of ELG candidates before the search via the placement of slits or by broadband magnitude cutoffs. This had the advantage of enabling the detection of ELGs with potentially very low continuum levels, and so might allow for the identification and study of smaller and/or fainter galaxies with nebular line emission. However, this did require an efficient method for selecting ELG candidates from the total sample of FIGS spectra. In order to search the ~ 6000 FIGS spectra for emission lines, we developed a code to automatically search for and identify significant peaks in a 1D spectrum.

First, the level of the continuum flux had to be estimated at each wavelength element in the 1D spectrum. To measure this, we used a median-flux filter, which assumes a prospective line width and calculates the local continuum from the median flux outside that line width, in wavelength regions on either side of the line. A given wavelength λ_0 is taken to be the center of a potential line. The potential line flux is measured as all the flux contained within a line width $2\Delta\lambda_1$, so that the algorithm defines the potential line as the region covered by

$$\lambda_0 - \Delta\lambda_1 < \lambda < \lambda_0 + \Delta\lambda_1 \tag{4.1}$$

Then the code estimates the nearby continuum by looking at regions to either side of the line with width $\Delta\lambda_2$. The nearby continuum is defined then as the regions contained in

$$(\lambda_0 - \Delta\lambda_1) - \Delta\lambda_2 < \lambda < (\lambda_0 - \Delta\lambda_1) \text{ and } (\lambda_0 + \Delta\lambda_1) < \lambda < (\lambda + \Delta\lambda_1) + \Delta\lambda_2 \quad (4.2)$$

The algorithm then takes the median flux of the wavelength pixels constrained by Equation 4.2 as an estimate of the local continuum around the hypothetical line, and subtracts this flux from the flux at λ_0 in order to obtain the continuum-subtracted or residual flux at that point. If there is a line present at λ_0, this method allows for measurement of the level of the continuum without influence from the line flux. The code takes the standard deviation among this set of fluxes as an estimate of the flux error at λ_0. The algorithm repeats this process, iterating over each wavelength element in a given spectrum, estimating the continuum flux at that wavelength, and subtracting it. See Figure 27 for an example continuum-subtracted spectrum. We were able to best minimize false detections while retaining real ones with $2\Delta\lambda_1 = 122.5$ Å and $\Delta\lambda_2 = 147$ Å, based on tests of variable $\Delta\lambda_1$ and $\Delta\lambda_2$ with a preliminary subsample of ELGs with matching spectroscopic redshifts.

After the spectrum is continuum-subtracted, the code calculates the signal-to-noise ratio (S/N) at each wavelength with the residual flux and the flux error, once more iterating through the list of wavelength elements. The sum of the fluxes constrained by Equation 4.1 determines the hypothetical line signal, and the estimated flux errors added in quadrature measure the noise of the hypothetical line. After this calculation is complete for all wavelengths, the algorithm identifies the location with maximum line S/N in the spectrum. If $S/N > 5$, we fit a Gaussian at the central wavelength element from which we obtain a measure of the continuum-subtracted integrated line flux. The code then subtracts the fit line from the residual flux spectrum and checks the next-highest S/N. If the S/N ratio still exceeds 5, the routine repeats until the peak S/N ratio is below the detection threshold.

We run this routine on the individual PA spectra in each field, and record all instances of $S/N > 5$. If the code finds a peak in at least two PAs with centroids at the same or

adjacent wavelength elements (24.5 Å in either direction), it declares a detection. Lower S/N thresholds produced numerous false positives, so we used the $S/N > 5$ cutoff to maintain a more robust sample. We avoided using simultaneous fits of all PAs in order to avoid including contaminated PAs in a combined significance measurement. With individual PA fits, contaminated detections could more easily be identified and removed. After running the routine over all galaxies in the field, the list of detections forms an ELG candidate list.

4.4.2 Line Identification and Confirmation

Once we had obtained lists of candidate detections for each field, we next attempted to identify the type of emission line detected in each spectrum. First, we matched the candidate lists to our photometric redshift (photo-z) catalog (Pharo et al., 2018) and assigned a preliminary line ID based on the likely redshift. For the purposes of this result, we focused on three strong line IDs that could be robustly detected at FIGS resolution and sensitivity: H$\alpha\lambda$6563, [OIII]$\lambda\lambda$4959,5007, and [OII]λ3727. We did this because these lines typically have the strongest emission, and therefore can be detected robustly, and because they are common features of star-forming galaxies. Hβ4861 could theoretically be resolved and detected alongside [OIII], but was typically faint enough that it was difficult to detect at a significant level. Other FIGS studies have looked at Lyα line emission at higher redshifts (Tilvi et al., 2016; Larson et al., 2018).

After the preliminary photo-z identification, we sought to confirm the existence and type of the line by checking the detection against ancillary data. The most straightforward way to do this was to check for other emission lines. Since the wavelength ratio between a given pair of emission lines is invariant across redshift, the detection of two strong lines is a useful check. For eight candidates, two strong lines were measured in the FIGS G102 spectra alone, and for 59 others we identified pairs by checking matched ACS, MUSE/VLT,

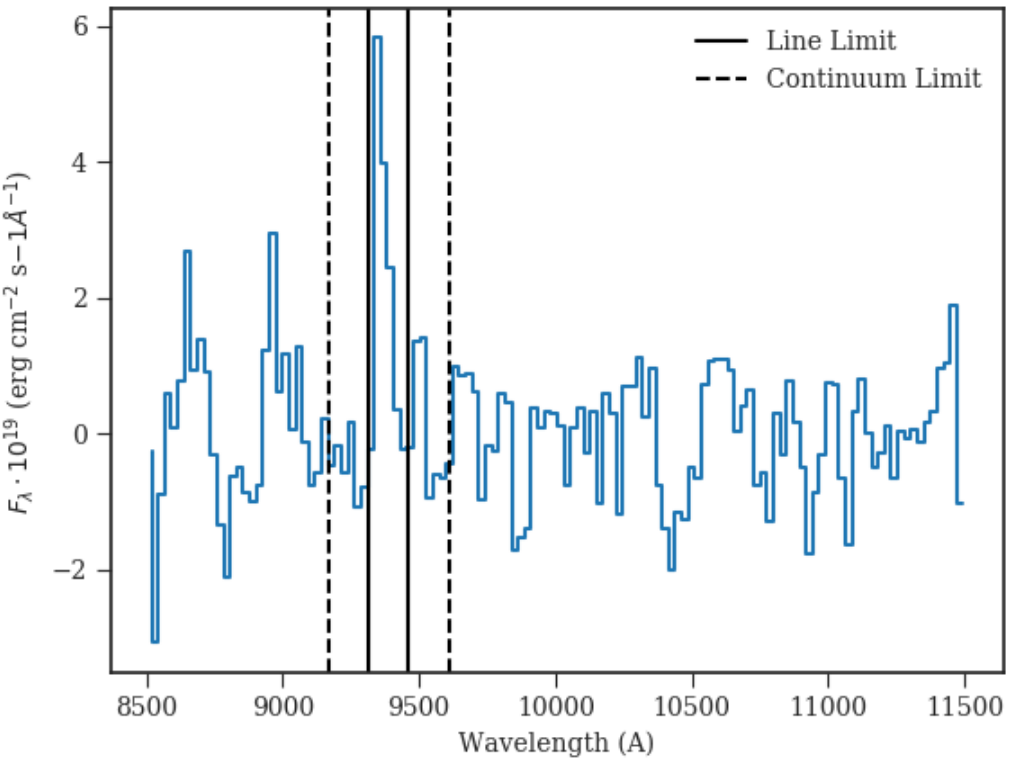

Figure 27: The continuum-subtracted 1D spectrum of one position angle of one FIGS ELG: ID GS1-2375. This figure shows a snapshot of the continuum-subtraction and line-finding routine. The routine identifies a “test line" region with a given pixel width, shown here as the region contained within the solid vertical lines. Next the routine uses the pixels between the solid lines and the dashed lines to estimate the local continuum flux, and subtracts that flux from the test line. Then the routine estimates the S/N ratio of the continuum-subtracted test line, and if the ratio surpasses the 5σ threshold, it reports a possible detection. This process iterates over each wavelength element in the spectrum.

and G141 spectra (described in §4.3.3). This most commonly involved finding Hα-[OIII] and [OIII]-[OII] pairs. Occasionally, we were able to identify another spectral feature, such as a strong 4000 Å break, in order to confirm the redshift. We note that while finding a matching line can confirm a line detection, not finding a matching line does not necessarily mean the detection is false, since the true relative line strengths are not known ahead of time. The matching line may be sufficiently weaker than the FIGS line, or the matching spectra sufficiently shallow, such that the matching line is not detected.

If matching spectra were not available, or a strong line was not identified, we next checked for a matching spectroscopic redshift (spec-z). If a spec-z assigned the line peak-wavelength a restframe wavelength that matched an emission line within the wavelength range of a FIGS grism element, we assigned the line the spec-z ID. If neither matching lines nor spec-z IDs were available, then we let the photo-z identification stand.

In each field, there were a handful of objects with a significant detection but no good redshift measurement. These were almost all very continuum faint (F105W > 27.5 mag) objects, which both reduced the availability of broadband fluxes to use for redshift fits and made the spectra more susceptible to contamination from nearby sources. Consequently, most of these candidates were removed through visual inspection, leaving four likely ELGs with no redshift: GS1-1062, GS2-532, GS2-838, and GS2-1624.

With the lines identified, we compared our results to the line list derived from Pirzkal et al. (2018), a study of FIGS strong line emitters using a distinct identification method with FIGS 2D spectra. In this paper, we do an independent selection and measurement of ELGs so as not to bias the findings of different search methods. However, we have compared our line candidates with those found in Pirzkal et al. (2018) and find them to be in close agreement, with a 90% match in identifications. A complete match would have been highly unlikely, as the methods have different strengths. The 2D method likely performs better at

identifying broader lines that are wider than the median filter used with the 1D search. The 1D method can detect lines with fewer PAs and nearer the edges of the field.

4.5 Flux Catalog

With a robust ELG list, we next systematically fit the strong emission lines in order to obtain flux measurements and more precise line centers (and therefore redshifts). To do this, we used a combined Gaussian fit to the line and power-law fit to the local continuum, using a Python coding package called *lmfit* (Newville et al., 2014). The peak-finding routine (§4.4.1) provided first estimates for the wavelength of the line center and the flux level of the nearby continuum. We restricted the possible wavelength of the line center allowed by the fit to only vary by the width of one grism element in either direction from this initial guess.

For the Hα line, the nearby [NII]$\lambda\lambda$6548,6584 lines are blended with Hα in the G102 grism, so that our recorded Hα fluxes are actually the combined fluxes of these three lines. Faisst et al. (2018) have derived an empirical estimate of the [NII]/Hα ratio in G102 as a function of redshift and stellar mass for $0 < z < 2.7$ and $8.5 < \log(M_\star/M_\odot) < 11.0$. This empirical relation gives a fractional flux ranging from 5% to 45%. For the [OIII]$\lambda\lambda$4959,5007 lines, we simultaneously fit two Gaussians and the continuum, with an additional restriction that the flux ratio of the two Gaussians match the theoretical intensity ratio of 2.98 for the two lines derived in Storey & Zeippen (2000). The [OII]$\lambda\lambda 3727, 3729$ doublet is too close to be resolved separately in FIGS spectra, and so is measured and reported together.

We ran this fitting procedure on each strong line in each PA that yielded a detection, and we averaged the fits for each line to obtain a final observed flux measurement. To get the flux error, we first estimated the error of the flux of each pixel from the standard deviation in the flux of the nearby continuum pixels. Then we propagated these errors with the line fit to

produce the total error for the integrated line flux. This method typically produced a larger and more realistic flux error than relying on the derived error of the fit parameters, which was often artificially small resulting from the constraints on the fit.

We summarize the median properties of each type of strong line-emitter in Table 15. We give the full emission line catalog, including individual line fluxes, redshifts, continuum magnitudes, and equivalents widths in a table in Appendix B. Figure 28 gives the redshift distribution of the lines, covering $0.3 < z < 2.1$, which is the full redshift coverage sampled by these three strong lines. Each line type's redshift distribution is set by the wavelength coverage of the grism, though there is some overlap between Hα and [OIII] and between [OIII] and [OII], as shown by the stacked bars. The bin sizes in the histogram scale with $0.03 \cdot (1 + z)$, so that the bin sizes roughly correspond to the grism redshift error. We find 81 [OIII] emitters, more than each of the other two (71 Hα, 56 [OII]), likely because it spans more volume coverage than the lower-z Hα while having less redshift dimming than the higher-z [OII].

Figure 29 shows the distributions of some other properties of the ELG catalog. The leftmost panel gives the distribution of the observed line fluxes without correction for dust or redshift dimming for the three types of strong line emitter. This also shows the minimum line flux we were able to robustly measure, down to 10^{-17} erg cm^{-2} s^{-1}. The faintest ELGs are dominated by [OII]λ3727, and the brightest are dominated by the lower-redshift Hα, with [OIII]$\lambda\lambda$4959,5007 spanning a broad range. Figure 29 also shows the distribution of F105W continuum magnitudes in the middle panel, showing that we detect ELGs for F105W up to 28 mag. Finally, the rightmost panel in Figure 29 gives the distribution of observed equivalent widths. Given the G102 resolution of $R = 210$, detections begin to drop off significantly for EW< 30 Å.

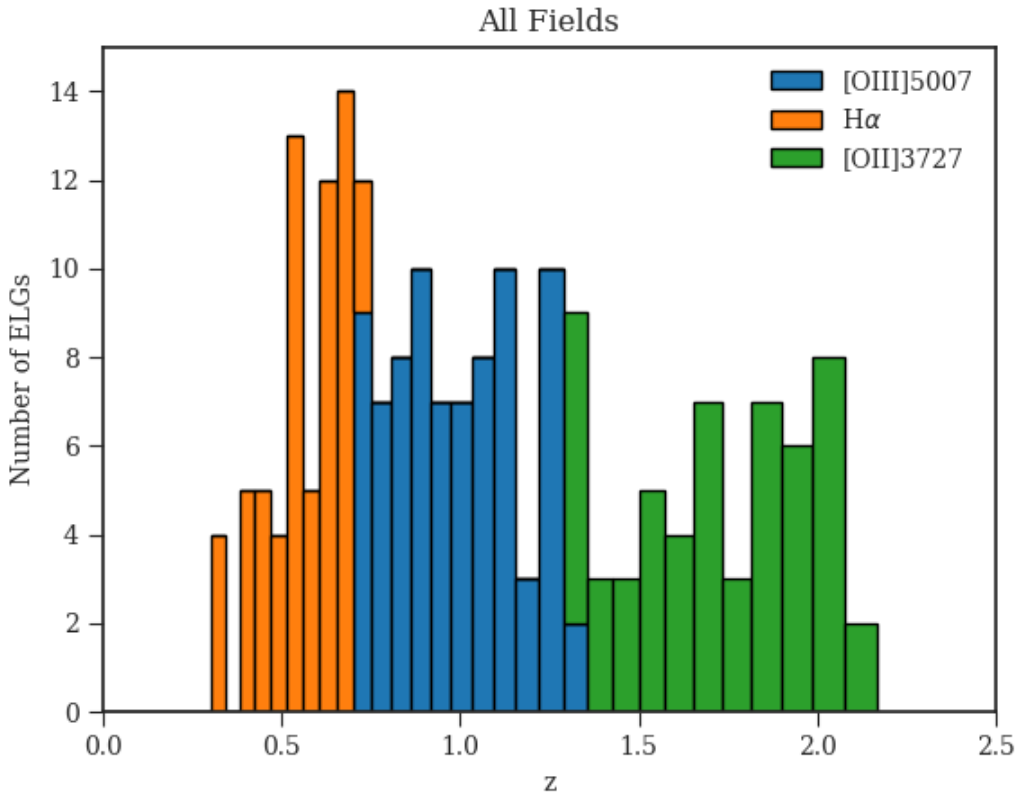

Figure 28: The distribution of identified ELGs by redshift. The histogram bins are scaled by $\Delta z = 0.03 \cdot (1 + z)$ in order to encompass the expected redshift error derived from our redshift catalogs (though many individual objects have additional spectroscopic confirmation, and thus their real error is much lower). The bars of the histogram are colored according to the FIGS strong line ID, and redshift bins that contain more than one type of line in FIGS have stacked bars of two colors, so that the height of the stack is still the total number of objects in the bin.

Table 15: Median Properties of Emission Line Galaxies

Line	Number	z	Flux (erg cm^{-2} s^{-1})	σ_F/F[a]	F105W Mag	EW (Å)
H$\alpha\lambda$6563	71	0.56	$8.1 \cdot 10^{-17}$	14%	22.9	42
[OIII] $\lambda\lambda$4959,5007	81	0.99	$5.3 \cdot 10^{-17}$	21%	24.3	67
[OII] λ3727	56	1.76	$3.5 \cdot 10^{-17}$	20%	24.2	53

[a] The median flux error as a percentage of the median line flux.

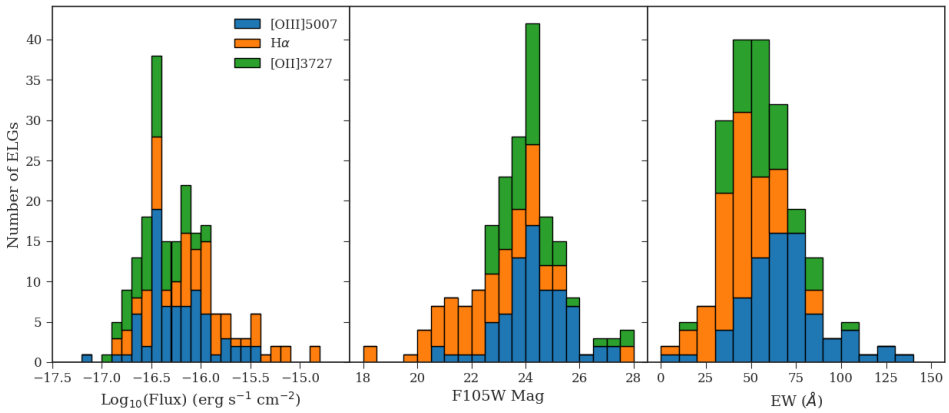

Figure 29: The distributions of ELG properties broken down by line ID. The histogram bars are colored according to the FIGS strong line ID, and bins that contain more than one type of line in FIGS have stacked bars of two or three colors. *Left:* The distribution of emission line fluxes given without correction for dust extinction. *Middle:* The distribution of identified ELGs by broadband F105W magnitude, in bins of 0.5 mag. *Right:* The distribution of observed equivalent widths (EW) in bins of 10 Å. The median values for each line in each quantity are given in Table 15.

4.6 ELG-Overdensity Relation

With a robust catalog of ELGs and their fluxes complete, in this section we use the catalog to probe ELG environments and explore how those environments relate to ELG properties.

4.6.1 FIGS Overdensity Catalog

In Pharo et al. (2018), we used redshift catalogs derived from combined FIGS grism spectroscopy and broadband photometry to search for significant overdensities of galaxies in the FIGS fields. First, we divided each field into slices of redshift with $\Delta z = 0.03 \cdot (1 + z_{min})$, where z_{min} is the lower bound of the redshift slice. In each redshift slice, we conducted a 7th-nearest-neighbor density search for a grid of points in the field. This is defined as

$$n_7 = \frac{N}{\pi R_7^2} \tag{4.3}$$

where $N = 7$ and R_7 is the angular distance to the 7th-nearest galaxy in that redshift slice.

We then checked for points of significant overdensity with two different metrics. First, we calculated $\mathcal{M}$, the largest value of n_7 in the slice normalized to the slice's median n_7. We also calculated $\mathcal{S}$, the peak nearest-neighbor density in the redshift slice divided by the standard deviation of densities in the adjacent redshift slices. We counted peaks with $\mathcal{M} = 10$ or $\mathcal{S} = 10$ as significant detections, based on comparisons with other nearest-neighbor density searches (Spitler et al., 2012) and the values for spectroscopically identified clusters (see Pharo et al. 2018 for more detail). Across the 4 FIGS fields, we identified 24 such overdensities, as well as determining the R_7 values for individual FIGS galaxies. We make use of both the proximity to a detected overdensity and the R_7 distance of a galaxy to study environmental effects in the subsequent sections.

Figure 30 shows a nearest-neighbor density plot in the FIGS GN1 field in which we detected a significant overdensity at $z = 0.69$. The figure also shows the locations of identified ELGs in the redshift slice, including several that appear associated with the location of the overdensity. However, it also shows two ELGs relatively far from the peak overdensity, suggesting that we can't simply use the presence of an ELG in the same redshift slice as an overdensity to link the two.

4.6.2 The R_7 Distribution

In order to systematically study a possible relationship between strong line emission and galaxy environment, we first looked at the R_7 distance for both ELGs and regular galaxies. If ELGs have a preferred relationship with overdensities, then the distribution of R_7 distances

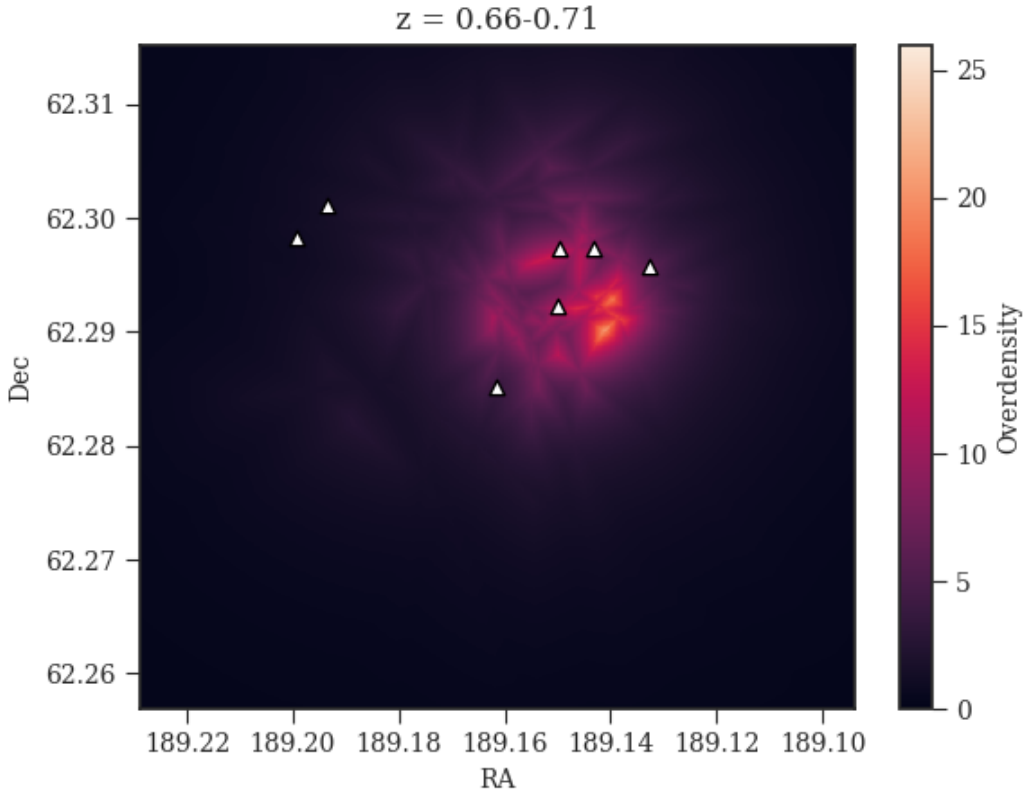

Figure 30: An example overdensity detected in GN1. This shows the redshift slice $\Delta z = 0.66 - 0.71$ shaded by measured overdensity, in this case the $\mathcal{M}$ term (see §4.6.1 for definition), as calculated from all galaxies in the redshift slice. ELGs in the same redshift slices are plotted as white triangles, in this case representing Hα emitters.

could be distinct from non-emitting galaxies, since, for example, a preference for ELGs to be close to overdensities should result in a distribution that peaks more at low R_7.

Figure 31 shows the probability density distributions of R_7 distances for ELGs compared to the whole set of galaxies in our redshift catalog. The distributions are broken down into six subsamples, in order to make meaningful comparisons of distance and stellar mass: first, by redshift ranges corresponding to the three strong emitters, and then by bright and faint F105W continuum magnitudes as a proxy for mass. To judge the significance of the differences between a given pair of distributions, we applied a two-sample Kolmogorov-Smirnov (KS)

test, a statistical test to determine whether two underlying one-dimensional probability distributions differ, to each subsample pair. The test produces a p-value determined by the sizes and differences of the two distributions, and this p-value gives the level of significance at which the two may be considered distinct. A lower p-value corresponds to a more significant determination that the two distributions are different.

This test showed no significant difference in the R_7 distribution of Hα emitters compared to other galaxies in either the bright or faint bins. For [OIII]$\lambda\lambda$4959,5007 emitters, the test does find a significant difference in distributions for both the bright ($p = 3 \cdot 10^{-7}$) and faint ($p = 0.02$) bins, with [OIII]$\lambda\lambda$4959,5007 emitters having a higher probability of appearing at mid-range R_7 distances compared to other galaxies. For [OII]λ3727 emitters, the test finds a significant difference only in the bright bin ($p = 0.002$). This measurement for [OIII] supports previous studies that find line-emitters preferentially at intermediate distances around clusters (Darvish et al., 2014) at $z \sim 1$. We explore this result in more detail in §4.6.5.

4.6.3 Measuring Star Formation

Studying the R_7 distribution by itself gives insight into only the relationship between the locations of ELGs and of overdensities, while ignoring the other properties of the ELGs. With the flux catalog, we were also able to investigate how an ELG's environment might influence its emission line luminosity and recent star formation rate.

We calculated SFRs for the ELGs using the following equations:

$$\text{SFR}_{\text{H}\alpha}\ (M_\odot\ \text{yr}^{-1}) = 7.9 \times 10^{-42} L(\text{H}\alpha)\ (\text{erg s}^{-1}) \tag{4.4}$$

$$\text{SFR}_{[\text{OII}]}\ (M_\odot\ \text{yr}^{-1}) = 1.4 \pm 0.4 \times 10^{-41} L([\text{OII}])\ (\text{erg s}^{-1}) \tag{4.5}$$

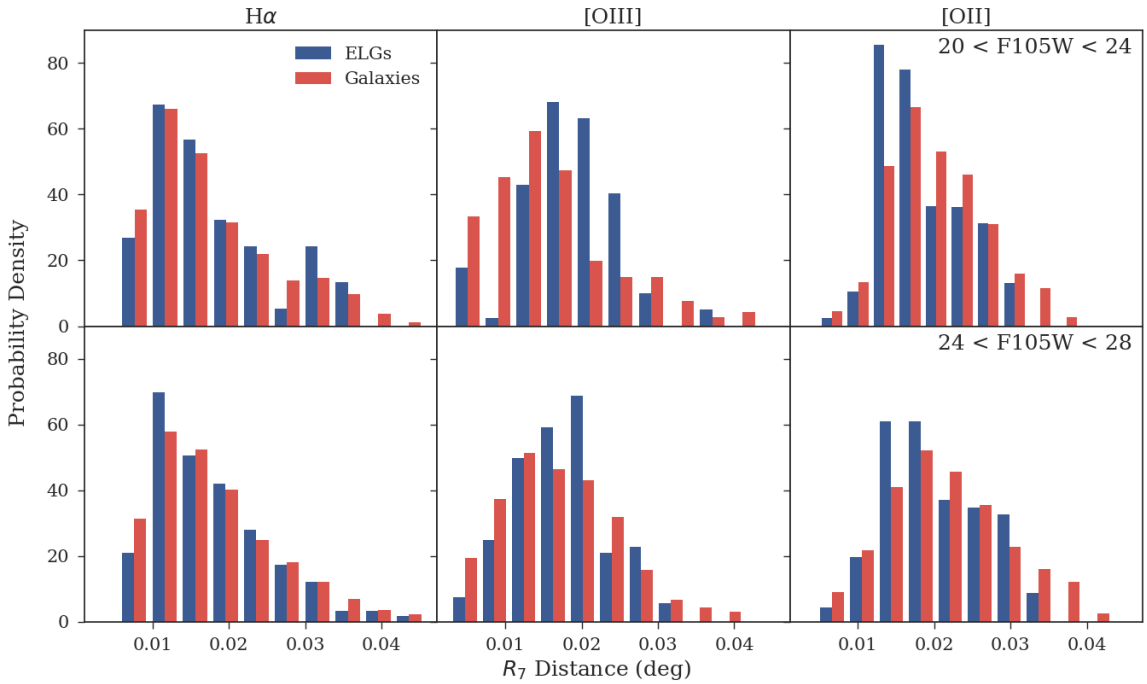

Figure 31: The probability density distributions of R_7 distances, separated into bins of redshift and F105W continuum magnitude, for ELGs (blue) and all galaxies (red) in a given magnitude-redshift bin. The first column uses $0.3 < z < 0.8$, corresponding to Hα emission. The middle column uses $0.8 < z < 1.3$ ([OIII]$\lambda\lambda 4959, 5007$), and the right column uses $1.3 < z < 2.1$ ([OII]$\lambda 3727$). The top row compares ELGs and galaxies with $20 < F105W < 24$ mag (bright). The bottom row compares ELGs and galaxies with $24 < F105W < 28$ mag (faint). For each distribution pair, we applied a two-sample K-S test to determine whether the distributions differed significantly. Both the bright and the faint Hα distributions are indistinguishable from the distributions of galaxies. The distributions of the [OIII]$\lambda\lambda 4959, 5007$ emitters do differ significantly ($p = 3 \cdot 10^{-7}$ for the bright distribution, $p = 0.02$ for the faint), with the [OIII]$\lambda\lambda 4959, 5007$ emitters found preferentially at middling R_7 values as opposed to low R_7. The [OII]$\lambda 3727$ distribution differs significantly only in the bright sample (p$= 0.02$).

$$\text{SFR}_{[\text{OIII}]}\ (M_\odot\ \text{yr}^{-1}) = 6.4 \pm 4.0 \times 10^{-42} L([\text{OIII}])\ (\text{erg s}^{-1}) \tag{4.6}$$

Equations 4.4 and 4.5 are calibrations from Kennicutt (1998), derived with a Salpeter IMF. Equation 4.6 was derived by Straughn et al. (2009) using [OIII]-Hα ratios from star-forming galaxy knots where both emission lines were present.

To account for the effects of dust extinction in measuring the SFR, we used a dust calibration developed by Sobral et al. (2012) using rest-frame *u*-*z* colors. The calibration was developed and tested using Hα and [OII] emitters at $z = 0.1$ and $z = 1.47$. It is given by

$$A_{\text{H}\alpha} = -0.092(u-z)^3 + 0.671(u-z)^2 - 0.952(u-z) + 0.875 \tag{4.7}$$

Sobral et al. (2012) find that this relation holds across redshift epochs, covering most of the redshift range of our sample and for both kinds of emitters. To convert the $A_{\text{H}\alpha}$ calculation to $A_{[OIII]}$ and $A_{[OII]}$, we applied the Calzetti et al. (2000) reddening law. For the few objects for which one of rest-frame *u* or *z* was unavailable, we assigned the median reddening value from the rest of the sample.

4.6.4 Environment and the SSFR-Mass Relation

We obtained stellar masses for our ELG sample by applying our EAZY SED catalogs to the SED fitting code FAST (Kriek et al., 2009). We checked the results for the GS1 field against the GOODS-South catalogs compiled by Santini et al. (2015), which largely exclude our GS2 parallel field. For the galaxies with existing measurements, we found our mass results consistent with the Santini et al. (2015) catalogs, with a median difference of less than 0.1 dex.

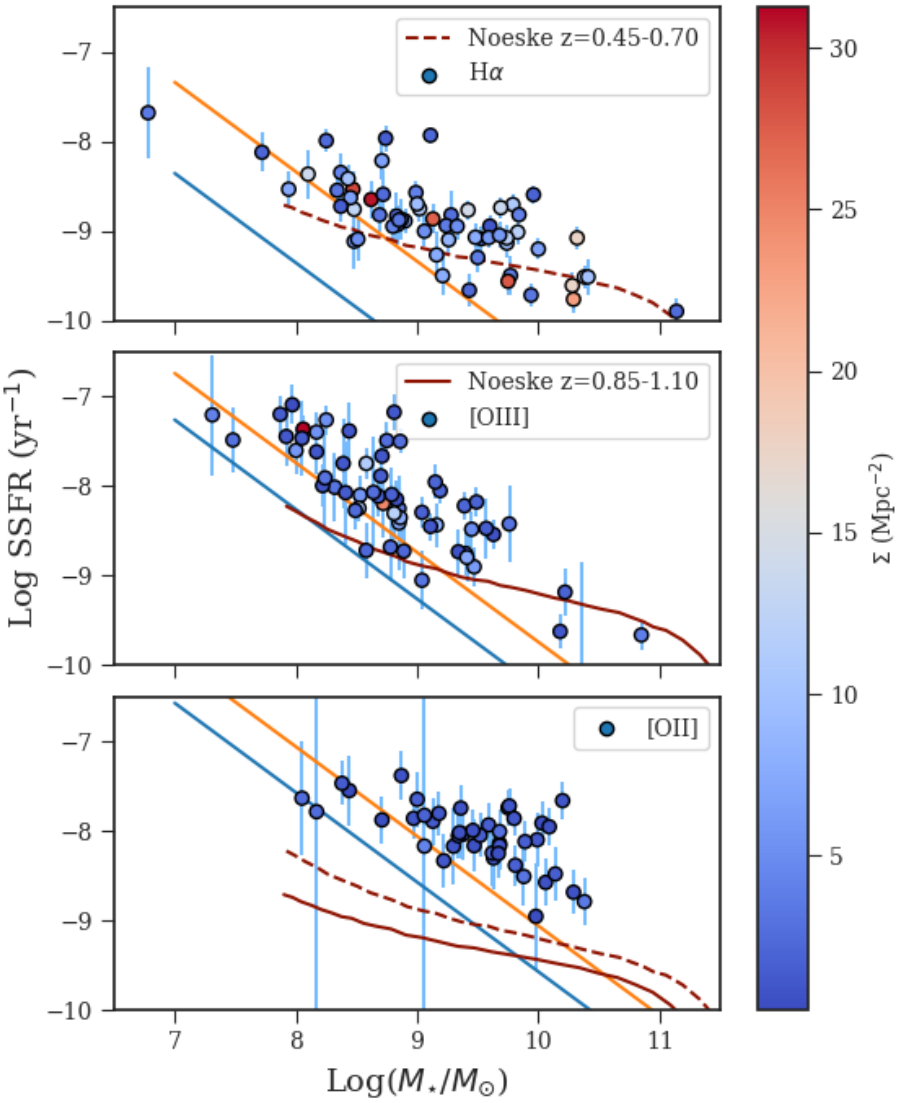

Figure 32: The specific star formation rate (SSFR) as a function of the stellar mass. The ELGs are given by colored circles (Hα, top panel; [O III]$\lambda\lambda 4959, 5007$, middle; [OII]$\lambda 3727$, bottom), and are shaded by their value of Σ, the local density of galaxies (see §sec:l-sig for description). Each panel also shows two lines of completeness (blue and orange solid lines), derived from the limiting line flux we measured (see Figure 29), and the minimum and maximum possible redshifts for each line. There is no clear trend between Σ and a galaxy's position on the SSFR-mass relation. The red curves (solid and dash) are the best-fit staged-tau models from Noeske et al. (2007). Our ELGs typically sit at higher SSFR for a given stellar mass compared to the models at comparable redshift, but this is likely due to the flux limitations of our sample.

With the stellar masses calculated, we were able to determine each ELG's SFR per stellar mass, or specific star formation rate (SSFR). The SSFR as a function of stellar mass is typically called the galaxy main sequence, and it suggests an evolution of star formation with redshift and stellar mass (Noeske et al., 2007). In star forming galaxies, as redshift decreases, ongoing star formation builds up increased stellar mass, and as this happens SSFRs decline as the galaxies exhaust their supplies of gas.

This smooth relation doesn't account for cases of rapid quenching, and does not address the influence of environment on how galaxies evolve. In Figure 32, we show the SSFR as a function of the stellar mass, and compare our ELGs to the results from Noeske et al. (2007), who measured this in four redshift bins up to $z = 1.1$. We show the best-fit staged-tau models of star formation history from Noeske et al. (2007) in the redshift bins most closely matching our Hα and [OIII] emitters (the [OII] sample is at too high a redshift), and find that our ELGs typically have higher SSFR for a given stellar mass.

However, we also estimated our lower-bound SSFR based on the limiting line flux of our catalog. Since the limiting luminosity is redshift dependent, we determined the lower-bound SSFR based on the lower and upper redshift limits of each ELG sample. We show these lines in Figure 32. They generally correspond to the elevated SSFRs of our ELGs, especially for [OII] and the lower-mass [OIII], indicating that we are likely sampling the upper region of the galaxy main sequence.

We were still able to investigate the possible environmental effects on the main sequence, especially for Hα, where we probe the main sequence most closely. In Figure 32, we also show each galaxy's local surface density Σ. There is no significant relationship between either Σ and the stellar mass or Σ and position on the SSFR-mass relation to the densities probed, which get only as dense as galaxy groups. The same holds for the ELGs' R_7 measurements. This suggests that environmental effects do not play a systematic role in

either quenching or triggering star formation, since they do not appear to disrupt the smooth star formation relation of the main sequence.

4.6.5 Line Luminosity and Clustering

We also studied the relationship between emission line strength and galaxy clustering more directly. First, we used the galaxies' redshifts and angular separations to compute the local physical surface density Σ in units of Mpc^{-2} for each ELG. Then, we split the sample of ELGs into two subsamples: those located in a redshift slice where a significant overdensity is detected ("In OD"), and those in a redshift slice with no detection ("No OD"). This result can be seen in Figure 33, which shows the line luminosity as a function of Σ for Hα, [OIII], and [OII] emitters. In each panel, the horizontal dashed lines give the median line luminosity for each subsample, and the vertical dashed lines give the median Σ. We measured SFR-Σ and SSFR-Σ relations as well, and the shape of the relation remained essentially unchanged for each emitter. Thus, for this discussion we will refer simply to the L-Σ relation shown in Figure 33, as that requires the fewest additional assumptions.

The Hα L-Σ distribution (top panel) shows little indication of a preferred relationship with density. Even in the OD slices, Hα emitters are found at a range of local densities, and with a range of luminosity values. The median luminosity for emitters near overdensities is 0.3 dex higher than for those in non-OD slices, which is about twice the typical error size for the Hα emitters. We compared the derived Hα SFRs from this luminosity sample to a narrowband-selected sample of star-forming (SFR $> 3M_{\odot}$ yr^{-1}) Hα emitters at $z = 0.845$ (Sobral et al., 2011), using the same SFR diagnostic. Our distribution differs from the result in Sobral et al. (2011), which shows SFR increasing with density up to $\Sigma \sim 50$ Mpc^{-2}. The discrepancy may be at least partially explained by their selection of SFR $> 3M_{\odot}$ yr^{-1}

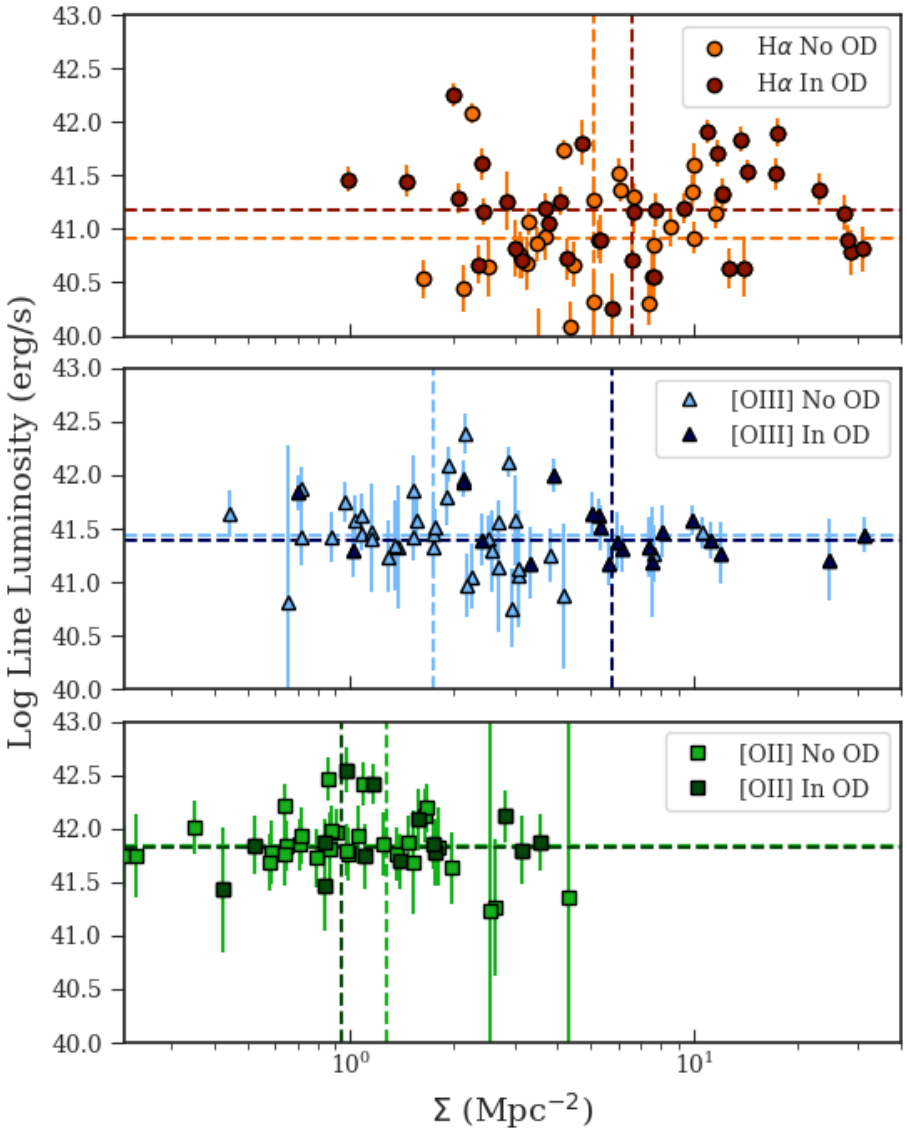

Figure 33: The line luminosity as a function of surface density for ELGs located in a redshift slice with a significant overdensity detection. The ELGs are given by orange circles (Hα, top panel), blue triangles ([OIII]$\lambda\lambda 4959, 5007$, middle), and green Xs ([OII]$\lambda 3727$, bottom). Each panel contains two subsamples: emitters found in redshift slices without a significant overdensity detection ("No OD"; lighter colors), and emitters found in slices with a significant detection ("In OD"; darker colors). The median luminosity and Σ values for each subsample are given by the horizontal and vertical dashed lines. This shows a substantial difference in the locations of [OIII] emitters depending on the proximity of an overdensity: in redshift slices with an overdensity, the [OIII] emitters are much more likely to be found at densities corresponding to group outskirts.

emitters, which would exclude most of our sample, and the availability of Hα-bright sources in their narrowband selection. Darvish et al. (2014) conducted a similar study down to a limit of SFR $> 1.5 M_{\odot}$ yr^{-1}, and finds only a small difference in median SFR between field and cluster galaxies. However, Darvish et al. (2014) also find that at intermediate densities, a higher fraction of galaxies exhibit star formation compared to fields and rich clusters.

Difference in redshift could provide further explanation. Grützbauch et al. (2011) found a weak correlation between overdensity and *U-B* color (as a proxy for star formation). Their study showed declining star formation with increasing density at $0.4 \leq z \leq 0.7$, roughly matching the redshift range of our Hα emitters, which becomes a flat relation for $0.85 \leq z \leq 1$. The result of Grützbauch et al. (2011) was limited to stellar masses down to only $\log(M_{\star}/M_{\odot}) > 10.25$, so they may not have detected the low-luminosity scatter we observe at low Σ, while observing a decline in high SFR as Σ increases. Scoville et al. (2013) studied NUV-continuum-derived SFRs versus density in redshift slices up to $z < 3$ in COSMOS, finding a flat SFR-Σ relationship for $0.8 < z < 2$. At lower redshift, they measure a flat relationship up to Σ of a few, after which the SFR declines with increasing density, with a stronger decline in lower redshift bins. These findings, combined with the results of Sobral et al. (2011); Darvish et al. (2014), suggests a transition period from peak star formation and merger interactions at $z \sim 2$ (Madau & Dickinson, 2014) to the local universe. After the merger peak, higher-density environments may have already quenched star formation in local galaxies through strangulation or ram-pressure stripping (Muzzin et al., 2012, 2014), depleting their reserves of star-forming material and increasingly relegating star formation to intermediate and field densities.

The [OIII]$\lambda\lambda 4959, 5007$ L-Σ distribution (middle panel) shows an essentially flat relationship, with high scatter at the lowest densities. In slices with an overdensity, the emitters we find are much more likely to occupy densities in the range $5 < \Sigma < 15$, with 12 out

of 20 emitters in OD slices found in this region. The median Σ is a factor of a few higher for [OIII] emitters in overdensity slices compared to those not near overdensities. This is distinct from the Hα emitters, which don't seem to have a distinct density preference when near overdensities.

The density where the [OIII] emitters are preferentially located corresponds to the rich fields and galaxy groups at the outskirts of a denser cluster, corroborating what we see in Figure 31. This result also matches the findings in Grützbauch et al. (2011), as we find a flat SFR-density relationship at $0.8 < z < 1.3$. We do not see the higher SFR at intermediate density that Darvish et al. (2014) measured, but our results do corroborate their finding of a higher fraction of star-forming galaxies at those densities. Compared to the Hα distribution, which shows emitters at all density ranges near overdensities, this could suggest an evolution with redshift in the preferred locations of star forming galaxies near overdensities.

The [OII]λ3727 SFR-Σ distribution (bottom panel) shows no relationship, with all the emitters found at low Σ. This is likely due in part to the limits of our overdensity search near $z \sim 2$, where our sample of fainter galaxies is less complete (see §4.6.4 for further discussion). One can see this effect in the range of SFRs calculated for the [OII] emitters, which is restricted to much higher star formation than the other two samples. Of the 24 overdensity candidates, only 4 are in the redshift range where we might find [OII], and these are of lesser significance and based on fewer galaxies compared to the overdensity candidates at lower redshift. These caveats aside, this could suggest that at higher redshift, field galaxies exhibit higher star formation, at least among the brightest galaxies. Patel et al. (2009) found in a study of $z \sim 0.8$ galaxies with $\log(M_\star/M_\odot) > 10$ that specific star formation (SFR per stellar mass) declined with increasing density. Since the limits of our completeness at this redshift selects more massive galaxies, this could indeed explain our findings.

4.6.6 Line Emission and Galaxy Pairs

We also investigated the behavior of ELGs with close companion galaxies, in order to study overdensities and environmental effects on a smaller scale. If nebular emission and related star formation are triggered by interactions with companion galaxies (Kennicutt et al., 1987; Alonso et al., 2004), then we could observe a difference in the number of nearby galaxies between ELGs and galaxies. Ellison et al. (2010) studied the effects on environment of interacting galaxy pairs selected from SDSS DR4, finding a small increase in SSFR for the closest pairs at low Σ relative to both more distant pairs and pairs found at higher galaxy densities. Their distance criterion for identifying a pair required a projected distance of $R_p < 80 \times h_{70}^{-1}$ kpc between the two galaxies. Using this projected distance as the range for possible companions, we find that the fractions of ELGs (31%) and non-ELGs (32%) that form a near pair are essentially the same. Kocevski et al. (2012) used a much narrower allowable pair range (12 kpc) to search for interactions near AGN hosts. Applying this much stricter cut yields a 3% pair rate in both ELGs and non-ELGs, suggesting that line emission and star formation are not necessarily directly connected to the presence of a nearby companion.

4.7 Conclusions

In this paper, we used deep NIR slitless spectroscopy to conduct an automated search for emission line galaxies. Using our continuum-subtracted peak-finding technique, we detected and identified 208 Hα6563, [OIII]$\lambda\lambda$4959,5007, and [OII]λ3727 emitters in the four FIGS

fields. For these emitters, we provide a robust catalog with integrated line fluxes, flux errors, line-derived redshifts, and observed equivalent widths. We measure line fluxes down to 10^{-17} erg cm^{-2} s^{-1} for objects with continuum magnitudes up to F105W < 28 mag.

We use the flux catalog to derive SFRs and the local surface densities of galaxies, which we use to search for trends in the SFR-density relation. We find that [O III] emitters are preferentially found at intermediate densities in the outer regions of galaxy groups, as shown in Figure 31, corroborating a finding at similar redshifts. When placing our sample on the SSFR-mass relation, we find higher SSFR per stellar mass compared to other studies at comparable redshift, though this is largely explained by limits on measured line flux. We find that SFR has no significant dependence on increasing local galaxy surface density for $0.3 < z < 0.8$ Hα emitters and for $0.8 < z < 1.3$ [OIII] emitters, as shown in Figure 33. We find no indication that environment influences a galaxy's location in this relation. A study of close galaxy pairs finds that ELGs are not more or less likely to have a close companion than non-ELGs. We compare our results with other environment studies after the peak in cosmic star formation at $z \sim 2$ (Madau & Dickinson, 2014), which show a variety of possible relations across different redshifts. We suggest a redshift evolution in the preferred location of ELGs near overdensities, from a preference for the close outskirts of groups at $z \sim 1$ to no preference at $z \sim 0.5$.

Chapter 5

COMPARING TRACERS OF STAR FORMATION AT $Z < 0.8$

5.1 Abstract

We measure the dust-extinction-corrected $F_{H\alpha}/f_{FUV}$ ratio for 15 emission line galaxies (ELGs) from the Faint Infrared Grism Survey and for 49 “green pea" ELGs. We find that for this sample the ratio varies significantly from the predicted theoretical ratios derived from simple stellar population models. To explain this, we explore possible relationships between the $F_{H\alpha}/f_{FUV}$ ratio and other ELG properties. The most significant correlation is between the $F_{H\alpha}/f_{FUV}$ ratio and the observed [OIII]$\lambda\lambda 4959, 5007$/[OII]$\lambda\lambda 3727, 3729$ emission line ratio. We model the stellar and nebular emission of a young stellar population as it evolves over time, and find that the age of the population can explain both the correlation between the ratios and the variation in $F_{H\alpha}/f_{FUV}$ ratio observed in our sample.

5.2 Introduction

The history of star formation in galaxies is critical to understanding the development of the $z = 0$ universe, whose modern structure and elemental composition depends on past star formation to process circumgalactic gas into stars and heavier elements. Tracing recent star formation in a galaxy can provide information about its current stellar population, as well as helping to explain the origins of its other characteristics.

There are several commonly used methods for measuring a galaxy’s star formation rate (SFR), described in detail in Kennicutt (1998). These methods depend on identifying

spectral emission generated uniquely by young stars, so that their detection implies recent star formation. One method uses the strength of the hydrogen recombination line Hα6563, which is produced when interstellar gas ionized by high-energy photons from massive ($M > 10M_{\odot}$ stars recombines, effectively reprocessing the integrated stellar emission beyond the Lyman limit. The massive stars responsible for generating the necessary ionizing radiation have short lifetimes of < 20 Myr, so the detection of strong Hα emission implies that new star formation must have occurred within that timescale.

Recent star formation can also be measured from the UV continuum at wavelengths between 1250 and 2500 Å, where the photon production is dominated by somewhat less massive ($M > 3M_{\odot}$) stars with ~ 100 Myr lifespans. Assuming that galaxies have a constant star formation history over a long timescale, and that they have a consistent initial mass function (IMF), gas composition, and dust extinction, then the Hα and far-UV (FUV) calibrations should produce star formation rates at a predicted, fiducial ratio. Many recent studies, however, observe systematic variations in the Hα-FUV ratio (Meurer et al., 2009; Lee et al., 2009; Boselli et al., 2009; Weisz et al., 2012).

In this paper, we study the variation in the Hα-FUV ratio among a sample of $0.3 < z < 0.8$ Hα emitters identified via slitless grism spectroscopy in the Faint Infrared Grism Survey, and among a sample of $z < 0.4$ green pea galaxies. To do this, we study the ratio as a function of other nebular emission and galaxy properties, and then make use of photoionization modeling to test how these properties relate to the Hα-FUV ratio ratio and a galaxy's star formation history. In §5.3, we briefly describe the FIGS data collection and reduction, as well as our methods for emission line detection and measurement, and the ancillary data used. In §5.4, we describe our measurements of the Hα-FUV ratio and compare our results to previous studies. In §5.5, we search for significant correlations between the Hα-FUV ratio and other parameters. In §5.6, we use stellar population and

photoionization modeling to study how our observed correlations relate to an aging starburst. For this paper we will use $H_0 = 67.3$ km s^{-1} Mpc^{-1} and $\Omega_M = 0.315$, $\Omega_\Lambda = 0.685$ (Planck Collaboration et al., 2014). All magnitudes are given in the AB system (Oke & Gunn, 1983).

5.3 Survey and Observations

5.3.1 Spectra from the Faint Infrared Grism Survey

The Faint Infrared Grism Survey (FIGS, HST/Cycle 22, ID:13779, PI S. Malhotra) used the HST WFC3-G102 (see Figure 34) infrared grism to obtain deep slitless spectroscopy of $\sim$ 6000 galaxies. FIGS achieved 40-orbit depth in 4 fields, designated GN1, GN2, GS1 (UDF), and GS2 (HDF-PAR2). Objects in each field were observed in 5 different 8-orbit position angles (PAs) in order to mitigate contamination of the spectra by overlapping spectra from nearby objects. Each PA covers a 2.05'x2.27' field of view. In this paper we focus on results obtained in the GS1/HUDF field.

In this paper, we used 1D spectra which were generated using the methods described in Pirzkal et al. (2017). Here we briefly summarize this process. We reduced FIGS data in a manner that loosely follows the method used for GRAPES and PEARS, the previous deep HST grism surveys (Pirzkal et al., 2004; Xu et al., 2007; Rhoads et al., 2009; Straughn et al., 2009; Xia et al., 2012; Pirzkal et al., 2013). First, we generated a master catalog of sources from deep CANDELS survey mosaics in the F850LP filter in ACS and the F125W and F160W filters in WFC3 (approximately the z, J, and H bands; Grogin et al., 2011; Koekemoer et al., 2011). We astrometrically corrected the data to match the absolute astrometry of the GOODS V2.0 catalogs. We estimated the background levels of the grism observations by using a two-component model, which included a constant Zodiacal

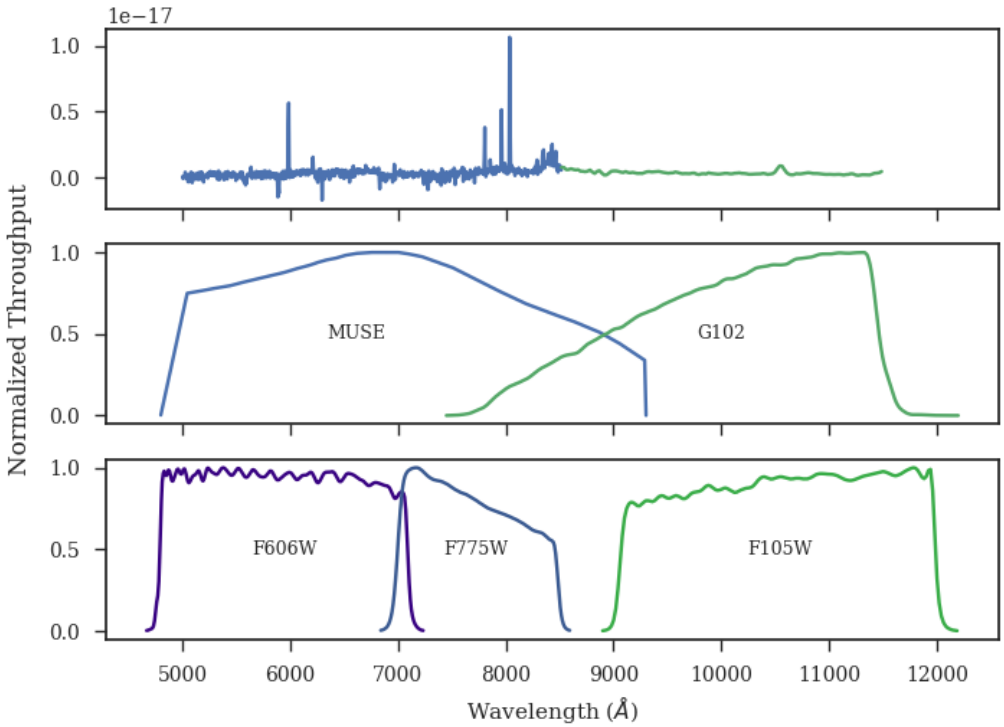

Figure 34: The top panel shows the spectrum of an example ELG from FIGS at z=0.885, with spectra from MUSE/VLT (blue) and the HST WFC3 G102 grism (green). The y-axis for this panel is F_λ. The middle panel gives the throughput curves for each spectrograph, normalized to the maximum throughput of each. The lower panel shows the throughput curves for HST photometric bands at comparable wavelengths. In this example, Hα+[NII] are detected in the FIGS G102 spectrum, and [OIII]$\lambda\lambda$4959,5007 and [OII]3727 are detected in MUSE/VLT.

light background as well as a varying He I light background. To generate the individual spectra, we used a Simulation Based Extraction (SBE) approach that accounts for spectral contamination from overlapping spectra, as well as allowing the use of an optimal extraction approach (Horne, 1986) when generating 1D spectra from 2D spectra. We refer the reader to Pirzkal et al. (2017) for a complete description of these processes. When the extractions were complete, we had an average of ~ 1700 spectra per field, with a typical 3σ continuum

detection limit of $m_{F105W} = 26$ mag and an emission line sensitivity of 10^{-17} erg cm^{-2} s^{-1}.

5.3.2 UV and Optical Data

We supplemented our infrared FIGS spectra with UV and optical data from other sources. We matched our FIGS objects with the UVUDF catalog (Rafelski et al., 2015) in order to obtain WFC3/UVIS F225W and F336W broadband photometry. The F225W measurements have a 5σ depth of 27.8 AB magnitudes, and the F336W measurements have a 5σ depth of 28.3 AB magnitudes, based on the limiting sky noise. The catalog photometry was already corrected for Galactic extinction.

For the GS1/HUDF FIGS field, we supplemented our infrared FIGS spectra with deep archival high-resolution optical IFU spectra taken with the Multi-Unit Spectroscopic Explorer (MUSE) instrument (Bacon et al., 2010) from the Very Large Telescope (VLT). This expands the available spectroscopic wavelength coverage considerably, enabling confirmation of detected emission lines in FIGS via the identification of complementary emission lines at optical wavelengths, even for many faint sources. We used the publicly available IFU spectra from the MUSE Hubble Ultra Deep Survey (Bacon et al., 2017), a mosaic of nine 1×1 arcmin^2 MUSE fields in the HUDF. In order to extract spectra for emission-line objects in our sample, we first used the known sky coordinates for each object in FIGS to find RA-Dec matches in the MUSE data. At each wavelength slice, we placed a 2 arcsecond aperture centered on the object, which we determined was able to capture the total flux from most line-emitting sources at the redshifts considered. Then, we generated 1-D spectra for the matched objects by summing up the flux within the aperture at each wavelength, across the entire MUSE wavelength range (see Figure 34 for the MUSE wavelength coverage compared to WFC3 G102). This produced a catalog of extracted FIGS

candidate spectra from the reduced MUSE datacube. The MUSE data wavelength coverage extends from 4752 Å to 9347 Å with a spectral resolution of 2.3 Å, though the sensitivity begins to drop off at wavelengths lower than 5000 Å and at wavelengths higher than 9200 Å noise from sky emission begins to dominate, so we restrict our usage of the MUSE spectra to between these wavelengths. MUSE has a 3σ line sensitivity of $\sim 3 \cdot 10^{-19}$ erg cm^{-2} s^{-1}, and thus should detect lines of strength comparable to or even considerably less than the lines found in FIGS G102 spectra.

5.3.3 Emission Line Measurement

We identified our sample of Hα galaxies from a systematic search of the FIGS spectra for emission line galaxies (ELGs). We conducted the search with an algorithm to find significant peaks from continuum-subtracted spectra, and then we identified and confirmed individual emission sources through a combination of visual inspection, spectroscopic and photometric redshift matching, and the identification of pairs of emission lines. The line fluxes were then estimated via a combined Gaussian fit to the line and a power-law fit to the continuum. To get the flux error, we first estimated the error of the flux of each pixel from the standard deviation in the flux of the nearby continuum pixels. Then we propagated these errors with the line fit to produce the total error for the integrated line flux. We used the best-fit line centroid to derive precise redshifts for the ELGs. Further details on the line selection and fitting process can be found in Pharo et al. (2019).

For the sample of FIGS Hα emitters, we measured the fluxes of their [OIII] and [OII] line emission using the matching MUSE spectra described in §2.2. We used a similar procedure to that used with the G102 spectra, with the initial line centers predicted by the Hα line fits. As the MUSE spectra have a much higher resolution, the [OIII] and [OII] line fits could

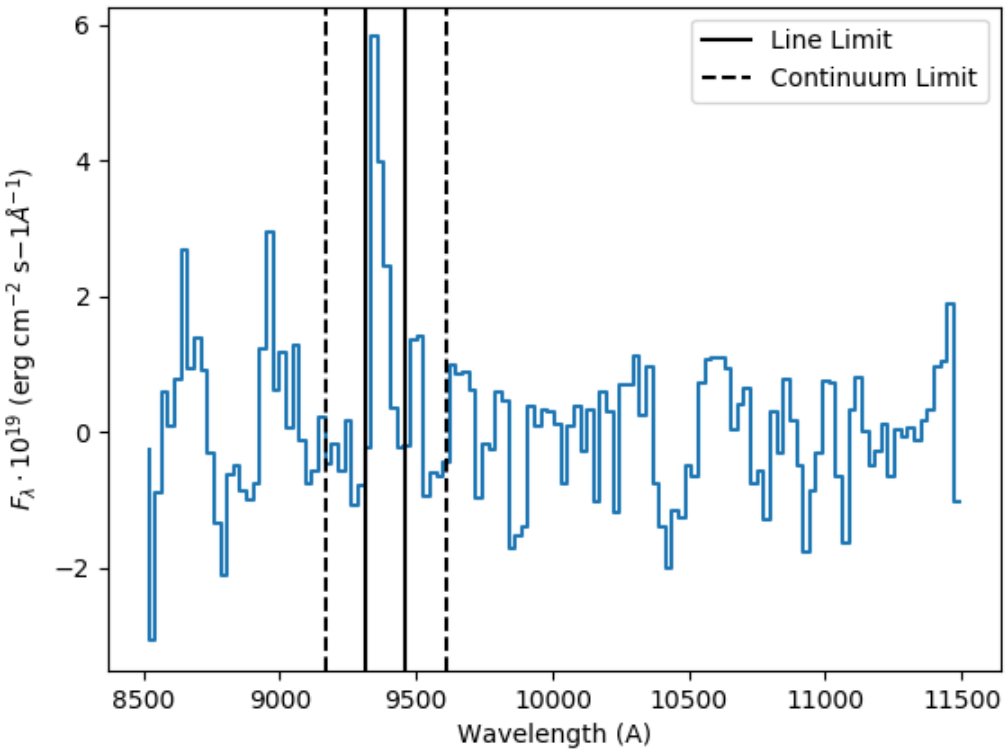

Figure 35: An example of the line-finding routine. This plot shows the continuum-subtracted flux for one PA of FIGS object GS1-2375. This shows an iteration of the line-finding routine when centered at 9388 Å. The routine sums the flux of the pixels within the solid black lines, which is considered to be the candidate line flux. Then, the continuum flux is estimated from the median flux of the pixels between the solid and dashed lines. This continuum is subtracted from the line flux, and the S/N is calculated.

refine the redshift measurement further. Flux calibration between the MUSE and FIGS spectra found that, for an emission line found in both spectra, the fluxes measured were generally in agreement within the derived line flux errors. The flux calibration is discussed in detail in Pharo et al. (2019).

5.3.4 Green Pea Sample

To augment our sample of FIGS ELGs, we turned to a catalog of 1004 so-called "green pea" galaxies. Green pea galaxies are so named for their green color and compact, unresolved shapes in composite *gri* images from the Sloan Digital Sky Survey (SDSS; Cardamone et al., 2009). This catalog selection is described in detail in Jiang et al. (2019), but the most important criterion for these results is the selection for strong [OIII]5007 and Hβ line emission in the SDSS optical spectra, so we could expect the objects to have well-measured Hα, O[III]5007, and O[II]3727 fluxes, among other optical lines.

The green peas have lower redshifts than the FIGS galaxies, with a median of $z = 0.129$ in the whole sample. Because of this, we needed to use UV data to obtain rest-frame FUV measurements. We matched this catalog with *Galaxy Evolution Explorer* (GALEX) FUV and NUV photometry (Morrissey et al., 2007), obtaining a final green pea sample of 49 ELGs with good FUV and NUV measurements, both of which are required to obtain the UV reddening through the FUV-NUV slope.

Because the green peas have emission lines with such high equivalent widths, the Hα flux is likely to dominate the R-band flux measurement. In order to obtain a measure for just the R-band continuum flux density, we divided the integrated Hα line flux by the Hα equivalent width. We measured their half-light radii from HST NUV imaging.

5.3.5 Extinction and Flux Corrections

For both the FIGS ELGS and the green peas, we estimated the internal dust extinction in the UV using the known relation between extinction and FUV-NUV color (Meurer et al., 1999). For all of the green peas and for most of the FIGS ELGS, we measured and corrected

for the optical extinction at Hα using the Balmer Decrement, measured from the observed ratio of the Hα line to Hβ. We were unable to obtain a measurement of Hβ for five of the FIGS ELGs, so for these we used the extinction measured with the FUV-NUV color and the dust extinction law from (Calzetti et al., 2000) to estimate the optical reddening.

Because of the low resolution of the FIGS spectra, the Hα emission line is blended with the nearby [NII]$\lambda\lambda$6548,6584 emission lines. If these emission line have fluxes of an appreciable fraction of the true Hα line strength, then they will inflate the Hα flux that we measure from the line fit. This could cause an overestimation of the star formation rate and other properties dependent on the Hα line flux, so we sought to correct for this contamination. Faisst et al. (2018) produced an empirical parameterization of the [NII]/Hα flux ratio for galaxies with $0 < z < 2.7$ and $8.5 < \log(M_\star/M_\odot) < 11.0$ as a function of redshift and stellar mass. We obtained stellar masses for our Hα emitters from Sanders et al. (2015), and thus were able to use the Faisst parameterization to estimate the [NII]/Hα flux ratio. A few of our objects actually have lower stellar masses than were considered by Faisst et al., but the [NII]/Hα flux ratio trends toward 0 as the stellar mass gets low. Faisst et al. give [NII]/H$\alpha = 0.04 - 0.07$ for the lowest mass bin, so we simply assume a fraction of 0.05 for the lowest mass objects, the effect of which is small. With the [NII]$\lambda\lambda$6548,6584 fractions estimated, we removed the estimated amount from the measured Hα flux, thereby deriving the "true" $H\alpha$ flux. The green pea emission lines we obtained with higher-resolution SDSS spectroscopy in which the nearby [NII] emission lines were resolved and separately measured, so they do not contaminate the green pea Hα measurements.

5.4 The Hα-FUV Ratio

5.4.1 Tracers of Star Formation

Meurer et al. (2009) defined a fiducial stellar population model with an IMF power-law slope given by $\gamma = -2.35$ and upper stellar mass limit of $M_u = 100 M_\odot$. Using the SFR calibrations from Kennicutt (1998) for Hα- and FUV-derived SFRs, Meurer et al. (2009) derived a fiducial flux ratio of

$$\frac{F_{\mathrm{H}\alpha}}{f_{\mathrm{FUV}}} = 11.3 \tag{5.1}$$

with the UV calibration transformed to the pivot wavelength of the GALEX FUV filter.

5.4.2 Trends with Surface Brightness

Following the procedure in Meurer et al. (2009), we studied the distribution of $H\alpha$/FUV ratios as functions of the $H\alpha$ surface brightness and the R-band surface brightness, which we approximate for FIGS objects by calculating the F105W surface brightness. We determine the surface brightness by the calculation

$$\Sigma = \frac{F \cdot (1+z)^4}{2\pi r_{50}^2} \tag{5.2}$$

where we have applied a redshift correction to better compare brightnesses to the $z = 0$ objects described in Meurer et al. (2009). For this we use the redshifts derived from the centroid of the emission line fit. Here F refers to either $F_{H\alpha}$, the integrated $H\alpha$ emission

line flux, or f_λ, the F105W flux density. In the case of f_λ, we applied an extra factor of $(1+z)$ to account for bandpass shift. The term r_{50} refers to the radius at which 50% of the flux is contained.

The results are plotted in Figure 36. We see a similar correlation to that found in Meurer et al. (2009) for the $H\alpha$ surface brightness, but this is to be expected since both the surface brightness and the ratio are proportional to the integrated $H\alpha$ line flux. We do not, however, observe the same correlation in the R-band surface brightness.

Figure 37 shows the same Hα-FUV versus R-band surface brightness relation, focused on the region occupied by the FIGS objects, shown in red. This figure also shows the results from Weisz et al. (2012), which show a weaker correlation with the R-band surface brightness than in Meurer et al. (2009), with high scatter among the low-surface-brightness galaxies, and the galaxies with higher surface brightness trending toward the fiducial ratio.

To expand the number of new objects with which we could study the Hα-FUV ratio, we added the sample of Green Pea galaxies described in §2.5. These are shown in Figure 37 as well. They typically have a high Hα-FUV ratio, sitting almost entirely above the fiducial ratio. The green peas largely correspond to the 1σ confines of the fit from Meurer et al. (2009), but they do not show as strong a correlation with the R-band surface brightness. The combined samples follow the R-band surface brightness correlation, though with large variation, particularly as the low-surface-brightness end.

5.5 Correlations with Other Properties

We sought further explanation for the Hα-FUV ratio variation by measuring the ratio's correlation with other galaxy properties. With the addition of the MUSE/VLT spectra, we

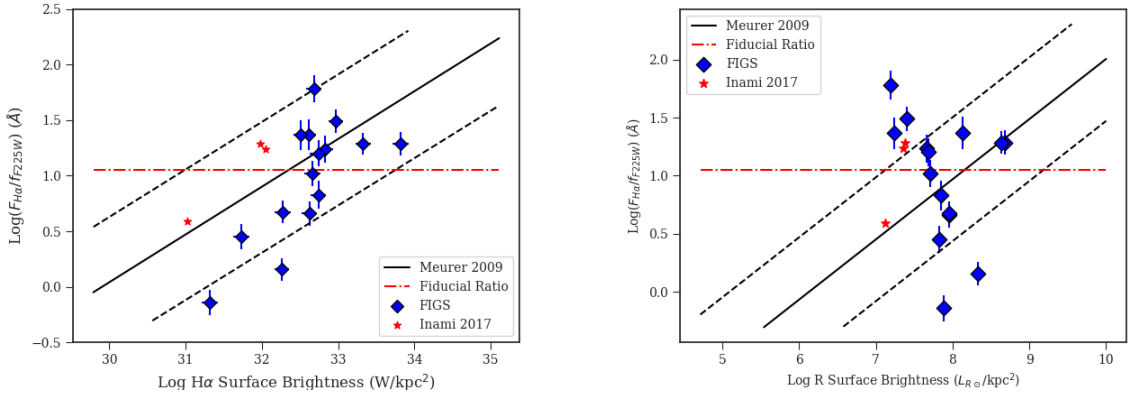

Figure 36: The $H\alpha$-FUV ratio as a function of the Hα surface brightness (left) and the R-band surface brightness (right). FIGS points are given by blue diamonds. The solid black line shows the fit from Meurer et al. (2009), with the 1σ fit limits given by the dashed black lines. The fiducial ratio as described in Equation 5.2 is shown by the red dot-dash line. Three Hα emitters from Inami et al. (2017) are shown as red stars. Our sample includes significant deviation around the predicted fiducial ratio, but does not reproduce the same R-band correlation observed by Meurer et al. (2009).

were able to measure the [OIII]$\lambda\lambda$4959,5007 and [OII]$\lambda\lambda$3727,3729 emission lines for FIGS galaxies. The green peas, initially selected for strong [OIII] emission, had measurable oxygen lines as well. This let us measure the ratio

$$O3O2 = \log([OIII]\lambda\lambda 4959, 5007) - \log([OII]\lambda\lambda 3727, 3729), \tag{5.3}$$

a common proxy for the ionization state of a galaxy's nebular gas (Kewley & Dopita, 2002).

With the Hα emission lines, we were able to obtain Hα equivalent widths and star formation rates derived from the Kennicutt (1998) calibration. Using stellar masses derived from CANDELS catalogs collected in Sanders et al. (2015), we converted the SFRs into star formation per stellar mass, or specific star formation rate (SSFR). We then checked for a relationship between the Hα-FUV ratio and these quantities.

Figure 38 shows the Hα-FUV ratio as a function of (clockwise from top left) redshift, O3O2, Hα EW, and Hα-derived SSFR. For each relation, we computed the Spearman rank

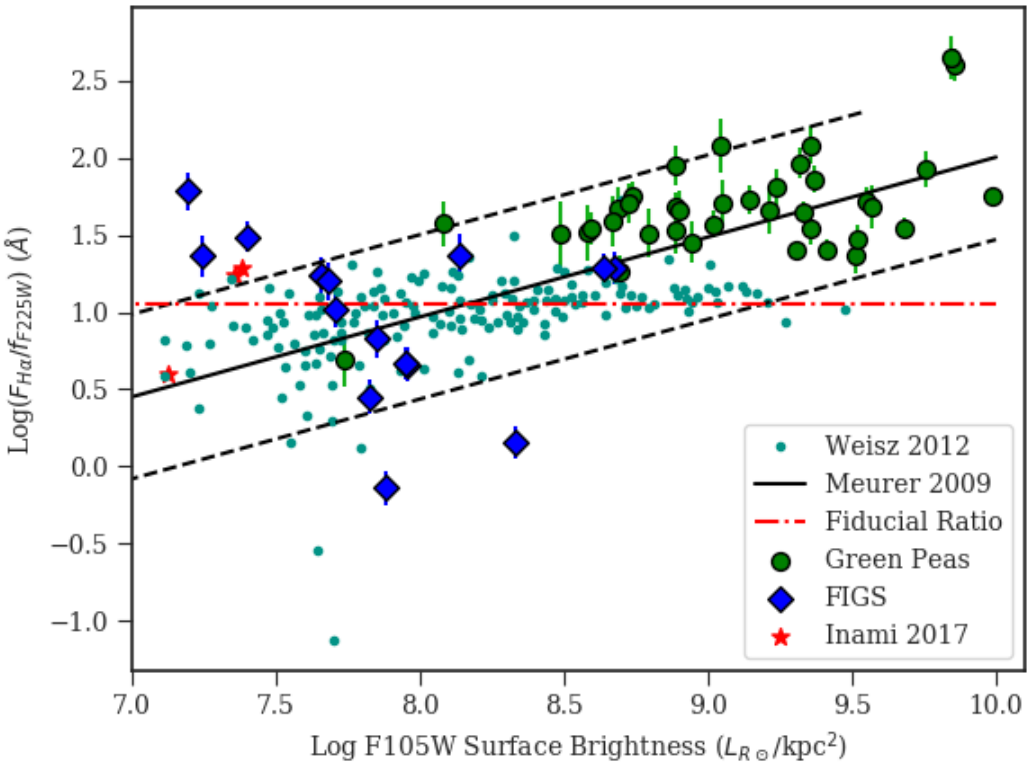

Figure 37: The $H\alpha$-FUV ratio as a function of the R-band surface brightness, corrected for dust and redshift dimming. The FIGS points are blue diamonds, and the green pea sample is shown as large green circles. The solid black line is the fit from Meurer et al. (2009), with the 1σ fit limits given by the dashed black lines. The fiducial value of the $H\alpha$-FUV ratio is shown by the red dot-dash line. The small blue circles are taken from Weisz et al. (2012), and the red stars are the emitters from Inami et al. (2017).

correlation coefficient, a method of testing for monotonic correlation between two variables. The Spearman coefficient r can range from -1 (a perfectly monotonic negative correlation) to 1 (a perfectly monotonic positive correlation), with 0 corresponding to no measurable correlation. The r value for each pair of quantities is given in a bottom corner of each panel in Figure 38. We also provide p, the probability of the null hypothesis that $r = 0$.

We measure a significant negative correlation between the Hα-FUV ratio and the redshift. This can be explained entirely as a selection effect. The green peas, selected for strong,

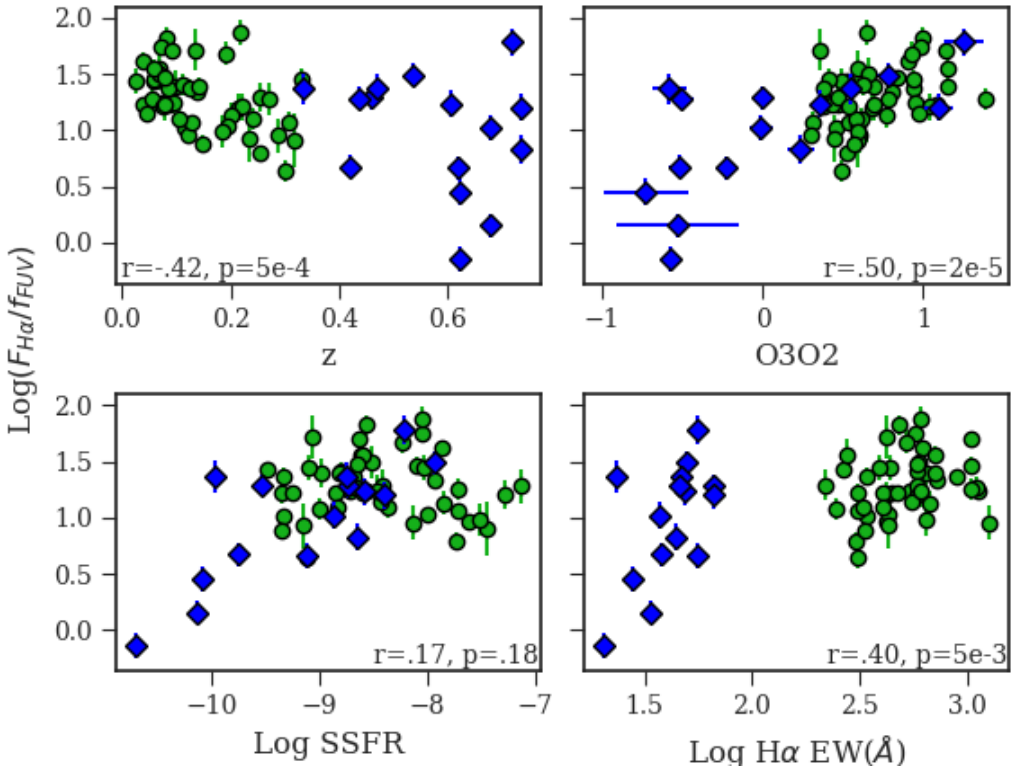

Figure 38: The Hα-FUV ratio as a function of different parameters. FIGS galaxies are shown as blue diamonds, and green peas are shown as green circles. In each panel, the Spearman correlation coefficient of the relation r is shown in a bottom corner, alongside p, the null hypothesis probability. A value of r close to 1 or -1 indicates a clear monotonic correlation, and a value of r close to 0 indicates no correlation.

high-EW line emission, are at a lower redshift than the FIGS sample. The FIGS sample alone has no significant correlation with redshift, and the green pea sample has only a weak one.

We find no correlation between the Hα-FUV ratio and the SSFR. This is mostly due to no observed dependence among the green peas, as a correlation with $p = 0.005$ can be found in the FIGS sample alone. We see a similar level of correlation with the Hα EW, though this trend is found in the green peas as well.

The strongest and most significant correlation (p =2e-5) is between the Hα-FUV ratio

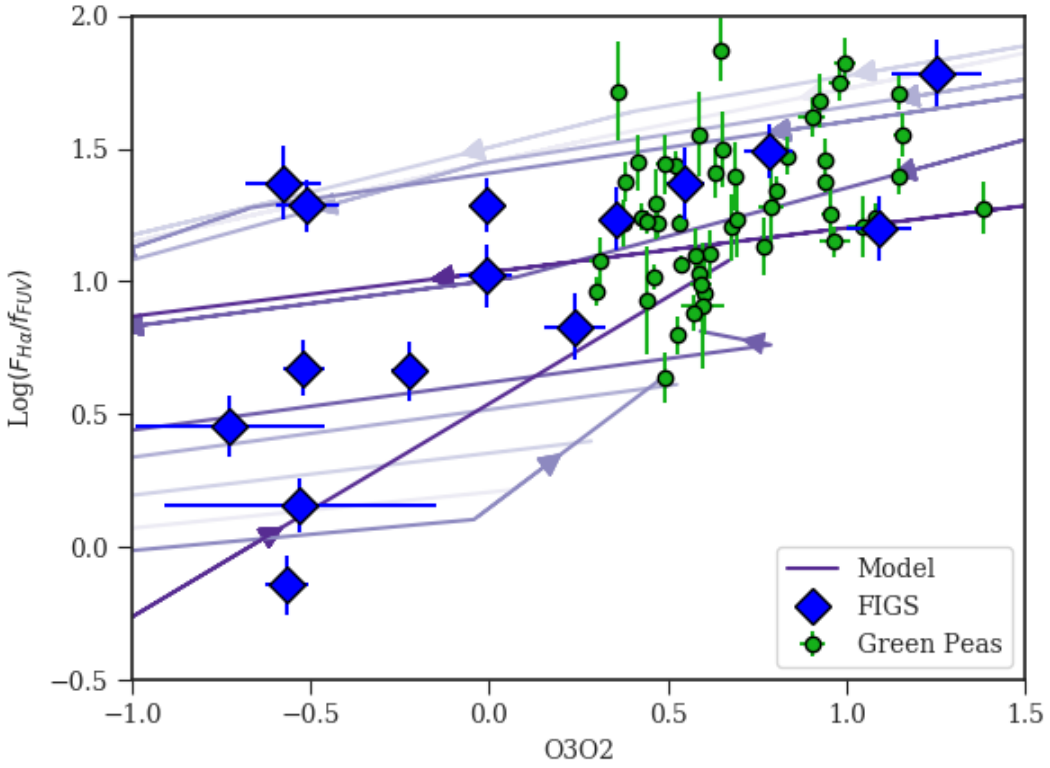

Figure 39: The Hα-FUV ratio of the FIGS and green pea samples as a function of O3O2. They are plotted over a series of photoionization models derived from CLOUDY using input stellar spectra from BPASS. Each line represents a model with a given metallicity (ranging from a mass fraction of $Z = 0.001$ to $Z = 0.04$, with $Z_{\odot} = 0.02$. The lowest Z is given by the lightest-shaded line, with metallicity increasing as the shade darkens. Each population model evolves with age of the stellar population, form an initial age of 10^6 years to 8×10^7 years. Arrows on the model lines show the direction of increasing age.

and O3O2, shown in the upper right panel. With $r = .50$, this relation is the closest to monotonic of those we've tested with our samples, and it doesn't rely on using the same Hα measurement to derive both relevant properties. Furthermore, we still find the correlation among each of the subsamples, albeit at a somewhat less significant level, with $r = 0.61$, $p = 0.016$ for the FIGS sample alone, and $r = 0.39$, $p = 0.005$ among the green peas.

5.6 Modeling a Simple Star Formation History

To explore the correlation between the Hα-FUV ratio and O3O2, we modeled the photoionization and nebular emission properties of a young simple stellar population. We used a library of stellar models from BPASS version 2.2.1 (Eldridge et al., 2017; Stanway & Eldridge, 2018), with an IMF upper slope of $\mu = -2.35$ and an upper stellar mass limit $M_u = 300 M_\odot$. We used models with a range of metallicities, defined by the metallicity mass fraction $Z = 0.001, 0.003, 0.006, 0.01, 0.02, 0.04$, where $Z_\odot = 0.02$. Each model is evolved from an initial age of 10^6 years to 10^{11} years. To investigate the young population, we selected models up to 10^8 years.

To obtain model nebular emission properties, we applied the BPASS stellar spectra to the CLOUDY photoionization code, version 17.01 (Ferland et al., 2017). We used a spherical cloud geometry as a distance of X parsecs from the stellar population, which combines with the luminosity of the incident spectrum to determine the ionization parameter. Then, using the gas composition and the shape of the stellar spectrum, CLOUDY calculates the ionization states of elements in the nebular cloud, and then produces a cloud emission spectrum. Combined with the emergent stellar radiation, CLOUDY produces a model of what an observed star forming cloud would look like. From this final spectrum, we took measurements of Hα, [OIII], and [OII] line emission, and we calculated a synthetic FUV flux from the emitted continuum. We checked the emission line luminosities as functions of age and metallicity with the results in Byler et al. (2017), and found our results consistent. We ran CLOUDY on stellar models with the range of metallicities and ages described above. The resulting evolution of the Hα-FUV ratio as a function of O3O2 is shown in Figure 39, alongside the observed FIGS galaxies and green peas.

The youngest stellar population, at 10^6 years, begins in the upper right quadrant of Figure

39, with both high Hα-FUV and high O3O2 ratios. As the population ages, the O3O2 ratio declines rapidly, and the Hα-FUV ratio declines more slowly, as the most massive stars begin to die, and the models move from the upper right to the upper left of the parameter space. These young ages cover most of the green peas, and the FIGS galaxies with Hα-FUV ratios elevated above the fiducial ratio. Next, the Hα-FUV ratio drops to the level of the fiducial ratio and then below, as the less massive stars that peak in the FUV continuum begin to dominate. For much of this period of stellar evolution, [OIII] emission is too low to be detectable, moving the models out of the range of our observed objects. As the population continues to age, and the less massive stars die out, the Hα-FUV ratio increases and begins to return to the fiducial level as the production of FUV continuum photons declines to match the previous decline in Hα.

As this happens, the O3O2 ratio also returns to values between -1 and 0. This places the models back in the lower left region of Figure 39, and covers the remaining FIGS objects. The age evolution can thus explain the FIGS and green pea observations in the Hα-FUV versus O3O2 plane. Variations in metallicity can account for the observed scatter, though variation in the ionization parameter can also explain this. As a result, the correlation between the Hα-FUV ratio and the O3O2 ratio can be seen as a function of the age of the starburst, so stellar population age can explain the deviations of observed Hα-FUV ratios from the theoretical fiducial ratio.

The behavior of the Hα-FUV ratio over the course of this burst is similar to that described in previous SFH models (Meurer et al., 2009; Weisz et al., 2012). These works show a similar cycling of Hα-FUV as the burst ages, varying with the duration of the burst and the level of underlying constant star formation. However, with the addition of the O3O2 parameter, we are able to demonstrate that the observed variation in the Hα-FUV ratio can

also be explained as a simple function of age and metallicity.

5.7 Conclusion

We measure the dust-extinction-corrected $F_{H\alpha}/f_{FUV}$ ratio for 15 $0.3 < z < 0.8$ emission line galaxies (ELGs) from the Faint Infrared Grism Survey and for 49 “green pea" ELGs at lower redshift. We find that the FIGS objects do not exhibit the same correlation with rest-frame R-band surface brightness that is seen in other samples, but a combined sample from many studies still corresponds closely to the correlation found in (Meurer et al., 2009). We examine other properties of the ELGs for correlations with the $F_{H\alpha}/f_{FUV}$ ratio that might explain the observed variation. We find a significant correlation between the combined FIGS-GP sample $F_{H\alpha}/f_{FUV}$ ratios and the O3O2, and lesser but still significant correlations among the individual samples. By using BPASS stellar models and photoionization models from CLOUDY, we are able to demonstrate that the O3O2 ratio combined with the age and metallicity of the stellar population can explain the observed $F_{H\alpha}/f_{FUV}$ ratio variation in the FIGS sample.

Chapter 6

CONCLUSIONS

This dissertation consists of four studies of galaxies at $0 < z < 2$ using WFC3 G102 near-infrared spectra from the Faint Infrared Grism Survey. We used these spectra in combination with matching spectra and broadband photometry from other surveys to identify overdensities of galaxies and emission line galaxies among the FIGS sample. With the ELGs, we were able to measure gas-phase metallicities and star formation rates. By combining this with the list of overdensity candidates, we studied a possible relationship between line emission, star formation, and galaxy environments.

In Chapter 2, we combined FIGS spectra with broadband photometry in order to produce a catalog of spectrophotometric redshifts. By comparing the catalog with a set of accurate spectroscopic redshifts, we demonstrated that the addition of the grism spectra to the redshift fit reduced the median redshift error of the sample from 3% to 2%. With the improved accuracy of the SPZ catalog, we conducted a systematic search for overdensities of galaxies in the four FIGS fields. To do this, we iterated through overlapping redshift slices with a width of $\Delta z = 0.03 \times (1 + z_{min})$, where z_{min} is the lower redshift boundary of the slice.

In each redshift slice, we calculated an array of nearest-neighbor densities. Overdensity candidates were flagged by comparing nearest neighbor densities to the densities found in adjacent redshift slices and within the given slice, in order to search for significant density peaks. This method yielded 24 candidate overdensities, of which two corresponded to galaxy clusters identified in previous spectroscopic surveys, in GN1 at $z = 0.85$ and GS1 at $z = 1.84$.

In Chapter 3, we developed a method for identifying ELG candidates from continuum-

subtracted 1D FIGS spectra by using a peak-finding algorithm. We applied this method to the GS1/HUDF field, where we were able to take advantage of matching deep optical IFU spectra from VLT/MUSE to find complementary emission lines and thereby confirm our candidates. We identified 71 ELGs in GS1 this way, and we measured line fluxes and redshifts.

In the matching MUSE spectra, we identified 14 ELGs at $z \sim 0.5$ where we were able to get a significant measurement of the [OIII]$\lambda 4363$ auroral emission line. Along with measurements of the [OIII]$\lambda\lambda$4959,5007; [OII]$\lambda\lambda$3727,3729; and Hβ4861 lines, we used this line to derive T_e-based oxygen-to-hydrogen ratios, and thereby gas-phase metallicities, for these 14 objects. We placed these objects on the Mass-Metallicity Relation, and found that they had lower metallicity at given stellar mass than several surveys at comparable redshift, contradicting the notion that there is little to no metallicity evolution from $z \sim 1$ to $z = 0$. We used a new calibration between the T_e metallicity method and the R_{23} metallicity method, which relies only on the [OIII]$\lambda\lambda$4959,5007; [OII]$\lambda\lambda$3727,3729; and Hβ4861 lines, to add eight ELGs with R_{23} metallicities to the Mass-Metallicity relation, some of which showed the same low-metallicity offset.

We explored possible explanations for the observed offset, ruling out selection effects, redshift, and choice of Initial Mass Function as causes. We observed a correlation between higher SSFR and lower metallicity, suggesting that gas inflows or outflows related to recent star formation may be the reason for measuring such low metallicities in this redshift regime. By placing the FIGS ELGs on the Fundamental Plane of Metallicity, the inclusion of star formation reconciles all but the lowest-mass FIGS objects with the literature, demonstrating the need to continue to probe galaxies at $0 < z < 1$ to lower stellar masses.

In Chapter 4, we expanded the ELG search from Chapter 3 to all of the FIGS fields. In addition to the MUSE data used in Chapter 3, we also used matching G141 grism spectra

and a compilation of spectroscopic redshifts to confirm candidates. We obtained a final set of 208 Hα, [OIII]$\lambda\lambda$4959,5007, and [OII]$\lambda\lambda$3727,3729 emitters. We developed a catalog of these line identifications with line fluxes and errors, line-derived redshifts, and rest-frame equivalent widths.

By using the overdensity study from Chapter 2, we obtained 7th-nearest-neighbor (R_7) distances and calculated a local surface density of galaxies Σ for each FIGS galaxy. We compared R_7 distributions for ELGs and regular galaxies, and found a significant difference in the shapes of their distributions for $0.8 < z < 1.3$ [OIII] emitters, with the [OIII] emitters preferentially located at intermediate R_7 compared to other galaxies.

With the line fluxes and redshifts, we derived line luminosities and associated star formation rates for the ELGs. We calculated stellar masses from the redshift SED fits and placed the ELGs on the SSFR versus mass relation, commonly known as the galaxy main sequence. Our ELGs typically had higher SSFR for a given stellar mass than previous relations at comparable redshifts, but this is largely an effect of the lower limit on our emission line flux detection. We also used these properties to develop a luminosity-Σ relation for each of the strong line emitters. We found no significant correlation between the line luminosity of an ELG and its local surface density of galaxies, but we did find that [OIII] emitters in redshift slices with significant overdensities were more likely to have densities in the range $5 < \Sigma < 15$ Mpc^{-2}, corresponding to the rich fields and galaxy groups on the outskirts of overdensities. This corroborates other findings for star-forming galaxies at $z \sim 1$. Finally, we compared rates of close-pair detection for ELGs and non-ELGs, and found similar rates among the two.

In Chapter 5, we measured the flux ratio of two common tracers of star formation, the Hα line flux and the far-ultraviolet (FUV) continuum, for 15 FIGS galaxies. We compared the tracer ratio to those measured in previous surveys and found that we observed a wider

variation in the Hα-FUV ratio at a given R-band surface brightness compared to these other results. We added a sample of "green pea" line emitters with high Hα-FUV ratios, and found that these two samples combined with previous results do follow a correlation with R-band surface brightness, albeit with high scatter at the low-surface-brightness end.

To explain the high scatter, we searched for correlations with other line emission properties of ELGs, including the redshift, SSFR, Hα EW, and the O3O2 ratio. The O3O2 ratio proved to be the most significant correlation among the combined FIGS and green pea populations, with a significant correlation also measured in the single samples. We used BPASS stellar models and CLOUDY photoionization models to produce a model of a stellar population's Hα-FUV ratio versus O3O2 ratio as that population ages for a range of metallicities. This model was able to explain the correlation with O3O2 and the Hα-FUV ratio variation as a function of the age and metallicity of the stellar population.

REFERENCES

Aller, L. H., ed. 1984, Astrophysics and Space Science Library, Vol. 112, Physics of thermal gaseous nebulae

Alonso, M. S., Tissera, P. B., Coldwell, G., & Lambas, D. G. 2004, MNRAS, 352, 1081

Amorín, R., Fontana, A., Pérez-Montero, E., et al. 2017, Nature Astronomy, 1, 0052

Andrews, B. H., & Martini, P. 2013, ApJ, 765, 140

Ashby, M. L. N., Willner, S. P., Fazio, G. G., et al. 2013, ApJ, 769, 80

Atek, H., Malkan, M., McCarthy, P., et al. 2010, ApJ, 723, 104

Bacon, R., Accardo, M., Adjali, L., et al. 2010, in Society of Photo-Optical Instrumentation Engineers (SPIE) Conference Series, Vol. 7735, Ground-based and Airborne Instrumentation for Astronomy III, 773508

Bacon, R., Conseil, S., Mary, D., et al. 2017, A&A, 608, A1

Baldry, I. K., & Glazebrook, K. 2003, ApJ, 593, 258

Baldwin, J. A., Phillips, M. M., & Terlevich, R. 1981, PASP, 93, 5

Balestra, I., Mainieri, V., Popesso, P., et al. 2010, A&A, 512, A12

Balogh, M., Eke, V., Miller, C., et al. 2004, MNRAS, 348, 1355

Barger, A. J., Cowie, L. L., & Wang, W. H. 2008, ApJ, 689, 687

Benítez, N. 2000, ApJ, 536, 571

Blanton, M. R., & Roweis, S. 2007, AJ, 133, 734

Bolzonella, M., Miralles, J. M., & Pelló, R. 2000, A&A, 363, 476

Boroson, T. A., Salzer, J. J., & Trotter, A. 1993, ApJ, 412, 524

Boselli, A., Boissier, S., Cortese, L., et al. 2009, ApJ, 706, 1527

Bouwens, R. J., Illingworth, G. D., Oesch, P. A., et al. 2015, ApJ, 803, 34

Brammer, G. B., van Dokkum, P. G., & Coppi, P. 2008, ApJ, 686, 1503

Brammer, G. B., van Dokkum, P. G., Franx, M., et al. 2012, ApJS, 200, 13

Bruzual, G., & Charlot, S. 2003, MNRAS, 344, 1000

Byler, N., Dalcanton, J. J., Conroy, C., & Johnson, B. D. 2017, ApJ, 840, 44

Calzetti, D., Armus, L., Bohlin, R. C., et al. 2000, ApJ, 533, 682

Calzetti, D., Kinney, A. L., & Storchi-Bergmann, T. 1994, ApJ, 429, 582

Capak, P., Cowie, L. L., Hu, E. M., et al. 2004, AJ, 127, 180

Cardamone, C., Schawinski, K., Sarzi, M., et al. 2009, MNRAS, 399, 1191

Christensen, L., Richard, J., Hjorth, J., et al. 2012, MNRAS, 427, 1953

Conroy, C. 2013, ARA&A, 51, 393

Cooper, M. C., Newman, J. A., Weiner, B. J., et al. 2008, MNRAS, 383, 1058

Cooper, M. C., Aird, J. A., Coil, A. L., et al. 2011, ApJS, 193, 14

Cooper, M. C., Yan, R., Dickinson, M., et al. 2012, MNRAS, 425, 2116

Coughlin, A., Rhoads, J. E., Malhotra, S., et al. 2018, ApJ, 858, 96

Dahlen, T., Mobasher, B., Faber, S. M., et al. 2013, ApJ, 775, 93

Darvish, B., Sobral, D., Mobasher, B., et al. 2014, ApJ, 796, 51

Dawson, S., Stern, D., Bunker, A. J., Spinrad, H., & Dey, A. 2001, AJ, 122, 598

Dickinson, M., Giavalisco, M., & GOODS Team. 2003, in The Mass of Galaxies at Low and High Redshift, ed. R. Bender & A. Renzini, 324

Dopita, M. A., & Evans, I. N. 1986, ApJ, 307, 431

Dressler, A. 1980, ApJ, 236, 351

Elbaz, D., Daddi, E., Le Borgne, D., et al. 2007, A&A, 468, 33

Eldridge, J. J., Stanway, E. R., Xiao, L., et al. 2017, Publ. Astron. Soc. Aust., 34, e058

Ellison, S. L., Patton, D. R., Simard, L., & McConnachie, A. W. 2008, ApJ, 672, L107

Ellison, S. L., Patton, D. R., Simard, L., et al. 2010, MNRAS, 407, 1514

Erb, D. K., Shapley, A. E., Pettini, M., et al. 2006, ApJ, 644, 813

Erben, T., Schirmer, M., Dietrich, J. P., et al. 2005, Astronomische Nachrichten, 326, 432

Faisst, A. L., Masters, D., Wang, Y., et al. 2018, ApJ, 855, 132

Ferland, G. J., Chatzikos, M., Guzmán, F., et al. 2017, Rev. Mex. Astron. Astrofis., 53, 385

Ferreras, I., Pasquali, A., Malhotra, S., et al. 2009, ApJ, 706, 158

Ferreras, I., Trujillo, I., Mármol-Queraltó, E., et al. 2014, MNRAS, 444, 906

Finkelstein, S. L., Cohen, S. H., Moustakas, J., et al. 2011, ApJ, 733, 117

Finkelstein, S. L., Papovich, C., Dickinson, M., et al. 2013, Nature, 502, 524

Finkelstein, S. L., Ryan, Russell E., J., Papovich, C., et al. 2015, ApJ, 810, 71

Finoguenov, A., Tanaka, M., Cooper, M., et al. 2015, A&A, 576, A130

Fioc, M., & Rocca-Volmerange, B. 1997, A&A, 500, 507

Gardner, J. P., Mather, J. C., Clampin, M., et al. 2006, SSRv, 123, 485

Geach, J. E., Smail, I., Best, P. N., et al. 2008, MNRAS, 388, 1473

Giavalisco, M., Ferguson, H. C., Koekemoer, A. M., et al. 2004, ApJ, 600, L93

Gobat, R., Daddi, E., Onodera, M., et al. 2011, A&A, 526, A133

Grazian, A., Fontana, A., de Santis, C., et al. 2006, A&A, 449, 951

Grogin, N. A., Kocevski, D. D., Faber, S. M., et al. 2011, ApJS, 197, 35

Grützbauch, R., Conselice, C. J., Bauer, A. E., et al. 2011, MNRAS, 418, 938

Hathi, N. P., Ferreras, I., Pasquali, A., et al. 2009, ApJ, 690, 1866

Hathi, N. P., Malhotra, S., & Rhoads, J. E. 2008, ApJ, 673, 686

Herenz, E. C., Urrutia, T., Wisotzki, L., et al. 2017, A&A, 606, A12

Hildebrandt, H., Erben, T., Dietrich, J. P., et al. 2006, A&A, 452, 1121

Horne, K. 1986, PASP, 98, 609

Hunt, L., Dayal, P., Magrini, L., & Ferrara, A. 2016, MNRAS, 463, 2020

Ilbert, O., Arnouts, S., McCracken, H. J., et al. 2006, A&A, 457, 841

Inami, H., Bacon, R., Brinchmann, J., et al. 2017, A&A, 608, A2

Izotov, Y. I., Stasińska, G., Meynet, G., Guseva, N. G., & Thuan, T. X. 2006, A&A, 448, 955

Jansen, R. A., Alpaslan, M., Ashby, M., et al. 2017, in American Astronomical Society Meeting Abstracts, Vol. 229, American Astronomical Society Meeting Abstracts #229, 438.04

Jiang, T., Malhotra, S., Rhoads, J. E., & Yang, H. 2019, ApJ, 872, 145

Jones, E., Oliphant, T., Peterson, P., et al. 2001–, SciPy: Open source scientific tools for Python, [Online; accessed <today>]

Jones, T., Martin, C., & Cooper, M. C. 2015, ApJ, 813, 126

Kajisawa, M., Ichikawa, T., Tanaka, I., et al. 2011, PASJ, 63, 379

Kauffmann, G., White, S. D. M., Heckman, T. M., et al. 2004, MNRAS, 353, 713

Kennicutt, Robert C., J. 1998, ARA&A, 36, 189

Kennicutt, Robert C., J., Keel, W. C., van der Hulst, J. M., Hummel, E., & Roettiger, K. A. 1987, AJ, 93, 1011

Kewley, L. J., & Dopita, M. A. 2002, ApJS, 142, 35

Kewley, L. J., Dopita, M. A., Leitherer, C., et al. 2013, ApJ, 774, 100

Kewley, L. J., & Ellison, S. L. 2008, ApJ, 681, 1183

Kewley, L. J., Groves, B., Kauffmann, G., & Heckman, T. 2006, MNRAS, 372, 961

Kobulnicky, H. A., & Kewley, L. J. 2004, ApJ, 617, 240

Kobulnicky, H. A., & Zaritsky, D. 1999, ApJ, 511, 118

Kocevski, D. D., Faber, S. M., Mozena, M., et al. 2012, ApJ, 744, 148

Kochiashvili, I., Møller, P., Milvang-Jensen, B., et al. 2015, A&A, 580, A42

Koekemoer, A. M., Faber, S. M., Ferguson, H. C., et al. 2011, ApJS, 197, 36

Kriek, M., van Dokkum, P. G., Labbé, I., et al. 2009, ApJ, 700, 221

Kriek, M., Shapley, A. E., Reddy, N. A., et al. 2015, ApJS, 218, 15

Kümmel, M., Walsh, J. R., Pirzkal, N., Kuntschner, H., & Pasquali, A. 2009, PASP, 121, 59

Kuntschner, H., Kümmel, M., Walsh, J. R., & Bushouse, H. 2011, Revised Flux Calibration of the WFC3 G102 and G141 grisms, Tech. rep.

Kurk, J., Cimatti, A., Zamorani, G., et al. 2009, A&A, 504, 331

Kurk, J., Cimatti, A., Daddi, E., et al. 2013, A&A, 549, A63

Lara-López, M. A., Cepa, J., Bongiovanni, A., et al. 2010, A&A, 521, L53

Larson, R. L., Finkelstein, S. L., Pirzkal, N., et al. 2018, ApJ, 858, 94

Le Fèvre, O., Cassata, P., Cucciati, O., et al. 2013, A&A, 559, A14

Le Fèvre, O., Tasca, L. A. M., Cassata, P., et al. 2015, A&A, 576, A79

Lee, J. C., Gil de Paz, A., Tremonti, C., et al. 2009, ApJ, 706, 599

Lilly, S. J., Carollo, C. M., & Stockton, A. N. 2003, ApJ, 597, 730

Liu, C. T., & Green, R. F. 1998, AJ, 116, 1074

Luo, B., Brandt, W. N., Xue, Y. Q., et al. 2017, VizieR Online Data Catalog, J/ApJS/228/2

Ly, C., Malkan, M. A., Nagao, T., et al. 2014, ApJ, 780, 122

Madau, P., & Dickinson, M. 2014, ARA&A, 52, 415

Maier, C., Lilly, S. J., Carollo, C. M., Stockton, A., & Brodwin, M. 2005, ApJ, 634, 849

Maiolino, R., Nagao, T., Grazian, A., et al. 2008, A&A, 488, 463

Malhotra, S., Rhoads, J. E., Pirzkal, N., et al. 2005, ApJ, 626, 666

Mannucci, F., Cresci, G., Maiolino, R., Marconi, A., & Gnerucci, A. 2010, MNRAS, 408, 2115

Mannucci, F., Cresci, G., Maiolino, R., et al. 2009, MNRAS, 398, 1915

McCarthy, P. J., Yan, L., Freudling, W., et al. 1999, ApJ, 520, 548

McLure, R. J., Pentericci, L., Cimatti, A., et al. 2018, MNRAS, 479, 25

Mei, S., Scarlata, C., Pentericci, L., et al. 2015, ApJ, 804, 117

Meurer, G. R., Heckman, T. M., & Calzetti, D. 1999, ApJ, 521, 64

Meurer, G. R., Wong, O. I., Kim, J. H., et al. 2009, ApJ, 695, 765

Momcheva, I. G., Brammer, G. B., van Dokkum, P. G., et al. 2016, ApJS, 225, 27

Morris, A. M., Kocevski, D. D., Trump, J. R., et al. 2015, AJ, 149, 178

Morrissey, P., Conrow, T., Barlow, T. A., et al. 2007, ApJS, 173, 682

Muzzin, A., Wilson, G., Yee, H. K. C., et al. 2012, ApJ, 746, 188

Muzzin, A., van der Burg, R. F. J., McGee, S. L., et al. 2014, ApJ, 796, 65

Newville, M., Stensitzki, T., Allen, D. B., & Ingargiola, A. 2014, LMFIT: Non-Linear Least-Square Minimization and Curve-Fitting for Python, doi:10.5281/zenodo.11813

Noeske, K. G., Faber, S. M., Weiner, B. J., et al. 2007, ApJ, 660, L47

Nonino, M., Dickinson, M., Rosati, P., et al. 2009, ApJS, 183, 244

Oke, J. B., & Gunn, J. E. 1983, ApJ, 266, 713

Ono, Y., Ouchi, M., Mobasher, B., et al. 2012, ApJ, 744, 83

Pagel, B. E. J., Edmunds, M. G., Blackwell, D. E., Chun, M. S., & Smith, G. 1979, MNRAS, 189, 95

Palmer, H. K. 1903, Lick Observatory Bulletin, 2, 46

Papovich, C., Momcheva, I., Willmer, C. N. A., et al. 2010, ApJ, 716, 1503

Pasquali, A., Pirzkal, N., Walsh, J. R., et al. 2003, in Astronomy, Cosmology and Fundamental Physics, ed. P. A. Shaver, L. Dilella, & A. Giménez, 471

Pasquali, A., van den Bosch, F. C., Mo, H. J., Yang, X., & Somerville, R. 2009, MNRAS, 394, 38

Pasquali, A., Ferreras, I., Panagia, N., et al. 2006, ApJ, 636, 115

Patel, S. G., Holden, B. P., Kelson, D. D., Illingworth, G. D., & Franx, M. 2009, ApJ, 705, L67

Pettini, M., & Pagel, B. E. J. 2004, MNRAS, 348, L59

Pharo, J., Malhotra, S., Rhoads, J., et al. 2018, ApJ, 856, 116

—. 2019, ApJ, 874, 125

Pilyugin, L. S., & Thuan, T. X. 2005, ApJ, 631, 231

Pirzkal, N., Xu, C., Malhotra, S., et al. 2004, ApJS, 154, 501

Pirzkal, N., Burgasser, A. J., Malhotra, S., et al. 2009, ApJ, 695, 1591

Pirzkal, N., Rothberg, B., Ly, C., et al. 2013, ApJ, 772, 48

Pirzkal, N., Malhotra, S., Ryan, R. E., et al. 2017, ApJ, 846, 84

Pirzkal, N., Rothberg, B., Ryan, R. E., et al. 2018, ApJ, 868, 61

Planck Collaboration, Ade, P. A. R., Aghanim, N., et al. 2014, A&A, 571, A16

Rafelski, M., Teplitz, H. I., Gardner, J. P., et al. 2015, AJ, 150, 31

Ravikumar, C. D., Puech, M., Flores, H., et al. 2007, A&A, 465, 1099

Reddy, N. A., Steidel, C. C., Erb, D. K., Shapley, A. E., & Pettini, M. 2006, ApJ, 653, 1004

Retzlaff, J., Rosati, P., Dickinson, M., et al. 2010, A&A, 511, A50

Rhoads, J. E., Malhotra, S., Dey, A., et al. 2001, in Astronomical Society of the Pacific Conference Series, Vol. 232, The New Era of Wide Field Astronomy, ed. R. Clowes, A. Adamson, & G. Bromage, 196

Rhoads, J. E., Panagia, N., Windhorst, R. A., et al. 2005, ApJ, 621, 582

Rhoads, J. E., Malhotra, S., Pirzkal, N., et al. 2009, ApJ, 697, 942

Rhoads, J. E., Malhotra, S., Stern, D., et al. 2013, ApJ, 773, 32

Ryan, R. E., J., Hathi, N. P., Cohen, S. H., et al. 2007, ApJ, 668, 839

Ryan, R. 2013, Understanding the Population of Distant Ultracool-Dwarfs from WISPS and 3d-HST, HST Proposal

Sanders, R. L., Shapley, A. E., Zhang, K., & Yan, R. 2017, ApJ, 850, 136

Sanders, R. L., Shapley, A. E., Kriek, M., et al. 2015, ApJ, 799, 138

—. 2016, ApJ, 825, L23

Santini, P., Ferguson, H. C., Fontana, A., et al. 2015, ApJ, 801, 97

Savaglio, S., Glazebrook, K., Le Borgne, D., et al. 2005, ApJ, 635, 260

Sawicki, M. J., Lin, H., & Yee, H. K. C. 1997, AJ, 113, 1

Scoville, N., Arnouts, S., Aussel, H., et al. 2013, ApJS, 206, 3

Silverman, J. D., Mainieri, V., Salvato, M., et al. 2010, ApJS, 191, 124

Skelton, R. E., Whitaker, K. E., Momcheva, I. G., et al. 2014, ApJS, 214, 24

Smith, M. G. 1978, Vistas in Astronomy, 22, 321

Sobral, D., Best, P. N., Matsuda, Y., et al. 2012, MNRAS, 420, 1926

Sobral, D., Best, P. N., Smail, I., et al. 2011, MNRAS, 411, 675

Song, M., Finkelstein, S. L., Gebhardt, K., et al. 2014, ApJ, 791, 3

Spergel, D., Gehrels, N., Baltay, C., et al. 2015, arXiv e-prints, arXiv:1503.03757

Spitler, L. R., Labbé, I., Glazebrook, K., et al. 2012, ApJ, 748, L21

Stanway, E. R., & Eldridge, J. J. 2018, MNRAS, 479, 75

Steidel, C. C., Adelberger, K. L., Shapley, A. E., et al. 2003, ApJ, 592, 728

Steidel, C. C., Giavalisco, M., Dickinson, M., & Adelberger, K. L. 1996, AJ, 112, 352

Steidel, C. C., Rudie, G. C., Strom, A. L., et al. 2014, ApJ, 795, 165

Storey, P. J., & Zeippen, C. J. 2000, MNRAS, 312, 813

Straughn, A. N., Meurer, G. R., Pirzkal, N., et al. 2008, AJ, 135, 1624

Straughn, A. N., Pirzkal, N., Meurer, G. R., et al. 2009, AJ, 138, 1022

Tilvi, V., Pirzkal, N., Malhotra, S., et al. 2016, ApJ, 827, L14

Tran, K.-V. H., Papovich, C., Saintonge, A., et al. 2010, ApJ, 719, L126

Tremonti, C. A., Heckman, T. M., Kauffmann, G., et al. 2004, ApJ, 613, 898

Treu, T., Schmidt, K. B., Brammer, G. B., et al. 2015, ApJ, 812, 114

Trump, J. R., Konidaris, N. P., Barro, G., et al. 2013, ApJ, 763, L6

Trump, J. R., Sun, M., Zeimann, G. R., et al. 2015, ApJ, 811, 26

Vanzella, E., Cristiani, S., Dickinson, M., et al. 2008, A&A, 478, 83

Vanzella, E., Giavalisco, M., Dickinson, M., et al. 2009, ApJ, 695, 1163

Wasilewski, A. J. 1983, ApJ, 272, 68

Weisz, D. R., Johnson, B. D., Johnson, L. C., et al. 2012, ApJ, 744, 44

Wirth, G. D., Willmer, C. N. A., Amico, P., et al. 2004, AJ, 127, 3121

Wirth, G. D., Trump, J. R., Barro, G., et al. 2015, AJ, 150, 153

Worthey, G. 1994, ApJS, 95, 107

Wuyts, S., Labbé, I., Förster Schreiber, N. M., et al. 2008, ApJ, 682, 985

Wuyts, S., van Dokkum, P. G., Franx, M., et al. 2009, ApJ, 706, 885

Xia, L., Malhotra, S., Rhoads, J., et al. 2011, AJ, 141, 64

—. 2012, AJ, 144, 28

Xu, C., Pirzkal, N., Malhotra, S., et al. 2007, AJ, 134, 169

Xue, Y. Q., Luo, B., Brandt, W. N., et al. 2011, ApJS, 195, 10

Yang, H., Malhotra, S., Rhoads, J. E., & Wang, J. 2017, ApJ, 847, 38

Yoshikawa, T., Akiyama, M., Kajisawa, M., et al. 2010, ApJ, 718, 112

Zahid, H. J., Dima, G. I., Kewley, L. J., Erb, D. K., & Davé, R. 2012, ApJ, 757, 54

Zahid, H. J., Geller, M. J., Kewley, L. J., et al. 2013, ApJ, 771, L19

Zahid, H. J., Kewley, L. J., & Bresolin, F. 2011, ApJ, 730, 137

APPENDIX A

GS1/HUDF EMISSION LINES

ID	RA	Dec	Hα	[OIII]	Hβ	[OIII]4363	[OII]3727	z[c]
724	53.17226	-27.76062	-	-	-	-	533 ± 53	1.550
950	53.16150	-27.76762	789 ± 79	254 ± 31[b]	101 ± 14[b]	17 ± 9[b]	260 ± 30[b]	0.678
970	53.16018	-27.76931	-	621 ± 36	139 ± 17	-	216 ± 52[b]	1.037
1013	53.16993	-27.77103	772 ± 77	368 ± 42[b]	674 ± 96[b]	-	1362 ± 109[b]	0.622
1016	53.17210	-27.77038	215 ± 26	50 ± 12[b]	34 ± 23[b]	17 ± 9[b]	89 ± 13[b]	0.622
1056	53.16245	-27.77091	-	261 ± 13	33 ± 3	-	43 ± 10[b]	1.038
1103	53.17400	-27.77206	2019 ± 285[a]	80 ± 18[b]	178 ± 20[b]	71 ± 18[b]	303 ± 30[b]	0.334
1132	53.18448	-27.77225	-	198 ± 43[a]	60 ± 36[a]	-	48 ± 24[b]	0.840
1171	53.15122	-27.77284	867 ± 87	757 ± 44[b]	158 ± 22[b]	21 ± 11[b]	332 ± 30[b]	0.606
1239	53.19146	-27.77389	667 ± 70	-	-	-	-	0.420
1295	53.16236	-27.77506	1869 ± 522[a]	198 ± 21[b]	476 ± 49[b]	109 ± 46[b]	655 ± 55[b]	0.420
1296	53.15936	-27.77503	-	354 ± 32	132 ± 13	-	-	1.219
1299	53.16080	-27.77537	657 ± 66	126 ± 76[b]	-	18 ± 9[b]	671 ± 48[b]	0.622
1316	53.16531	-27.77486	-	92 ± 8	77 ± 8	-	79 ± 32[b]	1.253
1359	53.18591	-27.77561	-	-	-	-	240 ± 77[a]	1.414
1392	53.18105	-27.77618	1335 ± 71	151 ± 52[b]	72 ± 9[b]	31 ± 10[b]	211 ± 29[b]	0.668
1467	53.15105	-27.77731	355 ± 21	337 ± 51[a]	69 ± 39[b]	-	194 ± 26[b]	0.736
1476	53.14744	-27.77760	-	-	-	-	190 ± 11	1.859
1477	53.15829	-27.77745	-	-	-	-	311 ± 20	1.556
1481	53.14661	-27.77749	-	281 ± 22	57 ± 6	-	107 ± 28[b]	1.088
1500	53.15234	-27.77795	-	-	-	-	214 ± 74[a]	1.413

Fluxes are given in units of 10^{-19} ergs s^{-1} cm^{-2}

[a] Line measured in FIGS and MUSE.

[b] Line measured only in MUSE.

[c] Derived from central wavelength of the most significantly detected line, averaged from PAs and MUSE.

ID	RA	Dec	Hα	[OIII]	Hβ	[OIII]4363	[OII]3727	z[c]
1552	53.15720	-27.77852	-	-	78 ± 13	-	299 ± 44[a]	1.307
1689	53.16248	-27.78035	559 ± 49	708 ± 83[a]	103 ± 32[b]	31 ± 14[b]	4 ± 11[b]	0.719
1711	53.19700	-27.78060	-	575 ± 46	-	-	-	0.733
1728	53.17633	-27.78086	685 ± 45	660 ± 44[a]	90 ± 11[b]	-	109 ± 16[b]	0.535
1803	53.17007	-27.78207	-	-	56 ± 8	-	135 ± 27[a]	1.351
1829	53.15076	-27.78256	-	-	90 ± 9	-	137 ± 38[a]	1.352
1851	53.15278	-27.78270	-	926 ± 101[a]	125 ± 21[b]	-	260 ± 24[b]	0.764
1900	53.18457	-27.78332	-	979 ± 70	101 ± 10	-	196 ± 28[b]	1.136
1901	53.18433	-27.78337	-	255 ± 19	14 ± 1	-	-	1.257
1946	53.19259	-27.78379	-	429 ± 36	42 ± 8	-	-	0.869
2023	53.15186	-27.78475	-	285 ± 26	36 ± 4	-	36 ± 18[b]	1.219
2039	53.16657	-27.78486	-	-	30 ± 5	-	103 ± 27[a]	1.320
2049	53.16935	-27.78499	-	-	27 ± 3	-	100 ± 27[a]	1.344
2138	53.16048	-27.78630	-	356 ± 29	67 ± 7	-	-	0.984
2168	53.16347	-27.78664	285 ± 20	228 ± 19[b]	42 ± 4[b]	14 ± 4[b]	64 ± 6[b]	0.468
2187	53.17775	-27.78697	-	336 ± 22	100 ± 11	-	143 ± 23[b]	0.955
2221	53.16410	-27.78730	-	2168 ± 156	318 ± 32	-	284 ± 50[b]	1.097
2291	53.14930	-27.78853	-	-	-	-	453 ± 45	1.917
2338	53.15736	-27.78922	-	346 ± 12	4 ± 0.4	-	19 ± 2[b]	1.015

Fluxes are given in units of 10^{-19} ergs s^{-1} cm^{-2}

[a] Line measured in FIGS and MUSE.

[b] Line measured only in MUSE.

[c] Derived from central wavelength of the most significantly detected line, averaged from PAs and MUSE.

ID	RA	Dec	Hα	[OIII]	Hβ	[OIII]4363	[OII]3727	z[c]
2363	53.16802	-27.78967	718 ± 61	373 ± 31[b]	31 ± 21[b]	-	627 ± 48[b]	0.619
2378	53.18795	-27.79000	8916 ± 568	198 ± 36[b]	490 ± 44[b]	82 ± 18[b]	640 ± 57[b]	0.436
2385	53.18481	-27.78993	-	392 ± 31	160 ± 25	-	432 ± 63[b]	0.954
2417	53.16042	-27.79037	-	-	-	-	355 ± 36	1.614
2495	53.18413	-27.79153	-	251 ± 15	51 ± 5.1	-	-	1.224
2517	53.16161	-27.79230	16439 ± 1374	3238 ± 198[b]	1127 ± 88[b]	45 ± 17[b]	3279 ± 202[b]	0.459
2560	53.18416	-27.79264	5114 ± 225	1810 ± 226[a]	716 ± 54[b]	147 ± 54[b]	1495 ± 101[b]	0.738
2570	53.16412	-27.79265	-	-	31 ± 3	-	90 ± 26[a]	1.311
2654	53.18221	-27.79399	279 ± 28	997 ± 54[a]	33 ± 29[b]	-	81 ± 16[b]	0.734
2669	53.15663	-27.79430	-	329 ± 32	119 ± 12	-	-	1.094
2696	53.15586	-27.79490	-	785 ± 43	216 ± 18	-	-	1.104
2720	53.15675	-27.79558	-	732 ± 36	330 ± 33	-	399 ± 76[b]	1.099
2732	53.16133	-27.79580	-	-	-	-	486 ± 135[a]	1.498
2783	53.18808	-27.79574	126 ± 13	43 ± 17[b]	-	9 ± 7[b]	15 ± 10[b]	0.532
2872	53.16687	-27.79771	-	616 ± 43	66 ± 7	-	410 ± 28[b]	0.984
2942	53.16112	-27.79880	-	388 ± 34	20 ± 2	-	231 ± 91[b]	1.238
4198	53.17838	-27.76824	1965 ± 115	318 ± 277[b]	474 ± 185[b]	111 ± 17[b]	1074 ± 97[b]	0.669
4258	53.15229	-27.77009	-	-	-	-	421 ± 33	1.859
4284	53.18454	-27.76822	-	-	-	-	74 ± 7	1.839
6865	53.19033	-27.77430	-	196 ± 12	120 ± 12.0	-	-	0.902
8178	53.18766	-27.78378	84 ± 8	127 ± 37[a]	92 ± 45[b]	-	17 ± 15[b]	0.739

Fluxes are given in units of 10^{-19} ergs s^{-1} cm^{-2}

[a] Line measured in FIGS and MUSE.

[b] Line measured only in MUSE.

[c] Derived from central wavelength of the most significantly detected line, averaged from PAs and MUSE.

APPENDIX B

FULL EMISSION LINE CATALOG

Below is the complete catalog of emission line galaxies identified in Chapter 4. The columns are the each object's FIGS field; the ELG's FIGS ID number; its Right Ascention (RA) and Declination (Dec) in degrees; the ELG's F105W AB magnitude; the identified emission line, one of Hα λ6463, [OIII]$\lambda\lambda$4959,5007, and [OII]$\lambda\lambda$3727,3729; the measured line flux and error in 10^{-18} erg s^{-1} cm^{-2}; the redshift z_{grism} derived from the line center; and the resframe equivalent width (EW) in Å.

Field	ID	RA	Dec	F105W	Line	Flux	z_{grism}	EW
GN1	1134	189.167313	62.306263	24.4	Hα	20 ± 4	0.635	48
GN1	1144	189.139786	62.305721	22.6	Hα	60 ± 9	0.557	34
GN1	1225	189.201447	62.304108	22.4	Hα	100 ± 25	0.636	49
GN1	1289	189.172318	62.302406	23.2	Hα	61 ± 6	0.529	44
GN1	1297	189.156693	62.302139	24.2	Hα	51 ± 10	0.384	70
GN1	1339	189.193359	62.30109	22.9	Hα	88 ± 8	0.672	52
GN1	1344	189.182663	62.301079	23.8	[OIII] λ5007	52 ± 11	1.014	69
GN1	1354	189.178833	62.300762	24.7	[OIII] λ5007	23 ± 11	1.09	52
GN1	1413	189.134064	62.299328	22.7	[OIII] λ5007	121 ± 13	1.013	55
GN1	1458	189.199326	62.29826	23.5	Hα	35 ± 8	0.647	50
GN1	1485	189.143372	62.297356	21.6	Hα	108 ± 12	0.684	32
GN1	1494	189.149567	62.297413	24.2	Hα	28 ± 5	0.679	44
GN1	1497	189.15683	62.296238	20.6	Hα	393 ± 32	0.554	44
GN1	1499	189.140961	62.297306	24.6	[OIII] λ5007	47 ± 9	0.799	62
GN1	1508	189.150726	62.297047	22.9	Hα	81 ± 8	0.711	47
GN1	1539	189.132751	62.295826	21.1	Hα	151 ± 16	0.683	33
GN1	1583	189.164795	62.295155	23.0	[OII] λ3727	109 ± 12	2.05	84
GN1	1589	189.153412	62.295105	25.4	[OIII] λ5007	40 ± 9	0.964	59
GN1	1610	189.15947	62.294628	23.2	Hα	35 ± 7	0.605	38
GN1	1640	189.186539	62.293983	23.6	Hα	51 ± 9	0.456	46
GN1	1647	189.184692	62.29356	21.1	Hα	438 ± 28	0.45	60
GN1	1681	189.161194	62.293125	26.0	[OIII] λ5007	45 ± 8	1.022	67
GN1	1715	189.149933	62.292282	24.2	Hα	30 ± 6	0.68	47
GN1	1734	189.139267	62.291878	23.5	[OIII] λ5007	15 ± 11	1.284	19
GN1	1747	189.1521	62.29171	23.7	[OIII] λ5007	51 ± 10	1.218	59
GN1	1750	189.173691	62.291481	21.8	Hα	108 ± 17	0.486	38
GN1	1756	189.151215	62.29155	24.2	[OII] λ3727	45 ± 6	1.793	68
GN1	1823	189.131577	62.289875	24.2	Hα	43 ± 7	0.537	64
GN1	1831	189.159225	62.289642	25.0	[OIII] λ5007	87 ± 10	0.801	78
GN1	1841	189.203278	62.28941	24.9	[OIII] λ5007	84 ± 9	0.955	104
GN1	1957	189.180191	62.286591	25.1	[OIII] λ5007	120 ± 11	0.795	68
GN1	1973	189.145004	62.286209	24.4	[OII] λ3727	37 ± 6	1.632	51

Field	ID	RA	Dec	F105W	Line	Flux	z_{grism}	EW
GN1	2026	189.161438	62.285141	21.3	Hα	372 ± 18	0.685	63
GN1	2033	189.182953	62.284897	21.3	Hα	193 ± 15	0.505	39
GN1	2120	189.163193	62.28294	24.7	[OII] λ3727	15 ± 6	1.693	41
GN1	2132	189.128632	62.282539	23.1	[OIII] λ5007	53 ± 11	0.94	52
GN1	2135	189.162811	62.282536	23.6	[OIII] λ5007	150 ± 11	1.014	75
GN1	2327	189.142426	62.278187	22.3	Hα	113 ± 10	0.502	49
GN1	2371	189.175491	62.277306	24.3	[OIII] λ5007	33 ± 12	0.949	60
GN1	2394	189.164597	62.276897	25.8	[OIII] λ5007	29 ± 10	1.243	125
GN1	2412	189.199005	62.276527	24.8	[OIII] λ5007	108 ± 20	0.779	76
GN1	2449	189.181458	62.275795	23.3	[OII] λ3727	37 ± 10	1.487	37
GN1	2713	189.188126	62.270935	23.5	[OII] λ3727	40 ± 10	1.444	53
GN2	488	189.378052	62.325283	24.4	[OII] λ3727	28 ± 6	2.007	68
GN2	506	189.35556	62.323696	23.4	Hα	46 ± 14	0.335	31
GN2	507	189.395798	62.323574	21.5	Hα	161 ± 10	0.635	39
GN2	514	189.370529	62.323437	24.3	[OIII] λ5007	64 ± 8	0.861	75
GN2	554	189.397171	62.32164	20.7	[OIII] λ5007	285 ± 32	0.835	32
GN2	591	189.34729	62.31987	24.9	[OII] λ3727	20 ± 5	1.996	90
GN2	598	189.369843	62.319496	24.2	[OII] λ3727	28 ± 6	1.598	57
GN2	657	189.358841	62.3158	23.6	[OII] λ3727	43 ± 6	1.596	51
GN2	659	189.405548	62.315742	23.7	[OIII] λ5007	39 ± 9	1.08	63
GN2	682	189.390213	62.319218	23.2	[OII] λ3727	63 ± 16	1.344	55
GN2	717	189.414581	62.313183	22.4	Hα	130 ± 14	0.337	46
GN2	724	189.390701	62.312847	23.3	[OII] λ3727	85 ± 8	2.005	63
GN2	740	189.349564	62.311909	23.0	Hα	39 ± 7	0.559	45
GN2	745	189.382751	62.311504	22.8	[OIII] λ5007	186 ± 19	1.084	98
GN2	746	189.402069	62.311489	24.4	[OIII] λ5007	33 ± 8	1.086	113
GN2	756	189.369843	62.310909	22.3	Hα	81 ± 20	0.519	36
GN2	757	189.421219	62.310848	22.1	Hα	78 ± 10	0.575	39
GN2	759	189.401138	62.310909	24.2	[OII] λ3727	34 ± 7	1.572	56
GN2	780	189.347214	62.310238	24.4	[OIII] λ5007	59 ± 9	1.052	68
GN2	782	189.387894	62.310043	24.5	[OIII] λ5007	34 ± 7	0.982	70
GN2	814	189.33992	62.308514	24.2	[OII] λ3727	32 ± 6	1.973	62
GN2	815	189.37941	62.308392	22.8	[OIII] λ5007	109 ± 10	1.197	67
GN2	836	189.391006	62.307247	21.9	Hα	112 ± 14	0.563	43
GN2	852	189.398239	62.306988	24.2	[OII] λ3727	20 ± 6	2.051	43
GN2	881	189.376816	62.305573	24.6	[OII] λ3727	33 ± 5	1.926	55
GN2	909	189.416992	62.304211	25.5	[OII] λ3727	21 ± 4	1.781	85
GN2	918	189.34906	62.303965	23.5	[OIII] λ5007	307 ± 205	1.078	121
GN2	938	189.419174	62.302856	22.4	[OIII] λ5007	95 ± 14	1.027	47
GN2	967	189.391983	62.301613	25.2	[OIII] λ5007	42 ± 8	1.224	71

Field	ID	RA	Dec	F105W	Line	Flux	z_{grism}	EW
GN2	969	189.367142	62.30154	25.4	[OIII] λ5007	34 ± 7	1.146	75
GN2	1049	189.385056	62.297539	24.2	[OII] λ3727	43 ± 7	2.006	82
GN2	1065	189.364334	62.29715	23.9	[OIII] λ5007	77 ± 12	1.012	64
GN2	1107	189.362579	62.295631	25.0	[OII] λ3727	15 ± 7	2.051	43
GN2	1114	189.387207	62.29525	23.3	[OIII] λ5007	97 ± 11	0.773	54
GN2	1145	189.355164	62.294254	24.1	[OIII] λ5007	32 ± 10	0.942	33
GN2	1160	189.356705	62.293705	23.4	[OII] λ3727	35 ± 8	1.526	47
GN2	1186	189.385986	62.292267	23.9	[OII] λ3727	31 ± 6	1.774	60
GN2	1227	189.376297	62.290405	24.0	[OII] λ3727	38 ± 7	1.682	75
GN2	1240	189.393906	62.289795	20.1	Hα	222 ± 24	0.638	21
GN2	1265	189.364151	62.289097	24.6	Hα	26 ± 4	0.633	47
GN2	1319	189.387177	62.287018	22.7	Hα	86 ± 8	0.632	58
GN2	3114	189.376511	62.325085	25.5	[OIII] λ5007	32 ± 12	0.839	135
GN2	3574	189.389481	62.315483	27.1	[OIII] λ5007	54 ± 10	0.863	57
GN2	4969	189.363007	62.287544	25.9	[OII] λ3727	47 ± 17	1.364	300
GS1	724	53.172264	-27.760622	22.6	[OII] λ3727	72 ± 13	1.552	42
GS1	950	53.161499	-27.76762	23.4	Hα	37 ± 8	0.679	38
GS1	970	53.160183	-27.769306	24.1	[OIII] λ5007	69 ± 11	1.044	88
GS1	1013	53.169926	-27.771027	20.0	Hα	231 ± 42	0.619	20
GS1	1016	53.172104	-27.770382	23.6	Hα	20 ± 5	0.631	40
GS1	1056	53.162453	-27.770908	24.3	[OIII] λ5007	36 ± 7	1.036	88
GS1	1103	53.174	-27.772057	20.7	Hα	199 ± 24	0.335	23
GS1	1132	53.184479	-27.772245	24.6	[OIII] λ5007	32 ± 9	0.835	50
GS1	1151	53.152878	-27.772497	24.6	[OII] λ3727	21.7 ± 5.4	1.853	55
GS1	1171	53.151215	-27.772837	23.8	Hα	50 ± 6	0.608	49
GS1	1239	53.191463	-27.77389	23.5	Hα	31 ± 7	0.419	34
GS1	1295	53.162361	-27.775063	20.6	Hα	344 ± 25	0.42	38
GS1	1296	53.159355	-27.775028	23.1	[OIII] λ5007	42 ± 17	1.22	45
GS1	1299	53.160801	-27.775373	21.2	Hα	127 ± 17	0.623	31
GS1	1359	53.185909	-27.775608	22.9	[OII] λ3727	79 ± 16	1.425	59
GS1	1392	53.181046	-27.776175	22.1	Hα	106 ± 111	0.668	41
GS1	1467	53.151047	-27.777309	24.1	[OIII] λ5007	32 ± 8	0.733	55
GS1	1467	53.151047	-27.777309	24.1	Hα	28 ± 8	0.601	47
GS1	1476	53.147438	-27.777596	23.6	[OII] λ3727	29 ± 6	1.851	46
GS1	1477	53.158291	-27.777449	24.5	[OII] λ3727	32 ± 7	1.555	56
GS1	1481	53.146614	-27.777489	25.0	[OIII] λ5007	21 ± 12	1.091	47
GS1	1500	53.152336	-27.777948	24.3	[OII] λ3727	33 ± 10	1.42	52
GS1	1552	53.157204	-27.778522	23.8	[OII] λ3727	21 ± 52	1.31	30
GS1	1689	53.162483	-27.780346	25.1	Hα	43 ± 8	0.515	64
GS1	1689	53.162483	-27.780346	25.1	[OIII] λ5007	64 ± 13	0.722	65

Field	ID	RA	Dec	F105W	Line	Flux	z_{grism}	EW
GS1	1710	53.172619	-27.78096	21.4	Hα	123 ± 13	0.62	35
GS1	1711	53.196999	-27.780598	23.9	[OIII] λ5007	36 ± 10	0.739	46
GS1	1728	53.176331	-27.780861	25.0	[OIII] λ5007	42 ± 10	1.016	60
GS1	1803	53.170067	-27.782066	26.7	[OII] λ3727	51 ± 10	1.343	75
GS1	1829	53.150764	-27.78256	24.2	[OII] λ3727	58 ± 20	1.35	60
GS1	1851	53.152782	-27.782698	24.4	[OIII] λ5007	101 ± 11	0.768	72
GS1	1864	53.175331	-27.782722	26.0	[OIII] λ5007	37 ± 20	0.843	152
GS1	1867	53.15184	-27.782864	23.2	Hα	71 ± 9	0.406	45
GS1	1900	53.184574	-27.783323	24.4	[OIII] λ5007	99 ± 16	1.137	76
GS1	1946	53.192593	-27.783791	24.7	[OIII] λ5007	66 ± 12	0.869	105
GS1	2023	53.151863	-27.784752	25.6	[OIII] λ5007	33 ± 10	1.217	86
GS1	2029	53.157948	-27.784767	28.1	[OIII] λ5007	22 ± 10	0.719	34
GS1	2029	53.157948	-27.784767	28.1	Hα	17 ± 8	0.312	26
GS1	2039	53.166565	-27.784861	27.6	[OII] λ3727	17 ± 11	1.304	104
GS1	2077	53.161686	-27.785322	27.5	Hα	30 ± 7	0.338	88
GS1	2138	53.160477	-27.786299	24.3	[OIII] λ5007	35 ± 8	0.983	57
GS1	2168	53.163471	-27.786636	25.1	Hα	17 ± 6	0.469	47
GS1	2187	53.177753	-27.786966	24.4	[OIII] λ5007	38 ± 10	0.95	75
GS1	2221	53.164097	-27.787298	23.8	[OIII] λ5007	191 ± 10	1.098	64
GS1	2291	53.149296	-27.788527	23.0	[OII] λ3727	59 ± 7	1.917	46
GS1	2338	53.15736	-27.789219	25.1	[OIII] λ5007	36 ± 13	0.999	85
GS1	2363	53.168015	-27.789671	22.8	Hα	82 ± 8	0.622	56
GS1	2375	53.176495	-27.789705	24.9	Hα	29 ± 5	0.427	48
GS1	2378	53.18795	-27.790001	20.3	Hα	739 ± 33	0.438	46
GS1	2385	53.184811	-27.789934	23.1	[OIII] λ5007	43 ± 11	0.956	45
GS1	2417	53.160419	-27.790369	23.5	[OII] λ3727	42 ± 8	1.617	44
GS1	2495	53.184132	-27.791531	23.1	[OIII] λ5007	7 ± 11	1.214	8
GS1	2517	53.161613	-27.792299	20.6	Hα	1410 ± 52	0.462	67
GS1	2560	53.184158	-27.792637	21.4	[OIII] λ5007	163 ± 18	0.739	107
GS1	2560	53.184158	-27.792637	21.4	Hα	228 ± 45	0.324	91
GS1	2570	53.164124	-27.792654	27.0	[OII] λ3727	16 ± 50	1.301	35
GS1	2654	53.182205	-27.793993	24.8	[OIII] λ5007	21 ± 12	1.28	60
GS1	2669	53.156631	-27.794302	24.3	[OIII] λ5007	42 ± 11	1.098	61
GS1	2696	53.155861	-27.794901	22.9	[OIII] λ5007	104 ± 32	1.1	74
GS1	2720	53.15675	-27.79558	21.8	[OIII] λ5007	91 ± 22	1.099	42
GS1	2732	53.161331	-27.795797	23.6	[OII] λ3727	47 ± 8	1.495	46
GS1	2783	53.188084	-27.795742	24.0	Hα	120 ± 11	0.536	49
GS1	2872	53.16687	-27.797707	23.7	[OIII] λ5007	70 ± 14	0.99	75
GS1	2942	53.161121	-27.798801	25.5	[OIII] λ5007	28 ± 14	1.228	82
GS1	4184	53.179535	-27.766174	25.1	Hα	21 ± 5	0.67	45

Field	ID	RA	Dec	F105W	Line	Flux	z_{grism}	EW
GS1	4198	53.178375	-27.76824	20.2	Hα	378 ± 32	0.674	35
GS1	4258	53.152287	-27.770088	23.7	[OII] λ3727	52 ± 9	1.853	56
GS1	4284	53.184544	-27.768221	25.2	[OII] λ3727	11 ± 6	1.839	21
GS1	6865	53.190331	-27.774298	26.8	[OIII] λ5007	18 ± 12	0.883	54
GS1	8178	53.187664	-27.783779	27.0	[OIII] λ5007	22 ± 8	0.737	110
GS2	575	53.28241	-27.843513	24.0	[OIII] λ5007	88 ± 18	0.739	73
GS2	575	53.28241	-27.843513	24.0	Hα	74 ± 13	0.509	70
GS2	577	53.273159	-27.844625	25.9	[OIII] λ5007	24 ± 10	1.231	66
GS2	596	53.274158	-27.84565	23.2	[OII] λ3727	35 ± 6	1.686	37
GS2	599	53.279076	-27.845737	23.1	[OIII] λ5007	319 ± 40	0.737	71
GS2	599	53.279076	-27.845737	23.1	Hα	239 ± 27	0.53	64
GS2	620	53.272892	-27.847765	22.2	Hα	78 ± 8	0.711	34
GS2	709	53.288483	-27.851877	24.0	Hα	22 ± 5	0.687	45
GS2	782	53.281536	-27.854385	23.7	[OIII] λ5007	81 ± 11	0.834	56
GS2	846	53.264668	-27.855431	24.6	[OII] λ3727	27 ± 7	1.757	65
GS2	868	53.275829	-27.855747	24.7	Hα	33 ± 8	0.736	80
GS2	871	53.266712	-27.856167	20.5	Hα	592 ± 39	0.528	52
GS2	887	53.291748	-27.856255	24.2	[OII] λ3727	29 ± 6	1.815	56
GS2	951	53.264828	-27.857828	24.3	[OII] λ3727	73 ± 16	1.303	76
GS2	951	53.264828	-27.857828	24.3	[OIII] λ5007	235 ± 31	1.291	107
GS2	1038	53.285847	-27.85964	20.6	[OIII] λ5007	238 ± 128	0.724	33
GS2	1038	53.285847	-27.85964	20.6	Hα	736 ± 72	0.741	64
GS2	1054	53.2869	-27.859509	22.8	[OII] λ3727	61 ± 15	1.679	38
GS2	1131	53.26556	-27.861135	23.6	[OIII] λ5007	38 ± 16	0.885	44
GS2	1215	53.266247	-27.862015	23.9	[OII] λ3727	23 ± 6	1.905	39
GS2	1240	53.293732	-27.862436	25.8	[OII] λ3727	15 ± 4	1.901	49
GS2	1270	53.275627	-27.863014	24.4	[OII] λ3727	28 ± 6	2.012	70
GS2	1280	53.283585	-27.864466	22.9	Hα	80 ± 11	0.476	47
GS2	1392	53.28775	-27.865278	24.3	Hα	21 ± 5	0.612	42
GS2	1483	53.272259	-27.867044	24.7	[OIII] λ5007	62 ± 8	0.979	73
GS2	1552	53.266247	-27.868002	22.9	[OII] λ3727	87 ± 9	1.762	54
GS2	1593	53.272778	-27.868891	21.6	Hα	147 ± 15	0.693	42
GS2	1607	53.265091	-27.86924	21.7	Hα	124 ± 17	0.524	46
GS2	1630	53.264194	-27.869268	23.3	[OII] λ3727	65 ± 10	1.817	63
GS2	1653	53.273643	-27.870647	18.4	Hα	561 ± 108	0.523	13
GS2	1666	53.268139	-27.869875	24.2	[OIII] λ5007	97 ± 12	0.737	80
GS2	1666	53.268139	-27.869875	24.2	Hα	56 ± 10	0.739	58
GS2	1772	53.28323	-27.872059	25.8	[OIII] λ5007	53 ± 10	1.176	73
GS2	1836	53.2654	-27.873278	22.8	[OII] λ3727	97 ± 10	1.988	52
GS2	3186	53.291828	-27.845343	19.9	Hα	1567 ± 72	0.524	64

Field	ID	RA	Dec	F105W	Line	Flux	z_{grism}	EW
GS2	3259	53.276016	-27.847622	24.4	[OIII] $\lambda 5007$	339 ± 24	1.262	99
GS2	3277	53.277046	-27.848417	24.6	[OII] $\lambda 3727$	23 ± 4	1.907	44
GS2	3295	53.258167	-27.849049	23.4	[OII] $\lambda 3727$	97 ± 8	1.9	66
GS2	3314	53.285191	-27.850237	24.3	[OII] $\lambda 3727$	27 ± 7	1.717	61
GS2	3347	53.266071	-27.852331	22.0	Hα	122 ± 13	0.548	50
GS2	3418	53.253826	-27.856579	27.0	[OIII] $\lambda 5007$	40 ± 12	0.909	92
GS2	3419	53.254498	-27.856409	24.3	Hα	30 ± 5	0.521	51